Thermal Science and Engineering

EnPress

2024 Volume 7 Issue 3
ISSN: 2578-1782 (Online)

https://systems.enpress-publisher.com/index.php/TSE

Editorial Board

Editor-in-Chief

Gang Zhang
A-Star, Institute of High Performance Computing (IHPC)
Singapore

Associate Editors

Nuo Yang
Huazhong University of Science and Technology
China

Yasser Mahmoudi
University of Manchester
United Kingdom

Editorial Board Members

Maziar Dehghan
Materials and Energy Research Center
Iran

Mohamed R. Eid
Northern Border University
Saudi Arabia

Hitesh Panchal
Gujarat Technological University
India

Clemente Bretti
Università di Messina
Italy

Fei Zhou
Nanjing University of Aeronautics and Astronautics
China

Xiaohu Yang
Xi'an Jiaotong University
China

Sivasankaran Sivanandam
King Abdulaziz University
Saudi Arabia

Talal Yusaf
Central Queensland University
Australia

Mousa Marzband
Northumbria University
United Kingdom

Olga E. Glukhova
Saratov State University
Russia

Zhenyu Tian
University of Chinese Academy of Sciences
China

Muneer Ismael
University of Basrah
Iraq

Ho Seon Ahn
Incheon National University
Korea

Mona Zebarjadi
University of Virginia
United States

Ioan Mihai Pop
Babeș-Bolyai University
Romania

Efstathios E. Michaelides
Texas Christian University
United States

Nehad Ali Shah
Sejong University
Korea

Jose Ordonez-Miranda
The University of Tokyo
Japan

Davood Domiri Ganji
University of Mazandaran
Iran

Mehmet Fatih Orhan
American University of Sharjah
United Arab Emirates

Olivier Mathieu
Texas A&M University
United States

Weiwei Yang
Xi'an Jiaotong University
China

Yuanzheng Li
Huazhong University of Science and Technology
China

Jingchun Feng
Guangdong University of Technology
China

Zhengmao Li
Nanyang Technological University
Singapore

Chin-Hsiang Cheng
National Cheng Kung University
Taiwan

Erkan Oterkus
University of Strathclyde Glasgow
United Kingdom

Leilei Dai
University of Minnesota
United States

Shail Upadhyay
Banaras Hindu University
India

Xianglei Liu
Nanjing University of Aeronautics and Astronautics
China

Grigorios Kyriakopoulos
National Technical University of Athens
Greece

Mohammed El Ganaoui
Université Henri Poincaré
France

Anqing Zheng
Chinese Academy of Sciences
China

Muhammad Hilmy Alfaruqi
Chonnam National University
Korea

Yuanyuan Duan
Tsinghua University
China

Silvio Simani
University of Ferrara
Italy

Abolfazl Ahmadi
Iran University of Science and Technology
Iran

Yuekuan Zhou
The Hong Kong University of Science and Technology
Hong Kong

Harry D. Kambezidis
National Observatory of Athens
Greece

Alban Kuriqi
University of Lisbon
Portugal

Mario Luigi Ferrari
Università degli Studi di Genova
Italy

Jingzheng Ren
The Hong Kong Polytechnic University
Hong Kong

Linchuan Zhao
Shanghai Jiao Tong University
China

Devraj Singh
Amity School of Engineering & Technology
India

Mohsen Sheikholeslami
Babol Noshiravni University of Technology
Iran

Nima E. Gorji
Dublin City University
Ireland

Esmail Lakzian
Shahid Beheshti University
Iran

Qingsong Wang
University of Science and Technology of China
China

Khaled Chetehouna
Institut National des Sciences Appliquées (INSA) Centre Val de Loire
France

Hamdy Mahmoud Youssef
Umm Al-Qura University
Saudi Arabia

Emad Mohamed El-Said
Fayoum University
Egypt

Volume 7 Issue 3 • 2024

Thermal Science and Engineering

Editors-in-Chief

Prof. Gang Zhang

A-Star, Institute of High Performance Computing (IHPC)

Singapore

EnPress Publisher

2024 | Volume 7 | Issue 3

Thermal Science and Engineering

https://systems.enpress-publisher.com/index.php/TSE

Contents

Articles

Thermal Science and Engineering 2024, 7(3), 8615.
https://doi.org/10.24294/tse.v7i3.8615

Article

Analysis of magnetized bio-convective Ellis nanofluid flow: Impact of viscous dissipation and activation energy

Tayyaba Akhtar[1,*], Muhammad Abid[2], Mohamed M. Awad[3], Munaza Chaudhry[1], Muhammad Imran[1]

[1] Department of Mathematics, Government College University Faisalabad, Faisalabad 38000, Pakistan
[2] Department of Mathematics, North Caroline State University, 27695 NC Raleigh, USA
[3] Mechanical Power Engineering Department, Faculty of Engineering, Mansoura University, Mansoura, Egypt
*** Corresponding author:** Tayyaba Akhtar, tayyabakanwal10@gmail.com

CITATION

Akhtar T, Abid M, Awad MM, et al. Analysis of magnetized bio-convective Ellis nanofluid flow: impact of viscous dissipation and activation energy. Thermal Science and Engineering. 2024; 7(3): 8615. https://doi.org/10.24294/tse.v7i3.8615

ARTICLE INFO

Received: 5 May 2024
Accepted: 26 June 2024
Available online: 8 July 2024

COPYRIGHT

Copyright © 2024 by author(s). *Thermal Science and Engineering* is published by EnPress Publisher, LLC. This work is licensed under the Creative Commons Attribution (CC BY) license. https://creativecommons.org/licenses/by/4.0/

Abstract: This study delves into the complex flow dynamics of magnetized bioconvective Ellis nanofluids, highlighting the critical roles of viscous dissipation and activation energy. By employing a MATLAB solver to tackle the boundary value problem, the research offers a thorough exploration of how these factors, along with oxytactic microorganism's mobility, shape fluid behavior in magnetized systems. Our findings demonstrate that an increase in the magnetization factor (M) leads to a decrease in both velocity and temperature due to enhanced interparticle resistance from the Lorentz force. Additionally, streamline analysis reveals that higher mixed convection parameters ($\aleph$) intensify flow concentration near surfaces, while increased slip parameters reduce shear stress and boundary layer thickness. Although isotherm analysis shows that higher Ellis fluid parameters enhance heat conduction, with greater porosity values promoting efficient thermal dissipation. These insights significantly advance our understanding of nanofluid dynamics, with promising implications for bioengineering and materials science, setting the stage for future research in this field.

Keywords: Ellis nanofluid; activation energy; darcy-forchheimer; magnetic field; numerical scheme

1. Introduction

Nanotechnology is an area of applied sciences and technology that includes atomic and molecular-scale manipulation of matter, usually below 100 nanometers. So, unlike their macroscale equivalents, these materials have special features because of the elevated surface-to-volume ratio and other novel physiochemical properties such as solubility, strength, diffusivity, magnetic, thermodynamic, etc. At present, various industries use fluids to increase production by increasing/reducing the flow of energy to the system. In this regard, nanofluids are of great significance. Nanofluids consist of sparse liquid suspensions of nanoparticles. Previous research suggests that nanofluids exhibit superior thermophysical properties. Contrasted with base fluids such as oil or water, nanofluids exhibit enhanced properties entailing thermal characteristics, thermal diffusivity, viscosity, and convective heat transfer coefficients. Typically, nanoliquids utilize nanomaterials derived from metals (such as Ag, Al, Cu, Fe, Au), non-metals (including carbon nanotubes and graphite), metallic oxides (like Al_2O_3, CuO, TiO_2, SiO_2, FeO), carbides/nitrides (such as TiC, SiC, TiN, SiN, AlNC, AlN), and layered materials (e.g., Al + Al_2O_3, Cu + C), with conventional liquids like water, glycol, and engine oil commonly employed as base fluids in the nanofluid formation process.

The development of nanotechnology has significantly enhanced modern living.

Owing to the beneficial use of nanoparticles, we have seen their valuable applications span across the disciplines of engineering, chemistry, mechanics, and biology. Nanoparticles are employed to enhance cooling in diverse heat exchange processes, including metal strip cooling, chemical transformations, automobile engines, welding machinery, microwave tubes, nuclear reactions, computing devices, and assorted engineering equipment, owing to their enhanced thermal characteristics [1]. In another article, Turkyilmazoglu [2] explored the thermal behavior of nanofluid flow in a wall jet employing five distinct nanoparticle varieties. He aimed to figure out how different nanofluids affect the heat and flow behavior of the wall jet. Arafa et al. [3] conducted a study on entropy generation in nanofluid flow with changing porosity along complex vertical duct. It has been noted that using nanoparticles results in very good improvement. It has been noted that the application of nanoparticles results in remarkable improvement. A comparable estimated resolution for fully established nanofluid flow is derived in Hussain et al.'s paper [4]. For the examination of heat and mass transfer phenomena, a vertical conduit with composite permeable medium has been used. A few significant studies on nanofluids are mentioned in Abbas et al. [5], Nadeem et al. [6], and Amjad et al.'s [7] works. In the comprehensive work, the authors delve into advanced mathematical approaches for understanding the behavior of nanofluids and complex fluid systems [8]. This resource offers critical insights into various fluid dynamic models, emphasizing their practical applications in both theoretical and engineering contexts.

Since the classical Newtonian liquid hypothesis is unable to fully estimate the significance of fluid characteristics involving suspended molecules, non-Newtonian flow, and heat transfer processes, it has garnered considerable attention. Not only are non-Newtonian fluid flows valuable from a technological standpoint, but their governing equations also display interesting mathematical properties. The physicochemical properties of Newtonian fluids are incredibly complex, and there isn't a single constitutive relation that can be universally applied to all non-Newtonian fluids. In the articles by Yahya et al. [9], Ahmad et al. [10], Gul et al. [11], and Abdal et al. [12], a number of noteworthy studies on these flows have been presented. All of the aforementioned studies investigate the dynamics of flow, heat, and mass transfer of assorted non-Newtonian fluids through a comprehensive literature review. Nevertheless, there has been no endeavor to characterize the flow dynamics of magnetized bioconvective Ellis nanofluids while considering the ramifications of viscous dissipation and activation energy. The Bingham (viscoelastic) and Power law models are generalized by the Ellis model. At elevated shear stresses, it demonstrates power-law behavior, transitioning to Newtonian characteristics at lower shear forces. The constitutive equation of the Ellis model serves as a foundational framework for deducing the constitutive equation of the Bingham model. The Ellis fluid model approach is flexible in adjusting viscosity rheological data across various non-Newtonian fluids and geometries. Hence, the Ellis fluid pattern can be regarded as a fusion of the Bingham, power-law, and Newtonian fluid models. It offers a helpful infrastructure for assessing the rheology of various biofluids, including blood, chyme, pulmonary mucus, cervical mucus, etc. Furthermore, several notable studies have explored the application of the Ellis fluid model in plentiful designs for flow analysis [13–16].

Analyzing heat and mass transfer spectacles in fluid flow deformable cylinders has attracted significant attention in light of its relevance in engineering and industry. Shaheen et al. [17] explored the interaction between Soret and Dufour phenomena in the flow of Casson nanofluid around a deformable cylinder, considering dynamic properties and integrating Arrhenius activation energy. Hayat et al. [18] interrogated magnetohydrodynamic axisymmetric flow characteristics of a third-grade fluid adjacent to a stretching cylinder. Also, Grigoriadis et al. [19] ventured the MHD flow behavior around a cylindrical object employing the Immersed Boundary Method to comprehensively analyze the fluid dynamics. Anuar et al. [20] assessed how magnetohydrodynamics (MHD) affected the steady-state (2-D) mixed convection flow in carbon nanotubes that was caused by a nonlinear surface. When using carbon nanotubes of both single and multi-wall varieties (CNTs), kerosene and water are utilized as the base fluids. Ramesh et al. [21] presented a detailed computational analysis on radiative non-Newtonian Carreau nanofluid flow in a microchannel under magnetic properties. In an innovative study, Mebarek-Oudina et al. [22] explored the role of a quadratic linearly radiating heat source with Carreau nanofluid and exponential space-dependence past a cone and a wedge, highlighting its implications for medical engineering and renewable energy applications. Khan et al. [23] examined nonlinear radiation effects in magnetohydrodynamic flow around a cylinder containing chemically reactant species by using the shooting technique.

Understanding the swimming capability of oxytactic microorganisms is vital for elucidating various biological characteristics related to bioconvection. The dispersion of oxytactic swimming microorganisms in a constricted space is referred to as bioconvection. Bioconvection entails convective fluid motion at the nanoscale level brought on by the density gradient and the concurrent swimming of motile microorganisms. Furthermore, the use of microorganisms in fluid mechanics has increased recently in order to enhance heat transport while reducing nanoparticle agglomeration. Kuznetsov and Avramenko [24] and Geng and Kuznetsov [25] originally scrutinized bioconvection in the existence of nanoparticles. Afterwards, the concept of suspending nanoparticles with gyrotactic microorganisms was proposed by Kuznetsov [26], using Buongiorno’s principle. Bég et al. [27] conducted numerical analysis regarding the bioconvection phenomenon of nanofluid flow through porous media. In a detailed study, Mebarek-Oudina et al. [28] investigated the hybrid nanofluid magneto-convective flow and the role of porous media in contributing to entropy generation. Dharmaiah et al. [29] numerically investigated the magnetic dipole effect on a radiative ferromagnetic liquid flowing over a porous stretched sheet that provides crucial insights into the interaction between magnetic fields and fluid flow dynamics.

Flow of bioconvection through symmetrical conduit infused with nanoparticles was considered by Akbar [30], and a bio-nano-engineering model was presented. The impetus of varying magnetic field on a model of blood clotting was also investigated by Bhatti et al. [31], employing the Jeffrey fluid model in conjunction with nanoparticles and microorganisms. Dharmaiah et al. [32] explored bio-convection phenomena within a slippery two-phase Maxwell nanofluid as it moves past a vertically induced magnetic stretching regime. This analysis is particularly relevant to applications in biotechnology and engineering, where the interactions between magnetic fields and fluid dynamics play a crucial role. The magnetized laminar flow via a porous medium with non-Darcy flow characteristics of nanofluid and gyrotactic microorganisms was observed by Abbas and Palani [33]. The extrinsic magnetic effect and bioconvection flow were researched by Chakraborty et al. [34] with nanoparticles subjected to convective boundary conditions. Umar et al. [35] utilized the shooting technique to examine slip effects on a stretching sheet in fluid dynamics, considering 3-D Eyring-Powell fluid with activation energy. Incorporating the importance of gyrotactic microorganisms and thermal radiation, Khan et al. [36] discussed Oldroyd B fluid flow. This study employs a bioconvective flow of an Oldroyd-B nanofluid via stretching sheet undergoing oscillations. In the analysis of bioconvective electro-magnetohydrodynamics (EMHD) and dissipative Williamson nanofluid over a three-dimensional Riga plate, Akolade et al. [37] explored the effects of Joule heating in complex fluid flows. This study is pivotal for understanding how magnetic fields, heat dissipation, and fluid properties interact, particularly in industrial and technological applications. These phenomena are associated with several successful studies [38–41].

In a novel case study, Hiba et al. [42] conducted a thermal and streamline analysis in a grooved enclosure filled with Ag-MgO/water hybrid nanofluid using the Galerkin finite element method (FEM). The findings highlighted the potential of such nanofluids to enhance heat transfer efficiency in various engineering applications. In a significant work, Sharif and Mohammad [43] explored natural convection in cavities with constant flux heating at the bottom wall and isothermal cooling from the sidewalls. This study provided a comprehensive analysis of the thermal and flow patterns within such cavities. Based on the preceding studies, this paper aims to explore thermal and mass transfer properties within a steady, 2-dimensional MHD flow of Ellis nanofluid containing oxytactic microorganisms. The impact of thermal radiation, Darcy-Forchheimer, and magnetization via deformable cylinder are also covered in this study. The study employs the Buongiorno nanofluid model, integrating thermophoresis and Brownian motion phenomena.

Ellis nanofluid containing oxytactic microorganisms plays a crucial role in Thermal Science and Engineering by significantly enhancing heat transfer efficiency and thermal management across diverse applications. Its distinctive properties, coupled with the dynamic motion of microorganisms, facilitate improved convective heat transfer and lower thermal resistance. This advancement aligns with the journal’s mission to further knowledge in thermal science, foster sustainable energy solutions, and investigate innovative materials that optimize thermal processes in engineering systems.

2. Model analysis

The characteristics of thermo-transfer within a steady, 2-dimensional magnetohydrodynamic (MHD) flow of Ellis nanofluid containing oxytactic microorganisms have been examined. This study also encompasses the impacts of magnetization, Darcy-Forchheimer, and radiative heat transfer over a deformable cylinder as depicted in **Figure 1**, subjected to boundary conditions tailored for appropriate transport within the geometry. Consider $\bar{u}$ and $\bar{w}$ as the velocity aspects along the cylinder's horizontal $(z - axis)$ and radial $(r - axis)$ axes, respectively. The cylinder experiences stretching as described by the velocity equation $u_w(\bar{z}) = \frac{u_o \bar{z}}{L}$, where L represents the length of the cylinder and a is a constant value. A radial magnetic field B_o is imposed. The study employs the Buongiorno nanofluid model, incorporating Brownian motion and thermophoresis phenomena. Based on these considerations, the governing equations for the specified problems are as follows [44,45]:

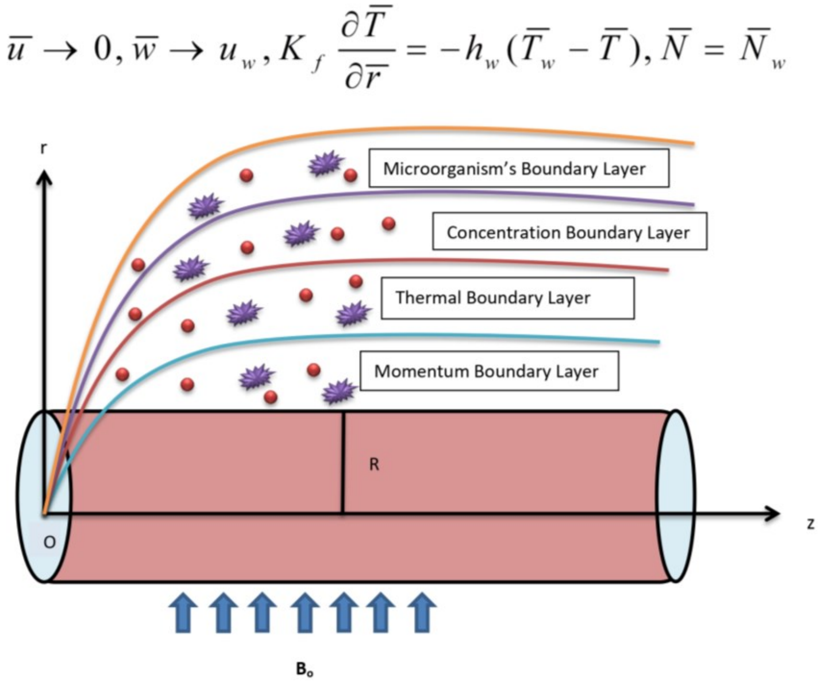

Figure 1. Visual depiction of the model's geometry.

$$\frac{\partial (r\bar{u})}{\partial \bar{z}} + \frac{\partial (r\bar{w})}{\partial \bar{r}} = 0 \tag{1}$$

$$\bar{u}\frac{\partial \bar{u}}{\partial \bar{z}} + \bar{w}\frac{\partial \bar{u}}{\partial \bar{r}} = \frac{1}{\rho_f}\frac{\partial}{\partial \bar{r}}\left(\frac{\bar{r}\mu_f}{1 + \left(\frac{1}{\sqrt{2}\tau_o^2}\frac{\partial \bar{u}}{\partial \bar{z}}\right)^{\alpha-1}}\frac{\partial \bar{u}}{\partial \bar{r}}\right) - \frac{\sigma_f B_o^2 \bar{u}}{\rho_f} - \frac{\mu_f \bar{u}}{K^* \rho_f} - \frac{\sqrt{C}_b}{k^*}\bar{u}^2 + \frac{1}{\rho_f}[(1 - C_\infty)\rho_f g \beta_t (\bar{T} - T_\infty) - (\rho_p - \rho_f) g \beta_c (\bar{C} - C_\infty) - (\rho_m - \rho_f) r^* g (\bar{N} - N_\infty)] \tag{2}$$

$$\bar{u}\frac{\partial \bar{T}}{\partial \bar{z}} + \bar{w}\frac{\partial \bar{T}}{\partial \bar{r}} = \frac{\alpha_f}{\bar{r}}\left(\frac{\partial \bar{T}}{\partial \bar{r}} + \bar{r}\frac{\partial^2 \bar{T}}{\partial \bar{r}^2}\right) + \tau\left[D_B \frac{\partial \bar{T}}{\partial \bar{r}}\frac{\partial \bar{C}}{\partial \bar{r}} + \frac{D_T}{T_\infty}\left(\frac{\partial \bar{T}}{\partial \bar{r}}\right)^2\right] + \frac{1}{(\rho C_p)_f}\frac{\partial}{\partial \bar{r}}\left(\frac{16\sigma *}{3kk^*}\bar{T}^3 \frac{\partial \bar{T}}{\partial \bar{r}}\right) \tag{3}$$

$$\bar{u}\frac{\partial \bar{C}}{\partial \bar{z}} + \bar{w}\frac{\partial \bar{C}}{\partial \bar{r}} = \frac{D_T C_\infty}{T_\infty}\frac{\partial^2 \bar{T}}{\partial \bar{r}^2} + D_B \frac{\partial^2 \bar{C}}{\partial \bar{r}^2} - Kr^2 \left(\frac{\bar{T}}{T_\infty}\right)^n exp\left(\frac{-E_a}{K_B \bar{T}}\right)(C_\infty - \bar{C}) \tag{4}$$

$$\bar{u}\frac{\partial \bar{N}}{\partial \bar{z}} + \bar{w}\frac{\partial \bar{N}}{\partial \bar{r}} = D_N \frac{\partial^2 \bar{N}}{\partial \bar{r}^2} - \frac{bW_c}{C_\infty}\frac{\partial}{\partial \bar{r}}\left(\bar{N}\frac{\partial \bar{C}}{\partial \bar{r}}\right) \tag{5}$$

The boundary conditions of problem typically match the configurations under investigation, as stated below:

$$\bar{r} = R, \ \ \bar{u} = 0, \ \ \bar{w} = u_w, \ \ k_f \frac{\partial \bar{T}}{\partial \bar{r}} = -h_w(T_w - \bar{T}), \ \ \bar{N} = N_w, \ \ D_B\left(\frac{\partial \bar{C}}{\partial \bar{r}}\right) + \frac{D_T}{T_\infty}\left(\frac{\partial \bar{T}}{\partial \bar{r}}\right) = 0, \tag{6}$$

$$\bar{r} \to \infty, \quad \bar{u} \to 0 \quad \bar{C} \to C_\infty, \quad \bar{T} \to T_\infty, \quad \bar{N} \to N_\infty$$

The provided similarity transformations below are employed.

$$\xi = \frac{r^2 - R^2}{2R}\sqrt{\frac{u_w}{z\mu_f}}, \quad u = f'(\xi)\frac{zu_o}{L}, \quad w = -\frac{R}{r}f(\xi)\sqrt{\frac{u_o\mu_f}{L}}$$
$$\theta(\xi) = \frac{T_\infty - \bar{T}}{T_\infty - T_w}, \quad \phi(\xi) = \frac{C_\infty - \bar{C}}{C_\infty - C_w}, \quad \chi(\xi) = \frac{N_\infty - \bar{N}}{N_\infty - N_w} \tag{7}$$

In Equation (7), ξ signifies the local transformation variable, $f'(\xi)$ represents the dimensionless velocity function, and $\theta(\xi)$ denotes the non-dimensionalized fluid temperature. Moreover, $\phi(\xi)$ represents the dimensionless volume fraction of nanoparticles, while $\chi(\xi)$ represents a motile microorganism lacking dimensional attributes. Equation (1) is identically satisfied. After the utilization of the above-mentioned transformation Equations (2)–(5), we got a subsequent scheme of ODEs.

$$\alpha(1 + 2\gamma\xi)[1 + (2 - \alpha)(\beta f'')^{\alpha-1}]f''' + \gamma[1 + (2 - \alpha)(\beta f'')^{\alpha-1}]f'' - [((1 + \beta f'')^{\alpha-1})^2]Mf' - [(1 + \beta f'')^{\alpha-1}]^2\sigma_1 f' + [(1 + \beta f'')^{\alpha-1}]^2[ff'' - F_r(f')^2 - (f')^2] + \aleph[\theta - N_r\phi - N_c\chi] \tag{8}$$

$$\frac{4}{3}Rd[(1 + (\theta_w - 1)\theta)^3](1 + 2\gamma\xi)\theta'' + 4Rd(\theta')^2[(1 + (\theta_w - 1)\theta)^2(\theta_w - 1)] + 2\gamma\theta' + N_b\theta'\phi' + N_t(\theta')^2 + Prf\theta' = 0 \tag{9}$$

$$\phi'' + f'\phi'Le\frac{\xi}{2} + Lef\phi' + \frac{N_t}{N_b}(\theta'' + \gamma\theta') - Le\Omega(1 + \Upsilon^*\theta)^n exp(\frac{-E}{1 + \Upsilon^*\theta})\phi = 0 \tag{10}$$

$$\chi'' + Lb(f\chi' + \xi f'\chi) + Pe[\delta_1\phi' - (\gamma\delta_1 + \chi)\phi''] + Lb\chi'\phi = 0 \tag{11}$$

The subsequent boundary conditions are provided as:

When $\xi = 0;\ f(\xi) = 0,\ f'(\xi) = 1,$

$$\theta'(\xi) = -Bi[1 - \theta(\xi)], \quad \phi'(\xi) + \frac{N_t}{N_b}\theta'(\xi) = 0, \quad \chi(\xi) = 1 \tag{12}$$

When $\xi \to 0; f'(\xi) \to 0,\ \theta(\xi) \to 0,\ \phi(\xi) \to 0,\ \chi(\xi) \to 0.$

Additionally, the dimensionless numbers and parameters within the above equations are as follows:

$$M = \frac{\sigma_f B_o^2 z}{\rho_f u_w}, F_r = \frac{C_b}{\sqrt{k*}}, \gamma = \frac{1}{R}\sqrt{\frac{L\mu_f}{u_o}}, Rd = \frac{4\sigma T_\infty^3}{K^* k_f}, \beta = \sqrt{\frac{u_o^3 z^2 r^2}{2\tau_o^4 R^2 L^3 \mu_f}}, \sigma_1 = \frac{z\mu_f}{k^* u_w}, Bi = \frac{h_w}{k\mu_f}\sqrt{u_o^{-1}\nu_f}, Pr = \frac{\nu_f (C\rho)_f}{k_f}, N_r = \frac{\beta_c(C_\infty - C_w)(\rho_p - \rho_f)}{(1 - C_\infty)(T_\infty - T_w)\beta_t\rho_f}, N_c = \frac{(\rho_m - \rho_f)\gamma^*(N_\infty - N_w)}{(1 - C_\infty)(T_\infty - T_w)\beta_t\rho_f},$$
$$\aleph = \frac{G_{rt}}{Re_x^2}, G_{rt} = \frac{(1 - C_\infty)\beta_t g(T_\infty - T_w)z^3}{2\nu_f^2}, Re_x^2 = \frac{u_w(z)}{\nu_f}, N_b = \frac{\tau D_B(C_\infty - C_w)}{\nu_f}, E = \frac{E_a}{K_B T_\infty} \tag{13}$$
$$N_t = \frac{\tau D_T(T_\infty - T_w)}{\nu_f T_\infty}, \theta_w = \frac{T_w}{T_\infty}, Le = \frac{\nu_f}{D_B}, \Omega = \frac{zkr^2r^2}{u_w R^2}, Lb = \frac{\mu_f}{D_N}, \delta_1 = \frac{N_\infty}{N_\infty - N_w}, \Upsilon^* = \frac{T_\infty - T_w}{T_\infty}$$

Here, M symbolizes the magnetic term, F_r is the Forchheimer number, γ represents the curvature parameter, Rd indicates the thermal radiation parameter, β signifies the Ellis fluid parameters, σ_1 denotes the porosity parameter, Bi stands for the thermal Biot number, Pr signifies the Prandtl number, and N_r represents the buoyancy force parameter. Bioconvection Rayleigh number N_c, $\aleph$ is the parameter for mixed convection, G_{rt} are the Grashof number, Re_x is the local Reynolds number, E activation energy parameter, N_t, θ_w, Le are the parameter of thermophoresis, temperature ratio parameter, Lewis number respectively. Furthermore, Ω represents the coefficient of chemical reaction, Lb stands for the bioconvection Lewis number, δ_1 denotes the parameter of bacterial concentration, and Υ^* signifies the temperature gradient.

3. Physical quantities

3.1. Drag force acting on the surface

The skin friction coefficient is characterized as:

$$C_f = \frac{\tau_w}{\rho_f u_w^2} \tag{14}$$

where τ_w represents the apparent shear stress, defined as follows:

$$\tau_w = [\frac{\mu_f}{1 + (\frac{1}{\sqrt{2}\tau_o^2}\frac{\partial \bar{u}}{\partial z})^{\alpha-1}}\frac{\partial \bar{u}}{\partial z}]|_r = 0 \tag{15}$$

The provided similarity transformation enabled us to acquire:

$$C_f = Re_x^{\frac{-1}{2}}(\frac{f''(0)}{(1+\beta f'')^{\alpha-1}}) \tag{16}$$

3.2. The heat transfer rate

The Nusselt coefficient at a specific point is calculated as:

$$Nu_x = \frac{x q_m^*}{k_f(T_\infty - T_w)} \tag{17}$$

Therefore, the surface heat flux is expressed as:

$$q_m^* = -k_f(\frac{\partial \bar{T}}{\partial r})|_{r=0} - \frac{16\sigma^*}{3k^*}\bar{T}^3(\frac{\partial \bar{T}}{\partial r})|_{r=0} \tag{18}$$

The dimensionless form of the aforementioned equation is obtained by employing Equation (7) as follows:

$$Nu = -Re_x^{\frac{1}{2}}(1 + \frac{4}{3}Rd)\theta'(0) \tag{19}$$

3.3. Motile microorganisms

The quantity of motile microorganisms within the local density is described as:

$$Nn_x = \frac{x q_n}{D_N(N_\infty - N_w)} \tag{20}$$

where, motile microorganism flux defined as

$$q_n = -D_N\frac{\partial \bar{N}}{\partial r}|_{r=0} \tag{21}$$

The equation is expressed in its non-dimensionalized form as:

$$Nn = -Re_x^{\frac{1}{2}}\chi'(0) \tag{22}$$

4. Details of numerical procedure

Given the intricate nature of analytically solving ordinary differential equations (ODEs), we turn to numerical methods like the shooting method implemented through MATLAB’s bvp4c software to tackle the governing equations. The core of bvp4c lies in its ability to transform the BVP into an IVP through the proposal of an initial solution. Numerous physical models involve nonlinear differential equations requiring numerical solutions, and the shooting method excels in achieving high accuracy. This technique transforms boundary value problems into initial value problems, iteratively adjusting initial conditions and integrating using methods like Runge-Kutta. Its effectiveness in solving complex flow models yields precise insights into fluid behavior. Consequently, we utilized this approach to address Equations (8)–(12). Shampine et al. [46] furnished a comprehensive description of Bvp4c. **Figure 2** shows the flow chart of the current investigation. Additionally, several new variables were introduced, outlined as follows:

$$\begin{gathered} f = p_1, f' = p_2, f'' = p_3, f''' = {p_3}', \\ \theta = p_4, \theta' = p_5, \theta'' = {p_5}', \\ \phi = p_6, \phi' = p_7, \phi'' = {p_7}', \\ \varphi = p_8, \varphi' = p_9, \varphi'' = {p_9}', \end{gathered} \tag{23}$$

$$\begin{aligned} {p_3}' = {} & \frac{1}{\alpha(1+2\gamma\xi)[1+(2-\alpha)(\beta p_3)^{\alpha-1}]} \times [-\gamma[1+(2-\alpha)(\beta p_3)^{\alpha-1}]p_3 + [((1+\beta p_3)^{\alpha-1})^2]Mp_2 + [(1 \\ & + \beta p_3)^{\alpha-1})]^2\sigma_1 p_2 - [(1+\beta p_3)^{\alpha-1}]^2[p_1p_3 - F_r(p_2)^2] - \aleph[p_4 - N_r p_6 - N_c p_8]] \end{aligned} \tag{24}$$

$$\begin{aligned} {p_5}' = {} & \frac{1}{\frac{4}{3}Rd[(1+(\theta_w-1)p_4)^3](1+2\gamma\xi)} \times [-4Rd(p_5)^2[(1+(\theta_w-1)p_4)^2(\theta_w-1)] - 2\gamma p_5 - N_b p_5 p_7 \\ & - N_t(p_5)^2 - Prp_1p_5] \end{aligned} \tag{25}$$

$${p_7}' = -p_2p_7Le\frac{\xi}{2} - Lep_1p_7 - \frac{N_t}{N_b}({p_5}' + \gamma p_5) + Le\Omega(1+\Upsilon^* p_4)exp(\frac{-E}{1+\Upsilon^* p_4})p_6 \tag{26}$$

$${p_9}' = -Le(p_1p_9 + \xi p_2p_8) - Pe[\sigma_1 p_7 - (\gamma\sigma_1 + p_8){p_7}'] - Lep_9p_6 \tag{27}$$

Together with the associated boundary conditions:

$$\begin{gathered} p_1(0) = 0,\ \ p_2(0) = 1,\ \ p_5(0) = -Bi[1-p_4(0)],\ \ \ p_7(0) + \frac{N_t}{N_b}p_5(0) = 0, \\ p_8(0) = 1,\ \ \text{at}\ \xi = 0 \end{gathered} \tag{28}$$

$$p_2 \to 0,\ \ p_4 \to 0,\ \ p_6 \to 0,\ \ p_8 \to 0,\ \ \text{at}\ \xi \to 0 \tag{29}$$

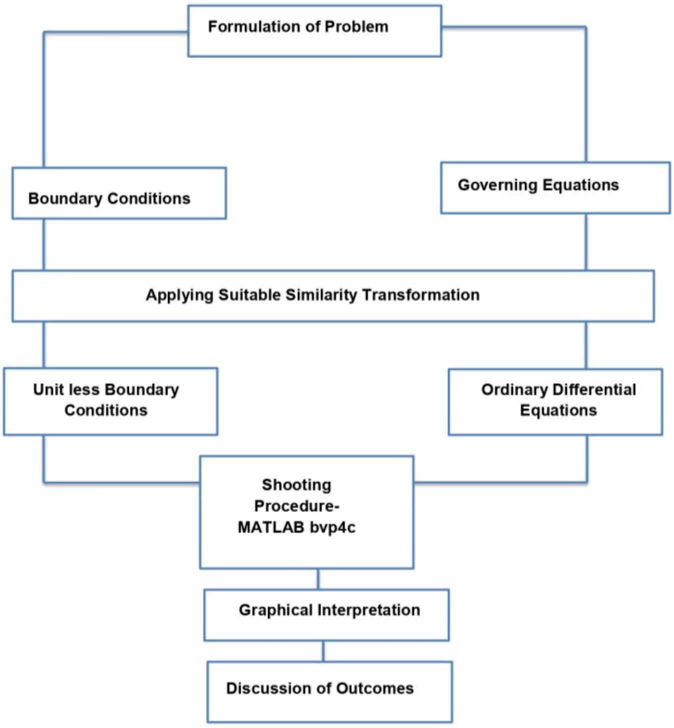

Figure 2. Flow chart for current problem.

5. Results and discussion

This part elucidates the graphs of physical characteristics such as distribution of velocity component $f'(\xi)$, distribution of temperature $\theta(\xi)$, distribution of concentration of nanoparticles $\phi(\xi)$, and distribution of motile oxytactic microorganisms $\chi(\xi)$. In the process of altering the physical variables of our interest, the variables left behind have been assigned these values $0.5 \leq M \leq 3.5$, $0.4 \leq Bi \leq 4.5$, $0.5 \leq Rd \leq 1$, $0.2 \leq \gamma \leq 0.8$, $m = 3$, $0 \leq \sigma_1 \leq 1$, $0.5 \leq \theta_w \leq 2$, $4 \leq Fr \leq 15$, $1 \leq \beta \leq 5$, $Pr = 1$ and $n = 1$.

5.1. Velocity profile

The persuasion of the slip parameter α, the magnetization factor M, the thermal radiation parameter Rd, the microorganism concentration difference constant Ω, and the parameter for buoyancy ratio Nr on the fluid speed $f'(\xi)$ is depicted in **Figure 3a–e**. The effects of the magnetization factor M on velocity graph $f'(\xi)$ is manifested in **Figure 3a**. A declining behaviour is prominent for velocity distribution by increasing the magnetization factor M. For higher values of (M = 0.5, 1.5, 2.5, 3.5), **Figure 3a** shows a decreasing trend of $f'(\xi)$. Because it depends on Lorentz force, the interparticle resistance increases as increases, which reduces $f'(\xi)$. The consequence of the slip parameter α on the velocity graph $f'(\xi)$ is shown in **Figure 3b**. By increasing α, an increase in velocity distribution is observed. Because, the presence of slip effectively increases the speed of particles in fluid. Similarly, the results for the radiation parameter Rd shown in **Figure 3c**. As the radiation constant Rd increases, the velocity distribution $f'(\xi)$ raises. Solar radiation can help in improving different heat and thermal moulding procedures in the twenty-first century. **Figure 3d** shows the effects of the microorganism concentration difference constant Ω. It is evident from the graph that there is a decline in velocity profile for changing values of Ω. The graphical results for the parameter for buoyancy ratio Nr is shown in **Figure 3(e)**. As the values of the parameter for buoyancy ratio Nr increases, the velocity distribution $f'(\xi)$ also shows an increasing trend.

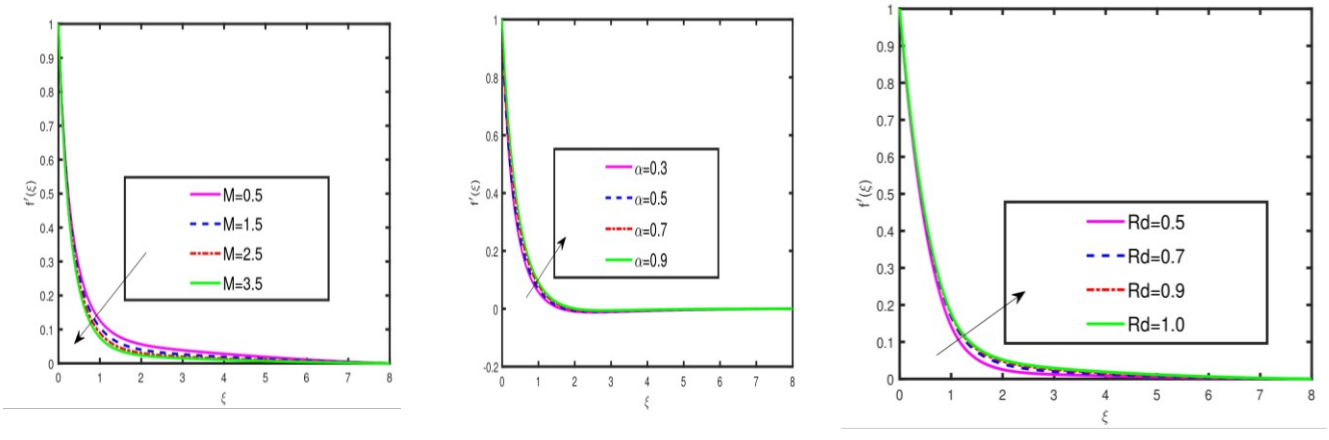

(a) **(b)** **(c)**

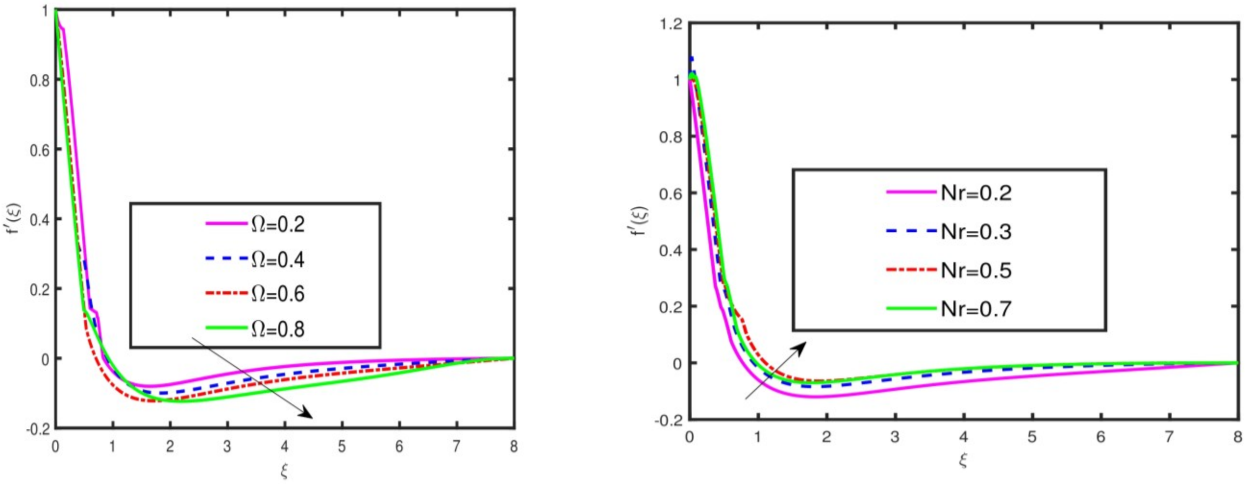

(d) **(e)**

Figure 3. Influence of **(a)** *M*; **(b)** *α*; **(c)** *Rd*; **(d)** *Ω*; **(e)** *Nr* on $f'(\xi)$.

5.2. Temperature distribution profile

The influences of the magnetization factor M, the thermal radiation parameter Rd, the thermophoresis parameter Nt, the curvature parameter γ and the bioconvention Peclet number Pe on the fluid speed $\theta(\xi)$ is shown in **Figure 4a–e**. Effects of the magnetization factor M on temperature field $\theta(\xi)$ is portrayed in **Figure 4a**. A declining behaviour is prominent for temperature distribution by increasing the magnetization factor M. For higher values of (M = 0.5, 1.5, 2.5, 3.5), **Figure 4a** shows a decreasing trend of $\theta(\xi)$. Because it depends on Lorentz force, the interparticle resistance increases as it increases, which reduces $\theta(\xi)$. The results for and the thermophoresis parameter Nt, as well as the thermal radiation parameter Rd is illustrated in **Figure 4b,c** respectively. For Nt, a declining behaviour of $\theta(\xi)$ observed in **Figure 4b**. The thermophoresis phenomenon is important in many processes because it involves migrating nanoparticles in a low temperature zone due to temperature differences. Similarly, the results for the radiation parameter Rd shown in **Figure 4c**. As the radiation constant Rd increases, the temperature distribution $\theta(\xi)$ changes. In **Figure 4d,e**, the effects of the bio convention Peclet number Pe and the curvature parameter γ are plotted. By altering Pe, a retarding behavior is discovered; this tendency establishes because Pe develop a reverse relationship with temperature field. $\theta(\xi)$ reduced as a result of this inverse relationship. **Figure 4e** demonstrates how the curvature parameter impacts the temperature profile of Ellis nanofluid. The temperature profile $\theta(\xi)$ decreases as the curvature parameter γ increases, leading to a reduction in the heat transfer rate.

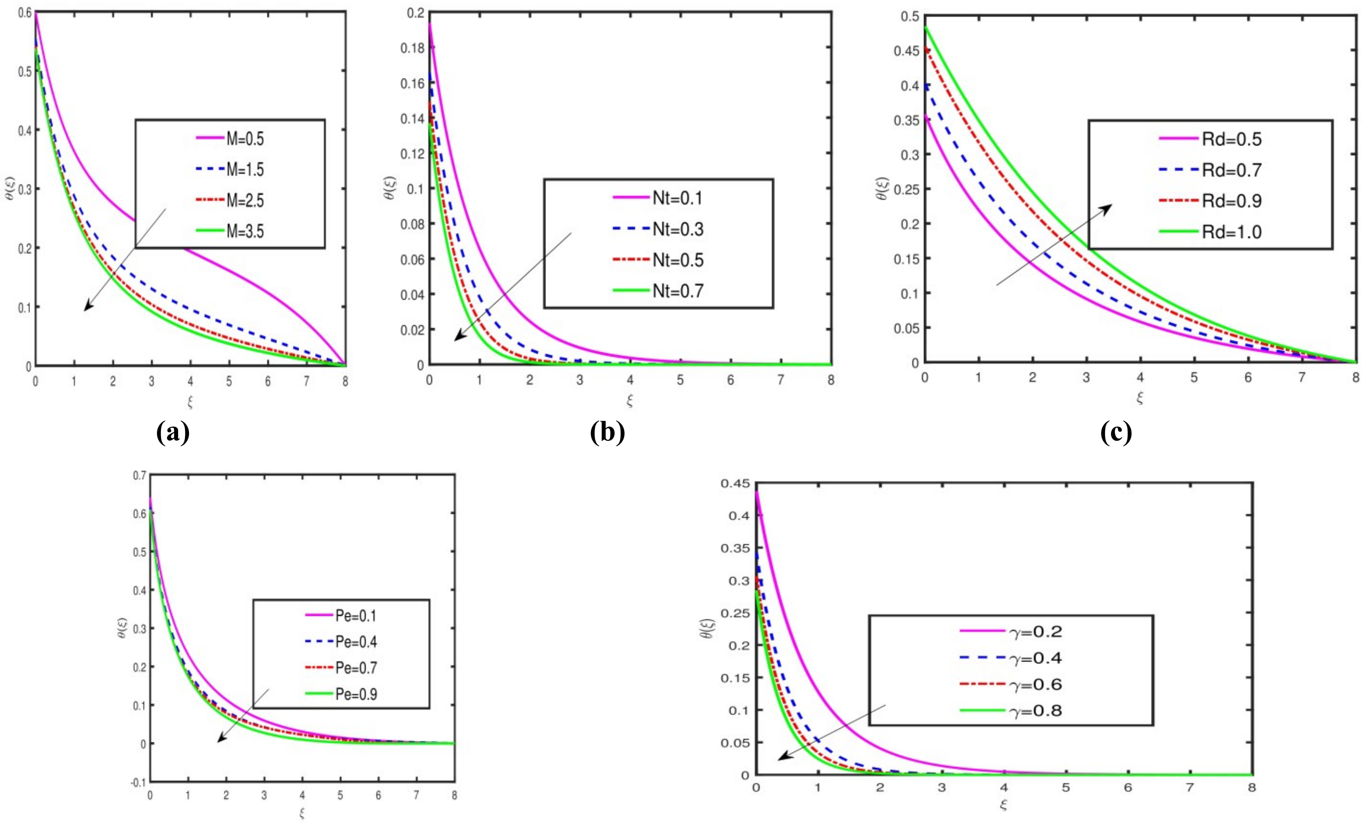

(a) **(b)** **(c)**

(d) **(e)**

Figure 4. Influence of **(a)** *M*; (b) *Nt*; **(c)** *Rd*; **(d)** *γ*; **(e)** *Pe* on *θ*(*ξ*).

5.3. Concentration profile significance

To examine changes in profile for concentration of nanoparticles $\phi(\xi)$ opposite different values of magnetization factor M, the thermal radiation parameter Rd, the Brownian movement parameter Nb, Lewis number Le and the Forchheimer number Fr **Figure 5a–e** are made. Effects of the magnetization factor on $\phi(\xi)$ is displayed in **Figure 5a**. An increasing behaviour is prominent for $\phi(\xi)$ by increasing the magnetic parameter M. For higher values of (M = 0.5, 1.5, 2.5, 3.5), **Figure 5a** shows an increasing trend of $\phi(\xi)$. **Figure 5b** indicates how the effects on $\phi(\xi)$ on Ellis nanofluid increases as the amounts of the Fr rise. Similarly, the results for the radiation parameter Rd are shown in **Figure 5c**. As the radiation constant Rd increases, the temperature distribution $\phi(\xi)$ first increases then shows a declining trend. The ramifications of yet two other crucial parameters, the Lewis number Le and the Brownian movement parameter Nb are shown in **Figure 5d**,**e** respectively. Although the concentration of nanoparticles decreases with Le but for Nb the profile for concentration of nanoparticles improves.

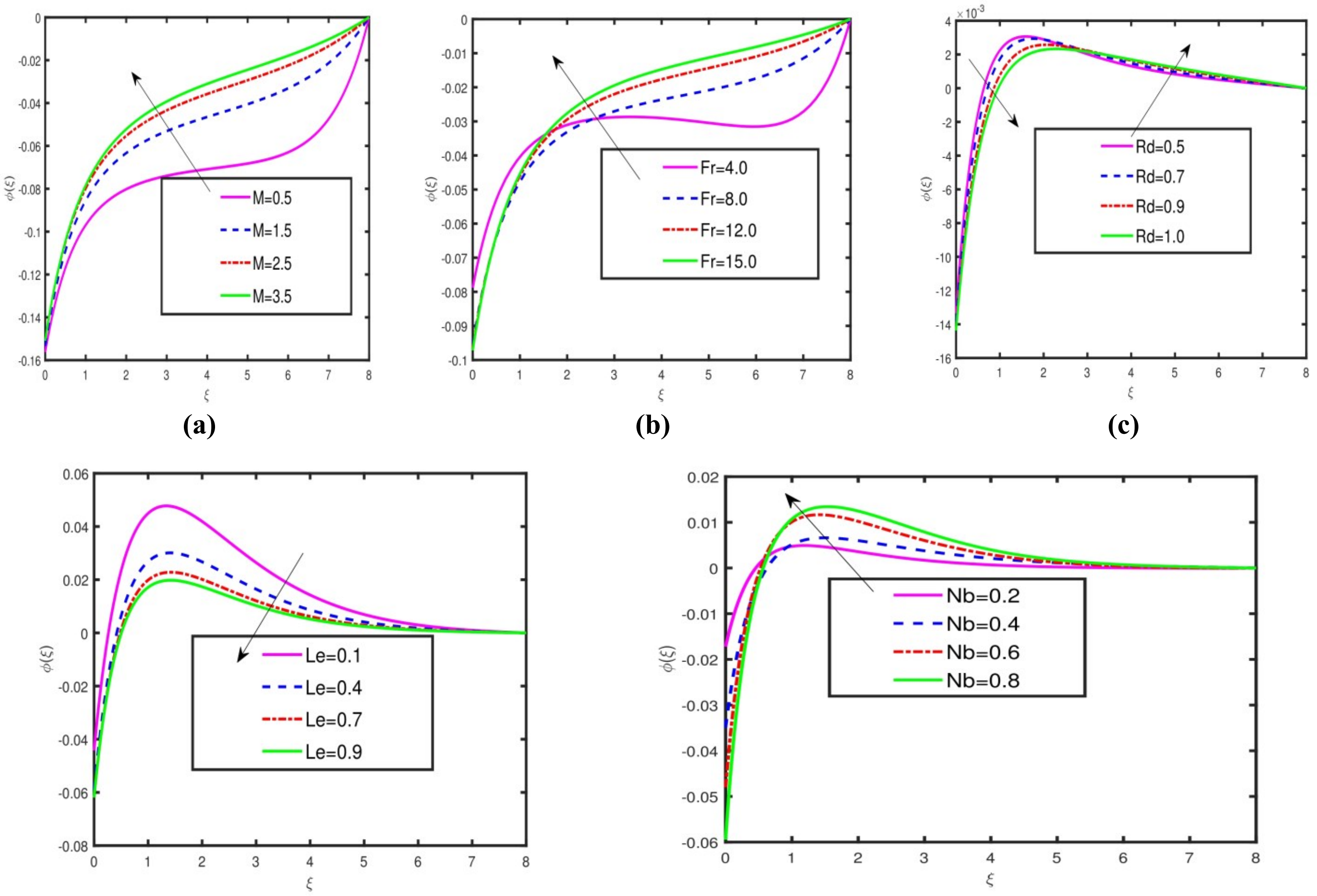

(a) **(b)** **(c)**

(d) **(e)**

Figure 5. Influence of **(a)** *M*; **(b)** *Fr*; **(c)** *Rd*; **(d)** *Le*; **(e)** *Nb* on $\phi(\xi)$.

5.4. Density of motile microorganism profile

Figure 6a–e shows the changes in the profile for independently moving microorganisms $\chi(\xi)$ for various parameters such as thermal Biot number Bi, stretching parameter β, magnetization factor M, Prandtl number Pr and Lewis parameter Lb on profile for independently moving microorganism $\chi(\xi)$. **Figure 6a** is prepared to depict the physical impact caused by thermal Biot number Bi on $\chi(\xi)$. It is easy to observe that $\chi(\xi)$ is a decreasing function of (Bi= 0.4, 1.5, 3.0, 4.5). As thermal Biot number has a connection to the coefficient of heat transfer, that causes a decrease in the independently moving microorganisms $\chi(\xi)$. An increasing behaviour is prominant for $\chi(\xi)$ by increasing the magnetic parameter M. For higher values of (M = 0.5, 1.5, 2.5, 3.5), **Figure 6b** shows an increasing trend of $\chi(\xi)$. The stretching parameter β for the dimensionless independently moving microorganisms $\chi(\xi)$ is graphed in **Figure 6c**. The profile for independently moving microorganisms $\chi(\xi)$ decreases as β increased. **Figures 6d,e** are prepared to depict the physical impact caused by Pr and Lb on independently moving microorganisms $\chi(\xi)$. It is easy to observe that $\chi(\xi)$ is a decreasing function of (Pr = 10, 12, 14, 16). Further, a distinguishing motile microorganism profile $\chi(\xi)$ is found when the value of Lb increases. The physical reasoning is that a bigger deviation in Lb is connected with reduced motility of motile bacteria, which decays $\chi(\xi)$ as a result of this.

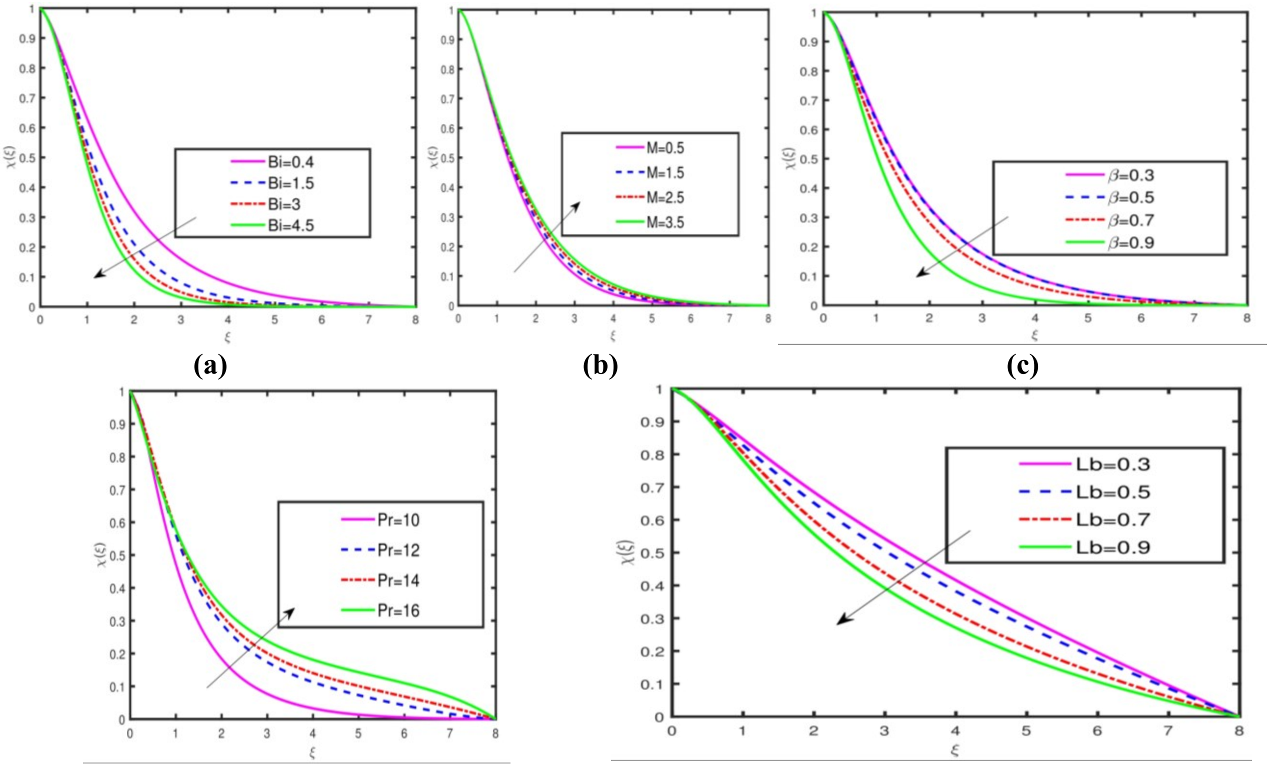

(a) **(b)** **(c)**

(d) **(e)**

Figure 6. Influence of **(a)** *Bi*; **(b)** *M*; **(c)** β; **(d)** *Pr*; **(e)** *Lb* on $\chi(\xi)$.

5.5. Streamlines patterns in Ellis nanofluid flow

This subsection illustrates the streamlines for the mixed convection parameter and slip parameter, as shown in **Figure 7a–d**. The graphs demonstrate the significant impact of both the mixed convection parameter $\aleph$and the slip parameter α on fluid dynamics. When $\aleph = 0.7$ the streamlines are densely packed near the surface, indicating a sharper velocity gradient and stronger convective flow due to buoyancy forces. In contrast, a lower mixed convection value $\aleph = 0.2$ results in smoother, less curved streamlines, highlighting the dominance of viscous forces. Regarding the slip parameter α, increasing it from 1.5 to 2.5 reduces boundary layer thickness and curvature of the streamlines, suggesting less friction and shear stress at the boundary, which enhances flow efficiency. This effect is particularly beneficial for applications like microfluidics, where minimizing drag is crucial. Conversely, lower α values result in thicker boundary layers and greater resistance, slowing down the fluid flow (see **Figure 7c,d**). Overall, mixed convection controls the intensity of surface flow, while the slip parameter governs flow resistance, both essential for optimizing fluid dynamics in systems that require precise control, such as microfluidic devices.

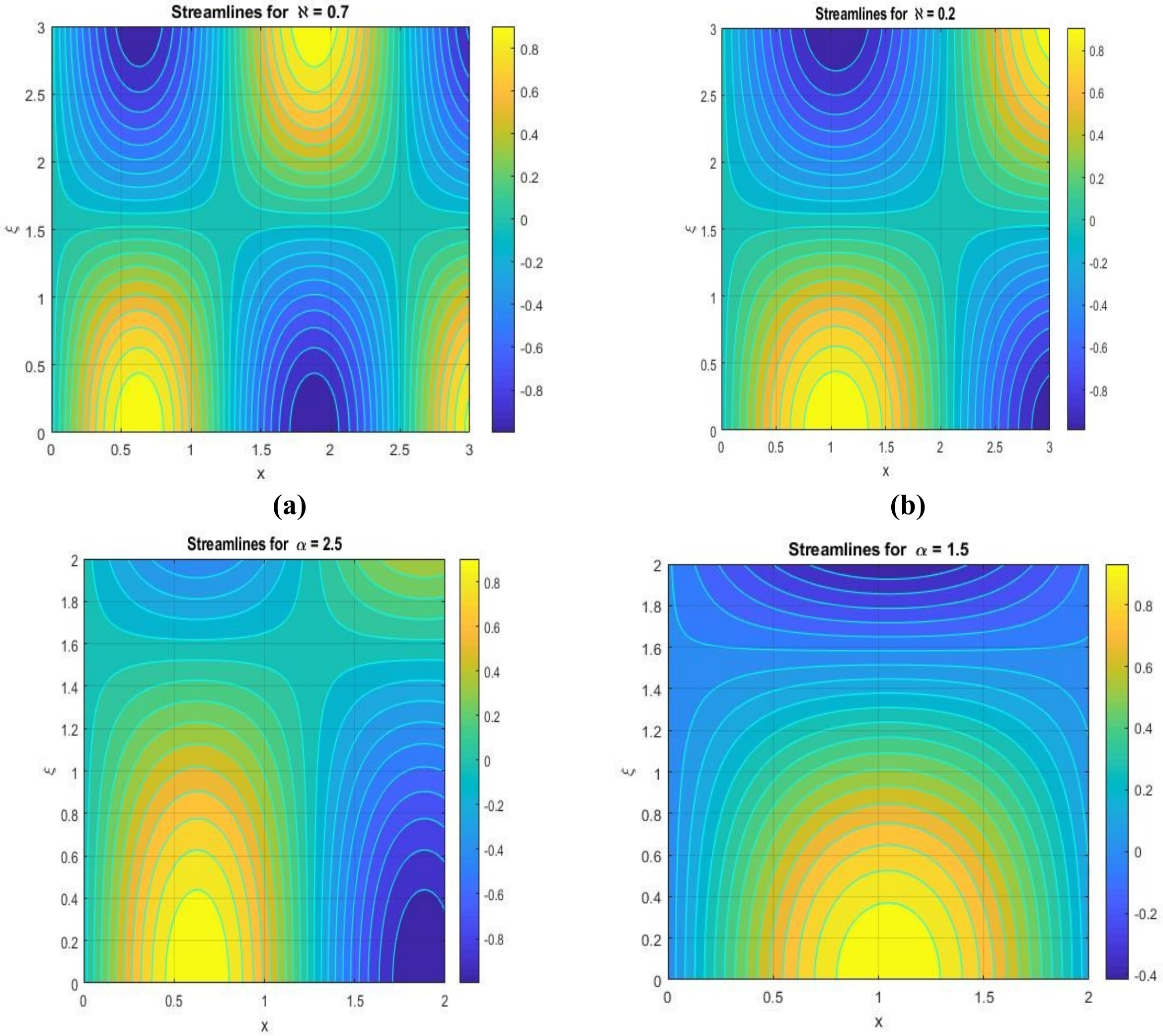

(a) **(b)**

(c) **(d)**

Figure 7. Streamlines for **(a)** ℵ = 0.7, **(b)** ℵ = 0.2, **(c)** α = 2.5, **(d)** α = 1.5.

5.6. Isotherm patterns in Ellis nanofluid flow

The isotherm patterns depicted in **Figure 8a–d** offer profound insights into the thermal dynamics of Ellis nanofluid flow, particularly with respect to the Ellis fluid parameter β and porosity parameter σ_1. In **Figure 8a**, where ($\beta = 0.7$), the closely packed isotherms near the center indicate a steeper temperature gradient, signifying enhanced heat transfer and thermal conduction within the fluid. On the other hand, **Figure 8b**, with a lower ($\beta = 0.5$), shows more widely spaced isotherms, suggesting a gentler temperature gradient and reduced heat conduction, which reflects a decline in thermal efficiency. Focusing on the porosity parameter, **Figure 8c** illustrates that a higher ($\sigma_1 = 1.5$) results in a well-structured, periodic isotherm pattern, promoting more effective thermal dissipation throughout the fluid. In contrast, **Figure 8d**, where ($\sigma_1 = 1.1$), reveals elongated and less organized isotherms, indicating diminished heat transfer efficiency due to increased thermal resistance at the boundaries. These findings highlight the critical roles of elevated β and σ_1 values in optimizing heat conduction and distribution within the Ellis nanofluid flow.

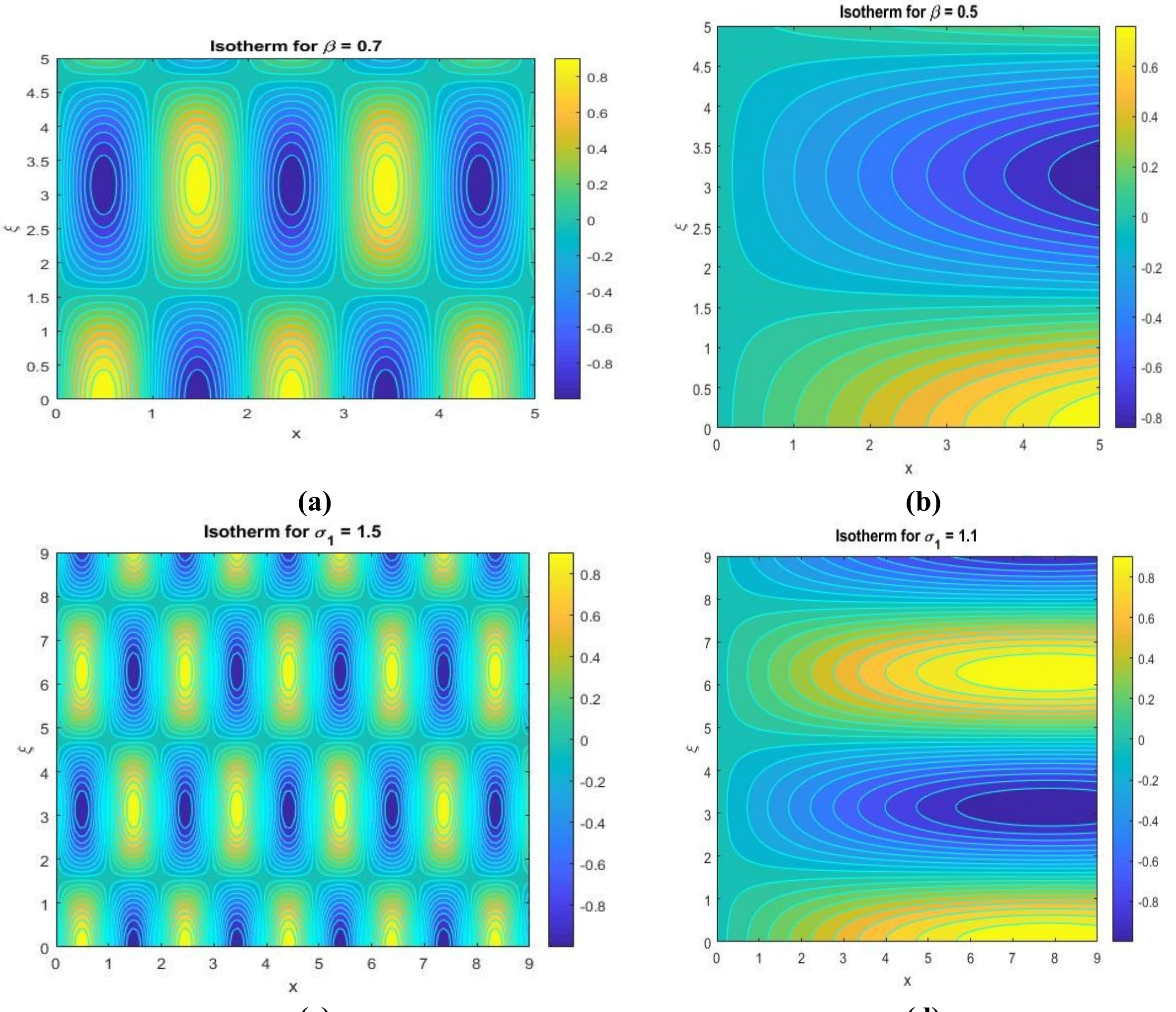

(a) **(b)**

(c) **(d)**

Figure 8. Isotherms for **(a)** $\beta = 0.7$, **(b)** $\beta = 0.5$, **(c)** $\sigma_1 = 1.5$, **(d)** $\sigma_1 = 1.1$.

5.7. Tabular discussion and validation

To validate this research, we compared the skin friction values with those reported by Rooman et al. [47] and Awan et al. [44] under specific conditions where M varies and all other parameters are set to zero, ensuring optimal heat and mass transfer in our model. The results demonstrate excellent agreement with existing literature (see **Table 1**).

Table 1. A comparison of $f'(0)$ for different inputs of M.

M	**Rooman et al. [47]**	**Awan et al. [44]**	**Current result**
0.0	−0.821821	−0.8266554	−0.8267556
0.4	−0.924421	−0.9186823	−0.9286826
0.8	−1.018311	−1.0488087	−1.0588092

6. Conclusion

Numerical analysis was conducted to explore the steady mixed convection of Ellis nano-liquid flow over a stretching cylinder, incorporating Darcy-Forchheimer and nonlinear thermal radiation effects. The numerical solution of this model involves formulating a system of partial differential equations, which is subsequently computed by utilizing the bvp4c function available in MATLAB. The acquired outcomes are visually presented and analyzed. The following observations have been made after a thorough examination of the problem:

- Increasing the magnetization factor M results in a decreasing velocity profile $f'(\xi)$ due to the stronger Lorentz force increasing interparticle resistance.
- An augmentation in the Peclet number (Pe) and thermophoresis value results in a decline in the thermal layer.
- The Ellis fluid parameter β results in a decrease in the motile density profile $\chi(\xi)$.
- Brownian motion enhances the thermal profile, while saturation in thermophoresis values leads to a decrease in flow.
- It has been uncovered that an increased approximation of the Forchheimer number results in an enlargement of the concentration profile $\phi(\xi)$.
- Our study demonstrates that varying the radiation parameter (Rd) provides valuable insights into the behavior of Ellis nanofluids under magnetized bioconvective conditions, emphasizing the significance of considering multiple factors for a comprehensive understanding of the fluid dynamics.
- Lower mixed convection values allow viscous forces to dominate, leading to smoother, less curved streamlines.
- Increased porosity parameter σ_1 values produce well-structured isotherms, promoting efficient thermal dissipation throughout the fluid.

Future research in this domain should explore the ramification of variable activation energy on the behavior of oxytactic microorganisms within magnetized bioconvective Ellis nanofluids, alongside extending studies to three-dimensional systems for a more comprehensive understanding. Experimental validation is essential to enhance credibility, while investigating additional dissipative processes like thermal diffusion could provide deeper insights. Further applications in bioengineering and materials science should be explored, considering the impact of external fields and conducting optimization studies to maximize efficiency in practical applications. These endeavors would significantly advance the understanding and application of magnetized bioconvective Ellis nanofluids.

Author contributions: Methodology, TA; software, TA; validation, MA; formal analysis, TA, MA and MC; investigation, TA, MMA and MI; data curation, MMA; writing—original draft preparation, TA and MMA; writing—review and editing, TA, MA, MC and MI; visualization, MA; supervision, MMA and MI. All authors have read and agreed to the published version of the manuscript.

Acknowledgments: The authors express gratitude to the reviewers for their valuable suggestions and comments, contributing to the enhanced clarity of this manuscript.

Conflict of interest: The authors declare no conflict of interest.

Nomenclature

$\bar{r}, \bar{z}$: Cylinderical coordinates (-)
$\bar{u}$: Velocity component along horizontal axis (z-axis) $(\mathrm{m/s})$
$\bar{w}$: Velocity component along radial axis (r-axis) $(\mathrm{m/s})$
$\bar{T}$: Temperature of particles (K)
k: Nanofuid thermal conductivity (W/mK)
M: Magnetic parameter (-)
$\bar{C}$: Concentration of particles $(\mathrm{mol/m^3})$
$\bar{N}$: Microorganism's density (-)
T_w: Surface temperature $((T)$
F_r: Forchheimer number (-)
C_w: Surface concentration (mol/m^3)
Rd: Thermal radiation parameter (-)
N_w: Surface microorganisms (-)
Bi: Thermal Biot number (-)
Pr: Prandtl number (-)
N_r: Parameter of buoyancy force $(-)$
N_c: Bioconvection Rayleigh number $(-)$
G_{rt}: Grashof number $(-)$
T_∞: Ambient temperature (-)
C_∞: Free stream concentration $(\mathrm{mol/m^3})$
N_∞: Ambient microorganisms (-)
Re_x: Local Reynolds number (-)
D_m: Microorganism's difusion coefcient (-)
E: Activation energy parameter (-)
N_t: Thermophoresis parameter (-)
Le: Lewis number (-)
Lb: Bioconvection Lewis number (-)
D_B: Brownian motion coefcient $(\mathrm{m^2/s})$

Greek symbols

γ: Curvature parameter (-)
ν: Kinematic viscosity $(\mathrm{m^2/s})$
β: Ellis Fluid parameters (-)
μ: Dynamic viscosity (g/ms)
σ_1: Porosity parameters (-)
θ_w: Temperature ratio parameter (-)
Ω: Coefficient of chemical reaction (-)
α: Slip parameter (-)
ρ_f: Density of the fluid $(\mathrm{kg/m^3})$
δ_1: Bacterial concentration parameter (-)

References

1. Turkyilmazoglu M. MHD natural convection in saturated porous media with heat generation/absorption and thermal

radiation: closed-form solutions. Archives of Mechanics. 2019; 71(1): 49-64. doi: 10.24423/aom.3049

2. Turkyilmazoglu M. Flow of nanofluid plane wall jet and heat transfer. European Journal of Mechanics - B/Fluids. 2016; 59: 18-24. doi: 10.1016/j.euromechflu.2016.04.007
3. Arafa AAM, Ahmed SE, Allan MM. Peristaltic flow of non-homogeneous nanofluids through variable porosity and heat generating porous media with viscous dissipation: Entropy analyses. Case Studies in Thermal Engineering. 2022; 32: 101882. doi: 10.1016/j.csite.2022.101882
4. Hussain F, Nazeer M, Ghafoor I, et al. Perturbation solution of Couette flow of Casson nanofluid with composite porous medium inside a vertical channel. Nanoscience and Technology: An International Journal. 2022; 13(4): 23-44. doi: 10.1615/nanoscitechnolintj.2022038799
5. Abbas N, Shatanawi W, shatnawi TAM. Thermodynamic study of radiative chemically reactive flow of induced MHD sutterby nanofluid over a nonlinear stretching cylinder. Alexandria Engineering Journal. 2023; 70: 179-189. doi: 10.1016/j.aej.2023.02.038
6. Nadeem S, Khan MN, Abbas N. Transportation of slip effects on nanomaterial micropolar fluid flow over exponentially stretching. Alexandria Engineering Journal. 2020; 59(5): 3443-3450. doi: 10.1016/j.aej.2020.05.024
7. Amjad M, Zehra I, Nadeem S, et al. Influence of Lorentz force and Induced Magnetic Field Effects on Casson Micropolar nanofluid flow over a permeable curved stretching/shrinking surface under the stagnation region. Surfaces and Interfaces. 2020; 21: 100766. doi: 10.1016/j.surfin.2020.100766
8. Ramesh K, Mebarek-Oudina F, Souayeh B. Mathematical Modelling of Fluid Dynamics and Nanofluids. CRC Press; 2023. doi: 10.1201/9781003299608
9. Yahya AU, Salamat N, Huang WH, et al. Thermal charactristics for the flow of Williamson hybrid nanofluid (MoS_2 + ZnO) based with engine oil over a streched sheet. Case Studies in Thermal Engineering. 2021; 26: 101196. doi: 10.1016/j.csite.2021.101196
10. Ahmad F, Abdal S, Ayed H, et al. The improved thermal efficiency of Maxwell hybrid nanofluid comprising of graphene oxide plus silver / kerosene oil over stretching sheet. Case Studies in Thermal Engineering. 2021; 27: 101257. doi: 10.1016/j.csite.2021.101257
11. Gul T, Ahmed Z, Jawad M, et al. Bio-convectional Nanofluid Flow Due to the Thermophoresis and Gyrotactic Microorganism Between the Gap of a Disk and Cone. Brazilian Journal of Physics. 2021; 51(3): 687-697. doi: 10.1007/s13538-021-00888-6
12. Abdal S, Hussain S, Siddique I, et al. On solution existence of MHD Casson nanofluid transportation across an extending cylinder through porous media and evaluation of priori bounds. Scientific Reports. 2021; 11(1). doi: 10.1038/s41598-021-86953-1
13. Narahari M, Sreenadh S, Arunachalam PV. Peristaltic pumping flow of an-Ellis fluid through a circular tube. Bulletin of Pure & Applied Sciences. 2000; 19(1): 493-503.
14. Steller RT. Generalized slit flow of an ellis fluid. Polymer Engineering & Science. 2001; 41(11): 1859-1870. doi: 10.1002/pen.10883
15. Ali N, Abbasi A, Ahmad I. Channel flow of Ellis fluid due to peristalsis. AIP Advances. 2015; 5(9). doi: 10.1063/1.4932042
16. Goud JS, Reddy RH. Peristaltic motion of an Ellis fluid model in a vertical uniform tube with wall properties. International Journal of Civil Engineering and Technology. 2018; 9(1): 847-856.
17. Shaheen N, Alshehri HM, Ramzan M, et al. Soret and Dufour effects on a Casson nanofluid flow past a deformable cylinder with variable characteristics and Arrhenius activation energy. Scientific Reports. 2021; 11(1). doi: 10.1038/s41598-021-98898-6
18. Hayat T, Shafiq A, Alsaedi A. MHD axisymmetric flow of third grade fluid by a stretching cylinder. Alexandria Engineering Journal. 2015; 54(2): 205-212. doi: 10.1016/j.aej.2015.03.013
19. Grigoriadis DGE, Sarris IE, Kassinos SC. MHD flow past a circular cylinder using the immersed boundary method. Computers & Fluids. 2010; 39(2): 345-358. doi: 10.1016/j.compfluid.2009.09.012
20. Anuar NS, Bachok N, Turkyilmazoglu M, et al. Analytical and stability analysis of MHD flow past a nonlinearly deforming vertical surface in Carbon Nanotubes. Alexandria Engineering Journal. 2020; 59(1): 497-507. doi: 10.1016/j.aej.2020.01.024
21. Ramesh K, Mebarek-Oudina F, Ismail AI, et al. Computational analysis on radiative non-Newtonian Carreau nanofluid flow in a microchannel under the magnetic properties. Scientia Iranica. 2023; 30(2): 376-390. doi: 10.24200/sci.2022.58629.5822
22. Mebarek-Oudina F, Dharmaiah G, Balamurugan KS, et al. The Role of Quadratic-Linearly Radiating Heat Source with

Carreau Nanofluid and Exponential Space-Dependent Past a Cone and a Wedge: A Medical Engineering Application and Renewable Energy. Journal of Computational Biophysics and Chemistry. 2023; 22(08): 997-1011. doi: 10.1142/s2737416523420073

23. Khan JA, Mustafa M. A numerical analysis for non-linear radiation in MHD flow around a cylindrical surface with chemically reactive species. Results in Physics. 2018; 8: 963-970. doi: 10.1016/j.rinp.2017.12.067
24. Kuznetsov AV, Avramenko AA. Effect of small particles on this stability of bioconvection in a suspension of gyrotactic microorganisms in a layer of finite depth. International Communications in Heat and Mass Transfer. 2004; 31(1): 1-10. doi: 10.1016/S0735-1933(03)00196-9
25. Geng P, Kuznetsov AV. Settling of bidispersed small solid particles in a dilute suspension containing gyrotactic micro-organisms. International Journal of Engineering Science. 2005; 43(11-12): 992-1010. doi: 10.1016/j.ijengsci.2005.03.002
26. Kuznetsov AV. Non-oscillatory and oscillatory nanofluid bio-thermal convection in a horizontal layer of finite depth. European Journal of Mechanics - B/Fluids. 2011; 30(2): 156-165. doi: 10.1016/j.euromechflu.2010.10.007
27. Bég OA, Prasad VR, Vasu B. Numerical Study of Mixed Bioconvection in Porous Media Saturated with Nanofluid Containing Oxytactic Microorganisms. Journal of Mechanics in Medicine and Biology. 2013; 13(04): 1350067. doi: 10.1142/s021951941350067x
28. Mebarek-Oudina F, Chabani I, Vaidya H, et al. Hybrid-nanofluid magneto-convective flow and porous media contribution to entropy generation. International Journal of Numerical Methods for Heat & Fluid Flow. 2024; 34(2): 809-836. doi: 10.1108/hff-06-2023-0326
29. Dharmaiah G, Mebarek-Oudina F, Balamurugan KS, et al. Numerical Analysis of the Magnetic Dipole Effect on a Radiative Ferromagnetic Liquid Flowing over a Porous Stretched Sheet. Fluid Dynamics & Materials Processing. 2024; 20(2): 293-310. doi: 10.32604/fdmp.2023.030325
30. Akbar NS. Bioconvection peristaltic flow in an asymmetric channel filled by nanofluid containing gyrotactic microorganism. International Journal of Numerical Methods for Heat & Fluid Flow. 2015; 25(2): 214-224. doi: 10.1108/hff-07-2013-0242
31. Bhatti MM, Zeeshan A, Ellahi R. Simultaneous effects of coagulation and variable magnetic field on peristaltically induced motion of Jeffrey nanofluid containing gyrotactic microorganism. Microvascular Research. 2017; 110: 32-42. doi: 10.1016/j.mvr.2016.11.007
32. Dharmaiah G, Mebarek-Oudina F, Rama Prasad JL, et al. Exploration of bio-convection for slippery two-phase Maxwell nanofluid past a vertical induced magnetic stretching regime associated for biotechnology and engineering. Journal of Molecular Liquids. 2023; 391: 123408. doi: 10.1016/j.molliq.2023.123408
33. Abbas IA, Palani G. Effects of magnetohydrodynamic flow past a vertical plate with variable surface temperature. Applied Mathematics and Mechanics. 2010; 31(3): 329-338. doi: 10.1007/s10483-010-0306-9
34. Chakraborty T, Das K, Kundu PK. Framing the impact of external magnetic field on bioconvection of a nanofluid flow containing gyrotactic microorganisms with convective boundary conditions. Alexandria Engineering Journal. 2018; 57(1): 61-71. doi: 10.1016/j.aej.2016.11.011
35. Umar M, Akhtar R, Sabir Z, et al. Numerical Treatment for the Three-Dimensional Eyring-Powell Fluid Flow over a Stretching Sheet with Velocity Slip and Activation Energy. Advances in Mathematical Physics. 2019; 2019: 1-12. doi: 10.1155/2019/9860471
36. Khan SU, Rauf A, Shehzad SA, et al. Study of bioconvection flow in Oldroyd-B nanofluid with motile organisms and effective Prandtl approach. Physica A: Statistical Mechanics and its Applications. 2019; 527: 121179. doi: 10.1016/j.physa.2019.121179
37. Akolade MT, Akhtar T, Awad MM, et al. Bioconvection analysis of EMHD and dissipative Williamson nanofluid over a three dimensional Riga plate with Joule heating effect. International Journal of Modelling and Simulation. 2023: 1-13. doi: 10.1080/02286203.2023.2265524
38. Waqas H, Khan SU, Shehzad SA, et al. Radiative flow of Maxwell nanofluid containing gyrotactic microorganism and energy activation with convective Nield conditions. Heat Transfer—Asian Research. 2019; 48(5): 1663-1687. doi: 10.1002/htj.21451
39. Waqas H, Khan SU, Tlili I, et al. Significance of Bioconvective and Thermally Dissipation Flow of Viscoelastic Nanoparticles with Activation Energy Features: Novel Biofuels Significance. Symmetry. 2020; 12(2): 214. doi: 10.3390/sym12020214
40. Shahid A, Zhou Z, Hassan M, et al. Computational Study of Magnetized Blood Flow in The Presence of Gyrotactic

Microorganisms Propelled Through a Permeable Capillary in A Stretching Motion. International Journal for Multiscale Computational Engineering. 2018; 16(5): 409-426. doi: 10.1615/intjmultcompeng.2018026030

41. Waqas H, Khan SU, Hassan M, et al. Analysis on the bioconvection flow of modified second-grade nanofluid containing gyrotactic microorganisms and nanoparticles. Journal of Molecular Liquids. 2019; 291: 111231. doi: 10.1016/j.molliq.2019.111231
42. Hiba B, Redouane F, Jamshed W, et al. A novel case study of thermal and streamline analysis in a grooved enclosure filled with (Ag–MgO/Water) hybrid nanofluid: Galerkin FEM. Case Studies in Thermal Engineering. 2021; 28: 101372. doi: 10.1016/j.csite.2021.101372
43. Sharif MAR, Mohammad TR. Natural convection in cavities with constant flux heating at the bottom wall and isothermal cooling from the sidewalls. International Journal of Thermal Sciences. 2005; 44(9): 865-878. doi: 10.1016/j.ijthermalsci.2005.02.006
44. Awan AU, Ali B, Shah SAA, et al. Numerical analysis of heat transfer in Ellis hybrid nanofluid flow subject to a stretching cylinder. Case Studies in Thermal Engineering. 2023; 49: 103222. doi: 10.1016/j.csite.2023.103222
45. Alwatban AM, Khan SU, Waqas H, et al. Interaction of Wu's Slip Features in Bioconvection of Eyring Powell Nanoparticles with Activation Energy. Processes. 2019; 7(11): 859. doi: 10.3390/pr7110859
46. Shampine LF, Kierzenka J, Reichelt MW. Solving boundary value problems for ordinary differential equations in MATLAB with bvp4c. Tutorial Notes. 2000; 1-27.
47. Rooman M, Jan MA, Shah Z, et al. Entropy generation and nonlinear thermal radiation analysis on axisymmetric MHD Ellis nanofluid over a horizontally permeable stretching cylinder. Waves in Random and Complex Media. 2022: 1-15. doi: 10.1080/17455030.2021.2020934

Thermal Science and Engineering 2024, 7(3), 9125.
https://doi.org/10.24294/tse.v7i3.9125

Article

Thermodynamic evaluation of an IGCC power plant utilizing allothermal gasification

Nitesh Kumar Choudhary*, **Sourov Ghosh**, **Sujit Karmakar**

Department of Mechanical Engineering, National Institute of Technology Durgapur, West Bengal 713209, India
*** Corresponding author:** Nitesh Kumar Choudhary, nkc.19me1105@phd.nitdgp.ac.in

CITATION

Choudhary NK, Ghosh S, Karmakar S. Thermodynamic evaluation of an IGCC power plant utilizing allothermal gasification. Thermal Science and Engineering. 2024; 7(3): 9125.
https://doi.org/10.24294/tse.v7i3.9125

ARTICLE INFO

Received: 6 July 2024
Accepted: 25 August 2024
Available online: 18 September 2024

COPYRIGHT

Copyright © 2024 by author(s). *Thermal Science and Engineering* is published by EnPress Publisher, LLC. This work is licensed under the Creative Commons Attribution (CC BY) license.
https://creativecommons.org/licenses/by/4.0/

Abstract: The present work conducts a comprehensive thermodynamic analysis of a 150 MW_e Integrated Gasification Combined Cycle (IGCC) using Indian coal as the fuel source. The plant layout is modelled and simulated using the "Cycle-Tempo" software. In this study, an innovative approach is employed where the gasifier's bed material is heated by circulating hot water through pipes submerged within the bed. The analysis reveals that increasing the external heat supplied to the gasifier enhances the hydrogen (H_2) content in the syngas, improving both its heating value and cold gas efficiency. Additionally, this increase in external heat favourably impacts the Steam-Methane reforming reaction, boosting the H_2/CH_4 ratio. The thermodynamic results show that the plant achieves an energy efficiency of 44.17% and an exergy efficiency of 40.43%. The study also identifies the condenser as the primary source of energy loss, while the combustor experiences the greatest exergy loss.

Keywords: allothermal gasification; combined cycle; energy; exergy; Indian coal

1. Introduction

The population in modern times is growing exponentially, which raises the energy demand. The majority of power plants in India use coal as fuel. According to the Ministry of Power of India, 47.28% of electricity comes from coal-based power plants. As of 30 June 2024, India has an installed power generation capacity of 446,189.72 MW, as illustrated in **Figure 1** [1]. Fossil fuel burning and industrial gas emissions are releasing CO_2 into the atmosphere, which is responsible for at least 55% of global warming today. Hence, it is imperative to develop alternative plans for enhancing clean energy approaches, such as producing energy from renewable sources, raising overall plant efficiency, and applying clean technology such as gasification, fuel cells, and CO_2 capture. Gasification is a thermochemical process that converts carbonaceous feedstocks like coal and biomass into syngas with the help of gasifying mediums such as steam with air/oxygen and heat. Carbon monoxide (CO), hydrogen (H_2), and methane (CH_4) are the major combustible constituents of gasification. Due to the high conversion ratio of coal to H_2 and CO, Integrated Gasification Combined Cycle (IGCC) technology is considered one of the most important energy production technologies for the twenty-first century [2]. Several gasification methods are being investigated as a way to improve IGCC performance even further. Among different new techniques of gasification, "allothermal (heated indirectly)" gasification is one of them and is predicted to gain high interest among researchers. In allothermal gasification, the gasifier is heated by a heat exchanger inside the gasifier or by circulating hot bed material, which carries heat from other parts of the system [3]. A laboratory-scale gasifier is examined with concentrated Xe light radiation as an indirect heating source and steam as a gasifying medium, giving a carbon conversion of 88% after 120 min of irradiation [4]. Allothermal gasification of biomass using the heat of combustion of biomass micron fuel (BMF) produces product gas, which has an LHV of 12 MJ/Nm^3 [5]. Simulation of coal gasification coupled with a steam power plant using the gasifying medium as steam and oxy-steam shows net electrical efficiency of 21.38% and 9.80%, respectively [6]. Heat Pipe integrated Gasifier-Solid Oxide Fuel Cell-GT system shows a 55%–72% increase in electrical efficiency with anode gas as a gasifying agent [7].

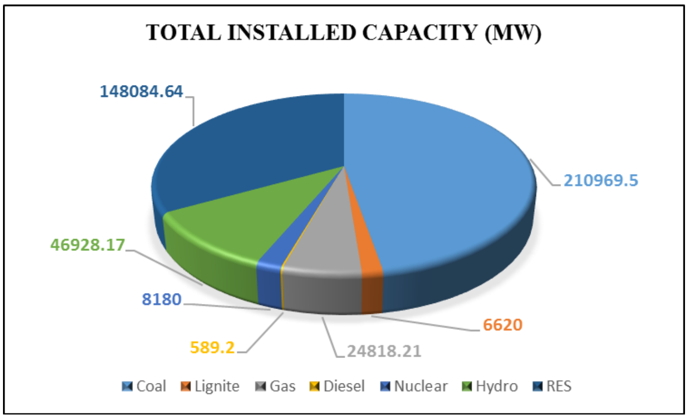

Figure 1. Total power production in India.

The above-mentioned literature shows that the allothermal gasification technique can increase the gasification efficiency in terms of the heating value of syngas and overall plant efficiency. In the present work, it is presented how the external heat of gasification affects the syngas composition and its effect on overall plant performance.

2. Methodology

The Cycle-Tempo software is used to perform an in-depth thermodynamic analysis of the proposed IGCC plant. [8]. This software models the plant as an interconnected system of mechanical and thermal components, which exchange mass and energy with each other and with the external environment. It employed the Gibbs energy minimization method to determine the gas compositions at the exits of the gasifier and compressor. The software operates based on key governing equations, including mass balance, energy balance, and exergy balance, as outlined below:

Mass balance: it refers to the fact to the fact that the total mass within a system remains constant over time unless there is an addition to or removal from the system. Mass balance is used to analyse processes where matter is flowing in and out of a system, such as chemical reactions or fluid flow.

$$\sum_i \dot{m}_i=\sum_e \dot{m}_e \tag{1}$$

Energy balance: it refers to energy conservation within a system. It involves tracking the amount of energy that enters and exits a system and the amount of energy generated or consumed within the system.

$$\sum_i \dot{m}_i h_i+\dot{Q}_{cv}=\sum_e \dot{m}_e h_e+\dot{W}_{cv} \tag{2}$$

Exergy balance: This concept considers the quality of energy within a system, by distinguishing between usable energy (exergy) and unusable energy (anergy).

$$\sum_i \dot{m}_i\Psi_i+\dot{X}_{heat}=\sum_e \dot{m}_e\Psi_e+\dot{W}_{cv}+\dot{I} \tag{3}$$

2.1. Plant configurations

Figure 2 illustrates the configuration of the IGCC plant, which includes a gasifier that uses Indian coal as a feedstock with steam as a gasifying medium. The ash separator receives the syngas from the gasifier, which mostly contains CO and H_2. It is worth mentioning that no syngas cooling unit is needed to attach to the model as the syngas temperature is lower than the ash softening temperature (1400 °C) [9]. It is assumed that 100% ash is separated and the clean syngas reaches the combustion chamber, where it is combusted with compressed air. After combustion, the hot flue gases expand in the gas turbine, producing power. After expansion, the flue gas passes through two heat exchangers, HX1 and HX2. Water is pumped at 10 bar through the heat exchanger (HX1), where it is converted into steam at 190 °C. The heat exchanger shown in the gasifier component of the Cycle-Tempo software is for cooling purposes of the syngas, where atmospheric water is passed through that heat exchanger and cooled down the syngas. But in this model, the bed material of the gasifier is heated by that heat exchanger. The simulation shows quite similar effects on the conversion of coal to syngas as that of indirect heating of bed material found in different literature [4,10].

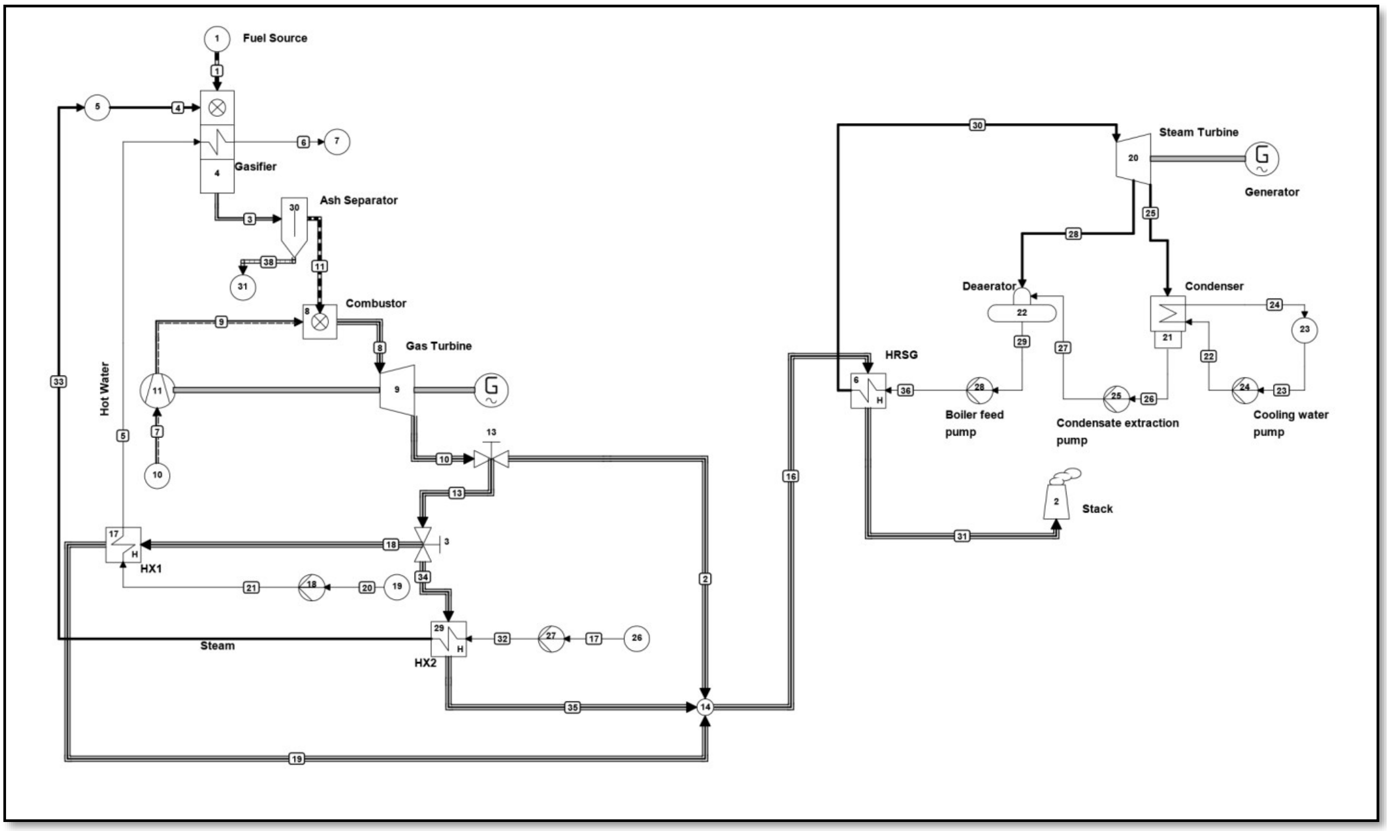

Figure 2. Layout of IGCC plant.

Therefore, the HX2 is used to heat the water for heating the bed material externally. The water flowing through pipe no 21 is heated up to 150 °C by the HX2 and leaves the HX of the gasifier at 50 °C rejecting heat to the gasifier. By harnessing the full capacity of the hot flue gas, the heat recovery steam generator (HRSG) converts the water from the feed pump into high-enthalpy steam. This steam then drives the turbine to produce electricity.

2.2. Fuel characteristics

The fuel considered for the proposed IGCC plant is Indian Coal. **Table 1** displays the heating values and composition of the Indian coal [11].

Table 1. Indian coal characteristics.

Ultimate analysis	**As dry basis (wt%)**
C	39.16
H	2.76
O	7.92
N	0.78
S	0.51
Ash	48.87
HHV (MJ/Kg)	15.83

2.3. Assumptions

In performing the chemical and thermodynamic evaluations of the gasifier and the proposed plant, the following assumptions have been applied:

Operating parameters of the gasifier:

1) Reaction pressure = 10 bar
2) Estimated pressure output = 10 bar
3) Steam-fuel ratio = 1

Gas turbine:

1) Turbine inlet pressure = 9 bar
2) Reaction temperature of combustor = 1000 ℃
3) Equivalence ratio = 1.5
4) Turbine outlet pressure = 1.01 bar

Steam turbine:

1) Turbine inlet pressure and temperature = 25 bar and 260 ℃
2) Bleed steam pressure = 3 bar
3) Condenser pressure = 25 kPa

2.4. Performance parameters

The following are the parameters that are used to calculate the results [12]:

$$\text{Energy efficiency} = \frac{\text{Net power output}}{\dot{m}_{\text{coal}} \times \text{heating value of coal}} \tag{4}$$

$$\text{Exergy efficiency } (\varepsilon) = \frac{\text{Net power output}}{\dot{m}_{\text{coal}} \times \text{coal specific exergy}} \tag{5}$$

$$\text{Cold gas efficiency} = \frac{\text{Heating value of product gas}}{\text{Heating value of feeding coal}} \tag{6}$$

3. Results and discussion

Table 2 reveals that the IGCC plant with external heat achieves an energy efficiency of 44.17% and an exergy efficiency of 40.43%, outperforming the configuration without external heat, which shows an energy efficiency of 43.17% and an exergy efficiency of 39.51%. This indicates that incorporating external heat into the gasifier improves both energy and exergy efficiencies, highlighting its beneficial impact on overall plant performance.

Table 2. Efficiencies of different plant.

Plant Type	Energy Efficiency (%)	Exergy Efficiency (%)
IGCC (With external heat)	44.17	40.43
IGCC (Without external heat)	43.17	39.51

3.1. Energy and exergy balance of IGCC plant (with external heat)

Energy losses are calculated using the ratio of heat rejected to the energy input from the fuel, while exergy losses are determined by the ratio of irreversibility to the exergy input. In the simulation, with 16,900 kw of external heat supplied to the gasifier at a reaction temperature of 650 °C, the net electrical power output reaches 120.9 MW on a lower heating value (LHV) basis. Of this, 24.89% of the total power is produced by the steam turbine. This integration of external heat not only boosts efficiency but also reduces the plant's overall water consumption.

The thermodynamic analysis shows that the IGCC plant achieves an overall energy efficiency of 44.17%. The major sources of energy loss are the condenser, which accounts for 27.43%, and the stack, contributing 26.79%. Minor losses are observed from ash at 0.88%, with the remaining 0.72% attributed to other losses by difference as shown in **Table 3**. This indicates that the condenser and stack are the primary areas where energy optimization could improve plant performance.

Table 3. Energy balance of the plant.

Components	In Percentage (%)
Energy Efficiency of plant	44.17
Losses	
Condenser	27.43
Stack	26.79
Ash	0.88
Others (By difference)	0.72

The exergy analysis of the IGCC plant shows an overall exergy efficiency of 40.43%. The combustor is identified as the largest source of exergy loss, accounting for 24.58%. Other significant losses occur in the steam generator for the gasifier (6.39%), HRSG (4.64%), gasifier (4.45%), and the stack (4.33%). Additional losses are observed in components such as the ash separator (3.78%), condenser (2.25%), gas turbine (1.34%), and steam turbine (0.91%), as shown in **Table 4**. The remaining 6.90% of losses are attributed to other factors by difference, highlighting the combustor as the primary area for potential efficiency improvement.

Table 4. Exergy balance of the plant.

Components	**In Percentage (%)**
Exergy Efficiency of plant	40.43
Losses	
Combustor	24.58
Steam generator for gasifier	6.39
HRSG	4.64
Gasifier	4.45
Stack	4.33
Ash Separator	3.78
Condenser	2.25
Gas Turbine	1.34
Steam Turbine	0.91
Others (by difference)	6.90

3.2. Parametric analysis of the plant

The parametric analysis in the study investigates the impact of external heat on various performance parameters of the IGCC plant. It reveals that increasing external heat supplied to the gasifier enhances the lower heating value (LHV) of syngas, improves the hydrogen-to-methane (H_2/CH_4) ratio, and boosts overall plant efficiency. The higher external heat input favors the endothermic steam-methane reforming reaction, resulting in a syngas with a higher hydrogen content and reduced methane. Additionally, the cold gas efficiency of the plant increases by 3.01% when 16,900 kw of heat is supplied to the gasifier, demonstrating the positive influence of external heat on the thermodynamic performance of the plant. This analysis highlights the critical role of external heat in optimizing syngas composition and improving overall plant efficiency.

3.2.1. Effect of external heat on LHV of syngas

Figure 3 shows how the lower heating value (LHV) of syngas increases as the external heat supplied to the gasifier rises. As more heat is added, the gasification process becomes more efficient, resulting in a higher energy content in the syngas produced. The graph demonstrates a clear positive relationship between the heat supplied and the LHV, highlighting the benefits of external heat in enhancing syngas quality.

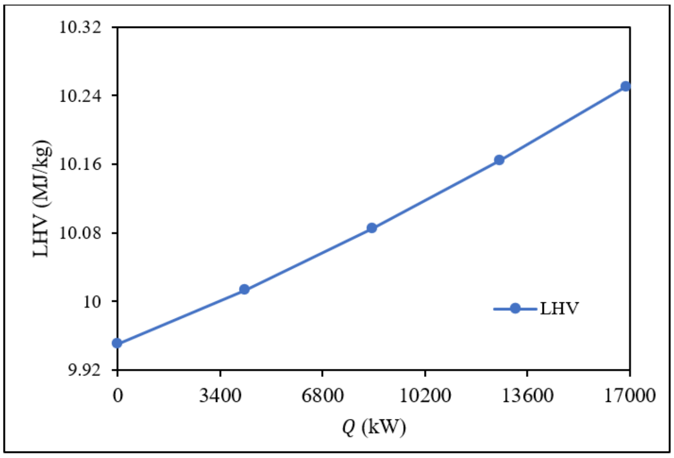

Figure 3. Effect of external heat on LHV of syngas.

3.2.2. Effect of external heat on H_2/CH_4 ratio

Figure 4 illustrates the effect of external heat on the hydrogen to methane (H_2/CH_4) ratio in the syngas. As the external heat input increases, the H_2/CH_4 ratio also rises. This is due to the steam-methane reforming reaction, which is endothermic and benefits from the additional heat. As a result, more hydrogen is produced, and the methane content decreases, improving the syngas composition for energy generation.

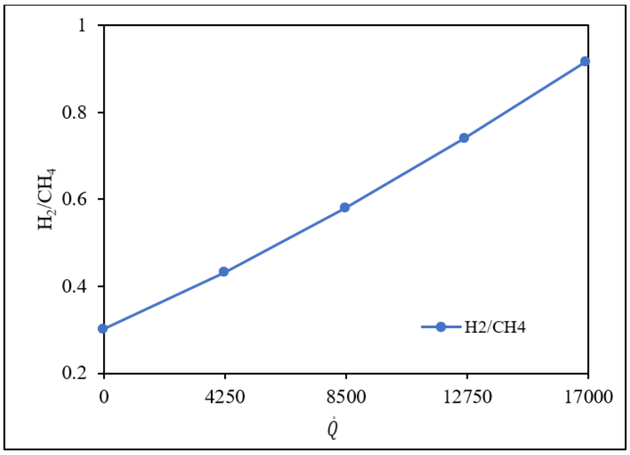

Figure 4. Effect of external heat on H_2/CH_4 ratio.

3.2.3. Effect of external heat on efficiency of the plant

Figure 5 presents the increase in plant efficiency (η) as external heat supplied to the gasifier is raised. The graph shows that, as the heat input increases, the net efficiency of the IGCC plant improves. This is because the enhanced syngas composition, particularly with higher hydrogen content, boosts the overall performance of the power generation cycle, leading to a higher net efficiency. The figure emphasizes the role of external heat in maximizing plant efficiency.

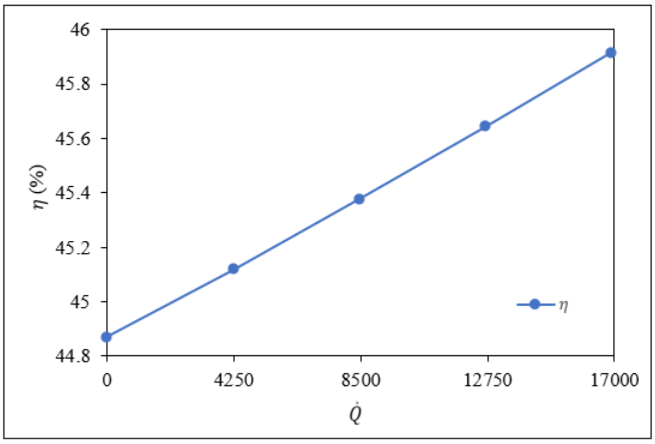

Figure 5. Effect of external heat on plant efficiency.

3.3. Validation of gasifier

To validate the proposed model, the results of two equilibrium gasification models from two different literatures are compared. The literature models are simulated in Aspen Plus software and Cycle-Tempo software, respectively [13,14]. In both, the literature shows that gasification of sawdust has been done with 10% moisture at a temperature of 800 °C. A simulation using the suggested model with the same gasification condition using sawdust as fuel was run for this comparison. **Figure 6** shows the comparison of syngas composition between the proposed model and literature data. The syngas composition of the developed gasifier model closely resembles the syngas composition of literature. Molar fraction of methane is not considered here as the value comes out to only 0.02%, which is the same as the above-mentioned literature.

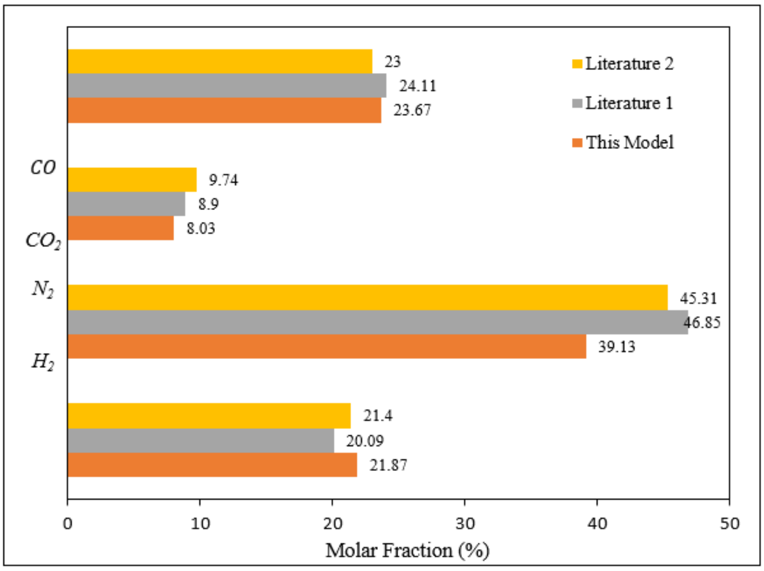

Figure 6. Comparison of syngas composition with literature data.

4. Conclusions

This study provides a comprehensive thermodynamic evaluation of an IGCC power plant using allothermal gasification. The findings demonstrate that applying external heat to the gasification process significantly enhances the syngas quality and overall plant performance. Specifically, utilizing steam as a gasifying agent and incorporating external heat increased the lower heating value (LHV) of the syngas and improved the hydrogen-to-methane (H_2/CH_4) ratio, which contributed to greater energy conversion efficiency. The energy and exergy efficiencies of the IGCC plant with external heat were measured at 44.17% and 40.43%, respectively, which represents an improvement over configurations without external heat. These gains underscore the thermodynamic benefits of integrating external heat into the gasification process. However, energy losses in the system were primarily observed in the condenser and stack, accounting for 27.43% and 26.79% of total losses, respectively. Exergy losses were most significant in the combustor, contributing to 24.58% of the total irreversibility. These areas present opportunities for optimization to further enhance the plant's efficiency. Parametric analysis further demonstrated that increasing the external heat supplied to the gasifier boosts syngas quality and plant efficiency by favoring endothermic reactions like steam-methane reforming, which increase hydrogen production.

In conclusion, the integration of external heat in allothermal gasification offers a promising pathway to improve both the energy and exergy efficiency of IGCC power plants. The reduction in water consumption and enhanced syngas composition provides additional environmental and operational benefits, making it a viable approach for optimizing future coal-based energy systems.

Author contributions: Conceptualization, SG; methodology, NKC; software, NKC and SG; validation, NKC; data curation, SK; writing—original draft preparation, NKC; writing—review and editing SK. All authors have read and agreed to the published version of the manuscript.

Conflict of interest: The authors declare no conflict of interest.

Abbreviations

HX	Heat Exchanger
h	Specific Enthalpy (kJ/kg)
Ψ	Exergy (kJ/kg)
I	Irreversibility (kW)
P	Pressure (bar)
N_2	Nitrogen
S	Sulfur
C	Carbon
H_2O	Water
O_2	Oxygen
HHV	Higher Heating Value (MJ/kg)
$\dot{m}_w$	Mass Flow Rate of Water (kg/s)
$\dot{Q}$	External Heat Flow Rate (kW)

References

1. Executive summary power sector. Available online: https://cea.nic.in/wp-content/uploads/executive/2024/07/Executive_Summary_June_2024.pdf (accessed on 8 August 2024).
2. Promes EJO, Woudstra T, Schoenmakers L, et al. Thermodynamic evaluation and experimental validation of 253 MW Integrated Coal Gasification Combined Cycle power plant in Buggenum, Netherlands. Applied Energy. 2015; 155: 181-194. doi: 10.1016/j.apenergy.2015.05.006
3. Bhaskar T, Balagurumurthy B, Singh R, et al. Thermochemical Route for Biohydrogen Production. Biohydrogen. 2013; 285-316. doi: 10.1016/b978-0-444-59555-3.00012-x
4. Gokon N, Izawa T, Abe T, et al. Steam gasification of coal cokes in an internally circulating fluidized bed of thermal storage material for solar thermochemical processes. International Journal of Hydrogen Energy. 2014; 39(21): 11082-11093. doi: 10.1016/j.ijhydene.2014.05.124
5. Cheng G, Li Q, Qi F, et al. Allothermal gasification of biomass using micron size biomass as external heat source. Bioresource Technology. 2012; 107: 471-475. doi: 10.1016/j.biortech.2011.12.074
6. Karellas S, Panopoulos KD, Panousis G, et al. An evaluation of Substitute natural gas production from different coal gasification processes based on modeling. Energy. 2012; 45(1): 183-194. doi: 10.1016/j.energy.2012.03.075
7. Santhanam S, Schilt C, Turker B, et al. Thermodynamic modeling and evaluation of high efficiency heat pipe integrated biomass Gasifier–Solid Oxide Fuel Cells–Gas Turbine systems. Energy. 2016; 109: 751-764. doi: 10.1016/j.energy.2016.04.117
8. Cycle-Tempo release 5.1.7, Delft University of Technology. Available online: https://asimptote.com/cycle-tempo/ (accessed on 10 June 2024).
9. Ozer M, Basha OM, Stiegel G, et al. Effect of coal nature on the gasification process. Integrated Gasification Combined Cycle (IGCC) Technologies. 2017; 257-304. doi: 10.1016/b978-0-08-100167-7.00007-x
10. Suárez-Almeida M, Gómez-Barea A, Ghoniem AF, et al. Solar gasification of biomass in a dual fluidized bed. Chemical Engineering Journal. 2021; 406: 126665. doi: 10.1016/j.cej.2020.126665
11. Choudhary NK, Khankari G, Karmakar S. Waste heat utilization using organic rankine cycle from a pressurized pulverized combined cycle power plant. Proceedings of the Institution of Mechanical Engineers, Part A: Journal of Power and Energy. 2024; 238(5): 922-933. doi: 10.1177/09576509241240013
12. Choudhary NK, Deep AP, Karmakar S. Thermodynamic Analysis of Integrated Gasification Combined Cycle Integrated with Organic Rankine Cycle for Waste Heat Utilization. Waste and Biomass Valorization. 2024; 15(6): 3691-3709. doi: 10.1007/s12649-023-02391-2
13. Okati A, Khani MR, Shokri B, et al. On the operating parameters for hydrogen-rich syngas production in a plasma co-gasification process of municipal solid wastes and polypropylene using a constrained model in Aspen plus. Journal of the Energy Institute. 2023; 107: 101173. doi: 10.1016/j.joei.2023.101173
14. Altafini CR, Wander PR, Barreto RM. Prediction of the working parameters of a wood waste gasifier through an equilibrium model. Energy conversion and management. 2003; 44(17): 2763-2777. doi: 10.1016/S0196-8904(03)00025-6

Thermal Science and Engineering 2024, 7(3), 9102.
https://doi.org/10.24294/tse.v7i3.9102

Article

Enhancement of heat dissipation efficiency in the CSNS target through the innovative design of a serial cooling water channel

Jiahui Chen[1,2,3], Jianfei Tong[2,3,*], Youlian Lu[2,3], Songlin Wang[2,3], Tianjiao Liang[2,3], Jian Wen[1]

[1] School of Energy and Power Engineering, Xi'an Jiaotong University, Xi'an 710049, China
[2] Institute of High Energy Physics, Chinese Academy of Sciences (CAS), Beijing 100049, China
[3] Spallation Neutron Source Center, Dongguan 523803, China
*** Corresponding author:** Jianfei Tong, tongjf@ihep.ac.cn

CITATION

Chen J, Tong J, Lu Y, et al. Enhancement of heat dissipation efficiency in the CSNS target through the innovative design of a serial cooling water channel. Thermal Science and Engineering. 2024; 7(3): 9102.
https://doi.org/10.24294/tse.v7i3.9102

ARTICLE INFO

Received: 12 September 2024
Accepted: 25 September 2024
Available online: 30 September 2024

COPYRIGHT

Copyright © 2024 by author(s). *Thermal Science and Engineering* is published by EnPress Publisher, LLC. This work is licensed under the Creative Commons Attribution (CC BY) license.
https://creativecommons.org/licenses/by/4.0/

Abstract: This paper presents a coupling of the Monte Carlo method with computational fluid dynamics (CFD) to analyze the flow channel design of an irradiated target through numerical simulations. A novel series flow channel configuration is proposed, which effectively facilitates the removal of heat generated by high-power irradiation from the target without necessitating an increase in the cooling water flow rate. The research assesses the performance of both parallel and serial cooling channels within the target, revealing that, when subjected to equivalent cooling water flow rates, the maximum temperature observed in the target employing the serial channel configuration is lower. This reduction in temperature is ascribed to the accelerated flow of cooling water within the serial channel, which subsequently elevates both the Reynolds number and the Nusselt number, leading to enhanced heat transfer efficiency. Furthermore, the maximum temperature is observed to occur further downstream, thereby circumventing areas of peak heat generation. This phenomenon arises because the cooling water traverses the target plates with the highest internal heat generation at a lower temperature when the flow channels are arranged in series, optimizing the cooling effect on these targets. However, it is crucial to note that the pressure loss associated with the serial structure is two orders of magnitude greater than that of the parallel structure, necessitating increased pump power and imposing stricter requirements on the target container and cooling water pipeline. These findings can serve as a reference for the design of the cooling channels in the target station system, particularly in light of the anticipated increase in beam power during the second phase of the China Spallation Neutron Source (CSNS II).

Keywords: CSNS target; heat dissipation; Monte Carlo method; serial flow; CFD; pump power

1. Introduction

As a kind of multidisciplinary platform for scientific research, spallation neutron sources have garnered increasing attention in recent years. Its applications span various fields, including basic-energy sciences, nuclear science, and the utilization of white neutrons/fast neutrons, as well as proton beam applications and meson research [1,2]. The neutron flux produced by a spallation neutron source serves as a critical metric for evaluating its operational efficiency; however, achieving a higher neutron flux necessitates an increase in beam power, which consequently results in elevated heat generation at the target station [3]. Thus, the development of effective heat removal strategies is of paramount importance for enhancing the power capabilities of spallation neutron sources.

A variety of heat removal techniques have been reported to be implemented in spallation neutron source targets globally. Spallation Neutron Source (SNS) in the United States and the Japan Proton Accelerator Research Complex (J-PARC) Pulsed Spallation Neutron Source (JSNS) are both megawatt-class neutron sources that utilize liquid mercury as coolant within the target [4,5]. The target of the Swiss Spallation Neutron Source (SINQ) in Switzerland employs an array of target rods that contain a sealed liquid lead-bismuth alloy [6]. The European Spallation Neutron Source (ESS), currently under construction, is also designed as a megawatt-level neutron source, featuring a large wheel-shaped target vessel [7]. The target configuration in Target Station 1 (TS-1) of Neutron and Muon Source at the Rutherford Appleton Laboratory in the United Kingdom consists of a fragmented target with integrated parallel cooling channels [8]. Analogous to ISIS TS-1 target, the target employed in the China Spallation Neutron Source (CSNS) in also characterized as a segmented target with parallel cooling channel [9]. This configuration is specifically developed to enhance cooling through a parallel flow system, which comprises a single inlet and a single outlet.

Among the aforementioned targets, the interaction of proton pulses with the liquid mercury target will generate pressure wave phenomena, which may result in a deleterious effect known as cavitation damage erosion [10]. Additionally, the polonium isotopes that are difficult to handle will occur in the Pb-Bi eutectic target as a consequence of irradiation, and the sealing of the target rod is also challenging [7,11]. Furthermore, rotating targets present issues related to duty cycles, and the target material is subjected to significant thermal cycling, potentially leading to embrittlement of the material [7]. Consequently, a mature design with solid fixed targets remains the preferred option for CSNS targets.

The utilization of parallel channels is prevalent in the majority of current solid fixed targets designed for heat dissipation. Research conducted by Hao Junhong et al. [12,13] focused on the thermal management of spallation neutron source targets, while Lu [14] examined the impact of proton beam deviation on the heat dissipation efficacy of the spallation neutron source target. Additionally, Allen and Findlay et al. investigated the decay heat with the target at the ISIS TS-1 facility. Takenaka [15] analyzed the parallel flow channels in megawatt-level sliced targets and target rod arrays, concluding that the minimum thickness of the target slice should be less than 9 mm. Bauer [16] similarly asserted that in spallation neutron sources operating at elevated proton beam power, the minimum gap size between targets may need to be reduced to below 0.7 mm. Furthermore, in addressing multi-channel cooling challenges, the effective delivery and distribution of coolant are critical for optimizing cooling performance [17]. Kumar and Singh [18] emphasized that the configuration of flow and the actual distribution of coolant must align with the heat flow to enhance better heat dissipation efficiency. If the thickness of the target plates and the inter-plate gaps are excessively small, the number of parallel channels will increase and make it difficult for the distribution of the coolant. Additionally, overly diminutive dimensions may pose significant challenges in terms of processing and installation.

Currently, research on the parallel channels of solid fixed targets is relatively comprehensive, whereas investigations into the heat dissipation mechanism of serial channels within the targets remain limited. Consequently, this paper introduces a novel serial flow channel designed for application in irradiated targets, informed by an analysis of the heat dissipation phenomena observed in complex flow channels at the CSNS. In the design of the serial flow channel, it is demonstrated that the dimensions of the target plates and flow channels do not significantly influence the distribution of the coolant. The cooling water can be effectively concentrated in regions exhibiting higher thermal power, thereby ensuring adequate cooling in those areas. This study examines the differences in heat dissipation between serial and parallel structures, evaluates the respective advantages and disadvantages of each configuration, and offers critical insights and recommendations for the enhancement of CSNS II.

2. CSNS target and simulation model

The structure of the current target utilized in CSNS is illustrated in **Figure 1**. The primary component consists of fifteen tantalum-clad tungsten target plates, which are installed within a stainless steel vessel. The design incorporates gaps ranging from 0.8 to 1.2 mm between the target plates to facilitate effective heat dissipation. Additionally, two stainless steel ribs are positioned among the target plates to provide structural reinforcement. Cooling water is introduced into the target vessel from one side, subsequently circulating the parallel channels formed between the target plates before exiting the vessel. Thermocouples are strategically installed in select plates to monitor the temperature of the target.

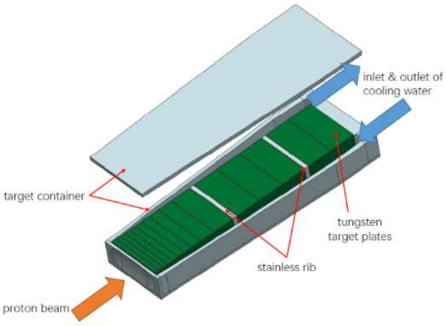

Figure 1. The structure of the CSNS target.

In the operational context, the target is bombarded by high-power proton beams, resulting in thermal energy deposition approximately equivalent to half of the beams' power within the target. Utilizing the Monte Carlo method, the energy deposited in the target is attributed to three primary mechanisms. The first mechanism is the energy loss associated with the ionization of electrons in atomic structures by protons and secondary charged particles, referred to as ionization energy loss. The second mechanism involves the recoil energy generated when fragments with elevated excitation energy release particles. The third mechanism pertains to the energy released during the fission of residual nuclei. This study integrates the Monte Carlo method with computational fluid dynamics (CFD). The heat deposition generated by proton interactions with the heavy metal target is calculated using Monte Carlo N-Particle Transport Code (MCNP), and this heat deposition is subsequently incorporated into FLUENT software as an internal heat source for thermal analysis. The distribution of generated heat within the target is non-uniform, as illustrated in

Figure 2. This figure depicts the model employed in MCNP and the spatial distribution of the internal heat source within the target when the proton beam power is set as 100 KW. It is evident that the majority of the heating power is concentrated in the target plates located at the front of the vessel.

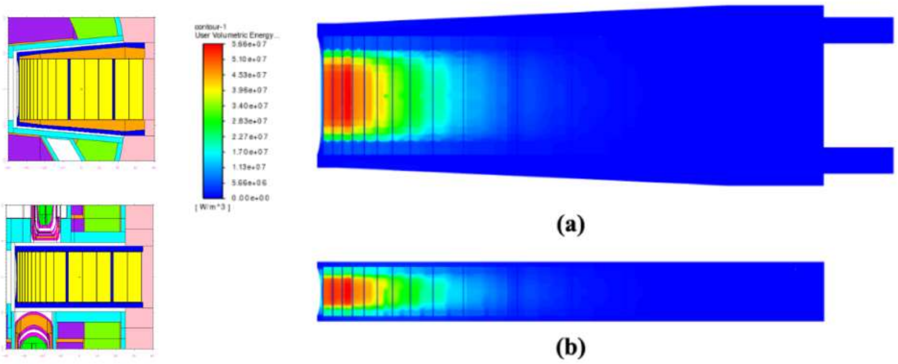

Figure 2. Model employed in MCNP and heat source power contour. **(a)** horizontal section; **(b)** vertical section. (protons delivered from left to right).

In order to maintain the maximum temperature of each target plate stay within the designated design parameters, the current target is cooled using water that circulates through the gaps between the target plates. This system allows for adjustments in both velocity and flow rate within each gap, a configuration referred to as a parallel channel. In this arrangement, the allocation of cooling water to regions with high heating power is critical in determining the overall efficiency of the target. Conversely, in a serial channel configuration, the channels are arranged sequentially, allowing for a concentration of cooling water in the areas of the target that experience higher power output.

In engineering practice, modifications to the target plates and channels can significantly impact the efficiency of heat dissipation in the target. Consequently, this paper presents a simplified structure of the target to mitigate the effects of such optimizations. **Figure 3** illustrates two channel models utilized in this study, where the gray region represents the target plate and the blue region denotes the cooling channel. Given that the majority of internal heating power is concentrated at the front of the vessel, there is an increased requirement for cooling in the target plates located in this region. As a result, the target plates are designed to be thicker in the direction of the proton beam. A detailed description of the channels is provided in **Figure 4**.

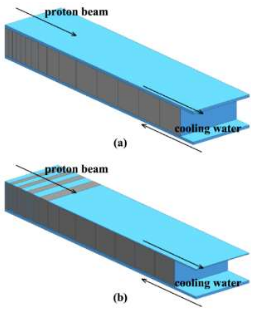

Figure 3. Model for simulation. **(a)** parallel channel configuration; **(b)** serial channel configuration.

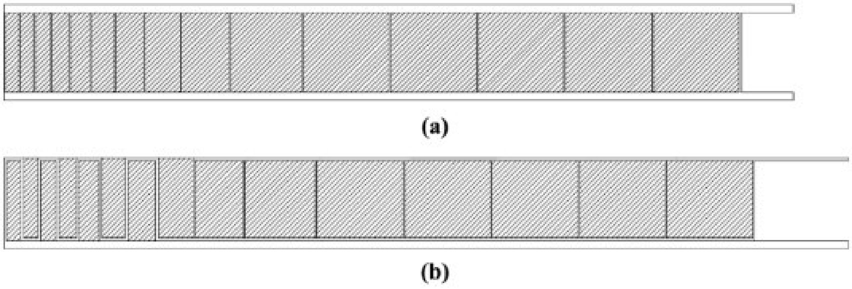

Figure 4. Cross section of the flow channel. **(a)** parallel channel configuration; **(b)**serial channel configuration.

In the parallel channel model, cooling water is introduced from one side of the target and exits from the opposite side after traversing through parallel channels. Conversely, the serial channel is implemented at the front 7 target plates, while the parallel configuration is maintained for the rear 8 target plates due to the reduced internal heat generation. The dimensions of the target plates and channels are presented in **Table 1**, which corresponds to the actual specifications. The inlet temperature of the cooling water is set at 28 ℃.

Table 1. The dimensions of the target plates and channels.

No. of target plate	Target plate thickness (mm)	No. of channel	Width of parallel channel (mm)	Width of serial channel (mm)
1	12.6	0	1	2.5
2	12.6	1	1	2.5
3	13.6	2	1	2.5
4	15.6	3	1	2.5
5	17.6	4	1	2.5
6	20.6	5	1	2.5
7	24.6	6	1	2.5
8	31.6	7	1	2.5
9	42.6	8	1	1
10	63.6	9	1	1
11	76.6	10	1	1
12	76.6	11	1	1
13	76.6	12	1	1
14	76.6	13	1	1
15	76.6	14	1	1
\		15	1	1

3. Results

Based on the actual process parameters, 8 cases have been studied in this paper for both models. The specifics of these cases are presented in **Table 2**, which serves solely for illustrative purposes. Detailed parameters will be attached with the analysis subsequently.

Table 2. List of cases.

Parallel channel model		**Cooling water flow rate (kg/s)**		
		2.3	2.5	2.7
Proton beam power (kW)	50	\	A3	\
	100	A1	A4	A2
	200	\	A5	\
	500	\	A6	\
	800	\	A7	\
	1000	\	A8	\
Serial channel model		**Cooling water flow rate (kg/s)**		
		2.3	2.5	2.7
Proton beam power (kW)	50	\	B3	\
	100	B1	B4	B2
	200	\	B5	\
	500	\	B6	\
	800	\	B7	\
	1000	\	B8	\

The subsequent analysis presents a comparison of temperature profiles between serial and parallel models. **Figure 5** illustrates the centerline temperature variations at a constant cooling water flow rate of 2.5 kg/s. The target plates, designated as 1 through 15, were aligned with the direction of the proton beam. It is evident that the temperature of target plates 1–10 in the serial model is lower than those observed in the parallel model. Conversely, the temperature of target plates 11–15 in the parallel model is comparatively lower. Furthermore, across all three scenarios examined, the peak temperature in the serial model occurs at target plate 9, whereas in the parallel model, it is observed at target plate 6. A comparison of the maximum target temperatures between the two models reveals that the maximum temperature in the parallel model consistently exceeds that of the serial model. When the proton beam power is increased to 1 megawatt (MW), the maximum temperature of the target in the parallel configuration is approximately 100 K higher than that in the serial configuration.

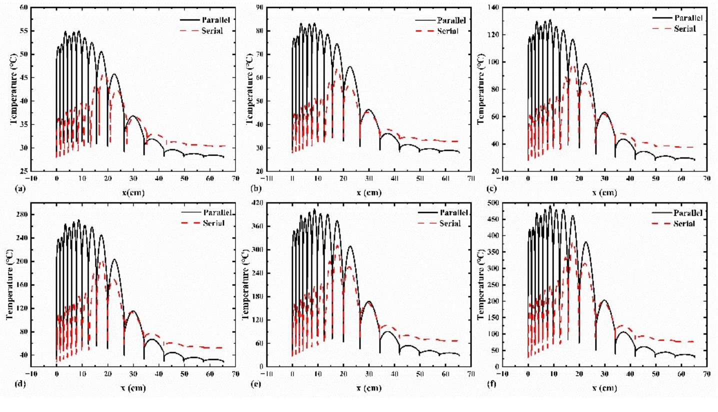

Figure 5. Profiles of the temperature along the centerline for different configurations under. **(a)** 50KW; **(b)** 100KW; **(c)** 200KW; **(d)** 500KW; **(e)** 800KW; **(f)** 1000KW.

Figure 6 presents a comparative analysis of the temperature distribution within the two distinct configurations. The legend for the temperature contours remains consistence across both configurations when subjected to the same proton beam power. Notably, the temperatures of the first 8 target plates in the serial configuration are significantly lower than those observed in the parallel model. This observation suggests that, for the initial 8 target plates with elevated internal heat generation, the heat produced can be dissipated more effectively through serial flow configurations. Conversely, for the subsequent 7 target plates, the temperature remains within the designated design parameters, attributable to the reduction in internal heat generation, despite a lower heat dissipation efficiency.

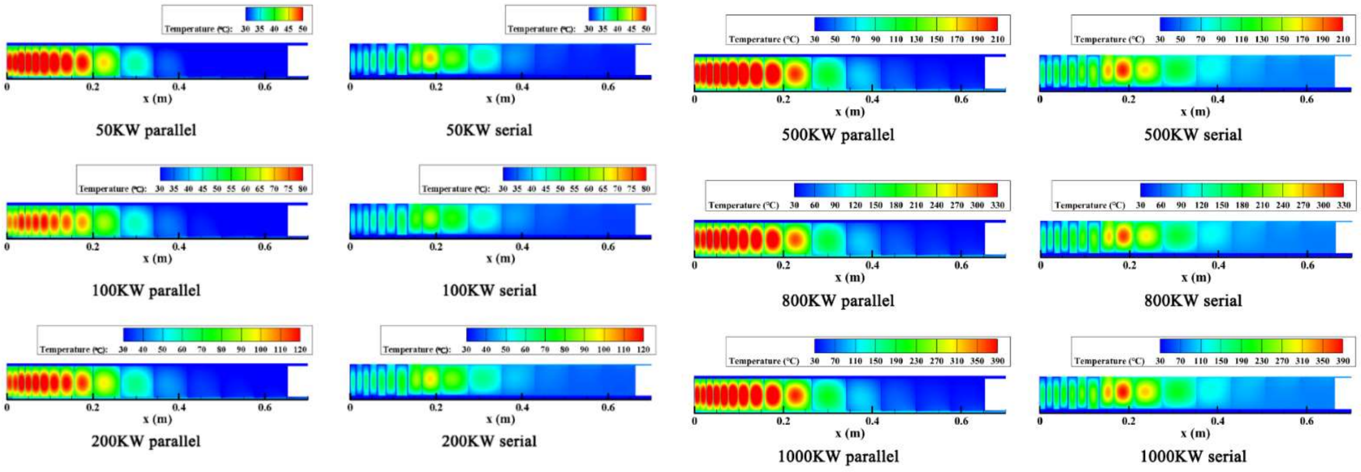

(a) **(b)**

Figure 6. Temperature contours for parallel/serial configurations under different proton beam powers. **(a)** 50/100/200 KW; **(b)** 500/800/1000 KW.

Due to the significant temperature disparity observed between scenarios involving power levels exceeding 500 KW and those with lower power outputs, the subsequent analysis and discussions will be focused on power levels of 50 KW, 100 KW, and 200 KW to facilitate a more coherent examination.

Figure 7 illustrates the temperature profiles along the centerline of the model under varying proton beam power, with the cooling water flow rate maintained at 2.5 kg/s. Each line in the figure contains 15 peak values, which correspond to the maximum temperature recorded for each target plate. As depicted in **Figure 7(a)**, target plate 6 exhibits the highest temperature within the parallel model, with maximum temperatures of 55 °C, 81 °C and 131 °C observed at proton beam powers of 50 KW, 100 KW, and 200 KW, respectively. This phenomenon can be attributed to the concentration of heating power in the target plates located at the front of the vessel, resulting in a temperature decline along the x-axis beyond plate 6. Conversely, **Figure 7(b)** indicates that in the serial configuration, the highest temperature is recorded on plate 9, with maximum temperatures of 46 °C, 64 °C and 99 °C at the same proton beam powers. This suggests that the serial channel effectively enhances heat dissipation for the initial target plates. Furthermore, **Figure 8** presents the temperature profiles along the centerline under a fixed proton beam power of 100 KW. The data indicate that variations in the cooling water flow rate do not significantly alter the trend of temperature change along the x-axis. Additionally, a 10% change in the cooling water flow rate has a minimal impact on the target temperature.

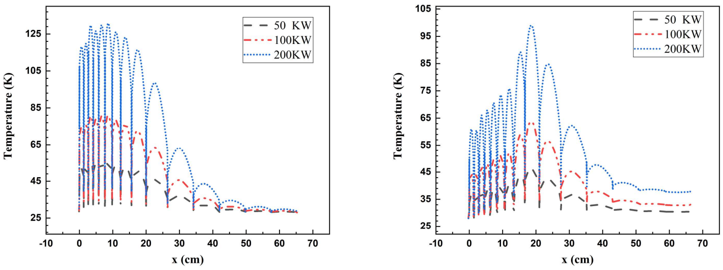

(a) (b)

Figure 7. Profiles of temperature along the centerline for different proton beam power under cooling water flow rate of 2.5 kg/s. **(a)** parallel channel model; **(b)**serial channel model.

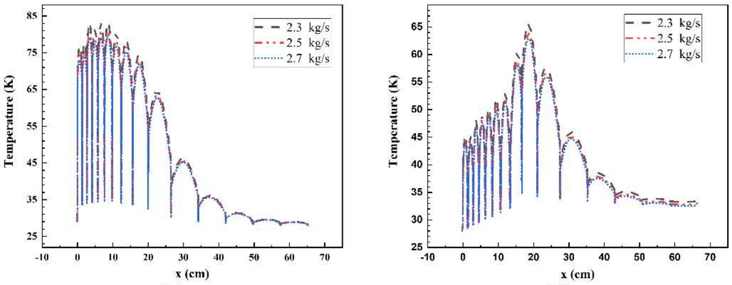

(a) (b)

Figure 8. Profiles of the temperature along the centerline for different cooling water flow rates under the proton beam power of 100KW. **(a)** parallel configuration; **(b)** serial configuration.

4. Effect of structure on Nusselt Number

The dimensions of the channel and the flow rate within a serial model differ from those in a parallel model, even when subjected to identical cooling water flow rates and proton beam power. This inconsistency complicates the analytical process; therefore, the Nusselt Number (*Nu*) functions as a standardized metric that aids in this analysis.

$$Nu = \frac{hl}{\lambda} \tag{1}$$

where h is the convective heat transfer coefficient and l is the characteristic length defined as the width of the flow channel. λ is the thermal conductivity of the cooling water, which is evaluated at the average temperature within the flow channel. The initial channel positioned in the direction of the proton beam is designated as channel 0. **Figure 9** illustrates the *Nu* for each channel under varying proton beam power conditions. **Figure 9(a)** presents the *Nu* values for the parallel model, revealing that as the channel number increases, the *Nu* initially rises gradually before experiencing a rapid decline. Notably, the *Nu* values in the front channels are greater than those in the rear channels, indicating that the heat exchange efficiency is enhanced in the front channels due to a more significant temperature differential between the cooling water and the channel walls. **Figure 9(b)** depicts the *Nu* values for the serial model. Unlike the parallel model, the peak value of *Nu* is observed within the channel 3–5, aligning with the target plates 3–6, which possess the highest internal heat source. Channels 9–15 are configured as parallel channels, resulting in a diminished flow rate. Concurrently, the temperature of the associated targets is expected to decrease as a result of the declining internal heat source. Consequently, *Nu* in channels 9–15 is considerably lower than that in the preceding channels. Furthermore, it is evident that the *Nu* value for the serial channel arrangement is markedly greater than that of the parallel arrangement under identical conditions, a difference that is particularly pronounced in the front channels.

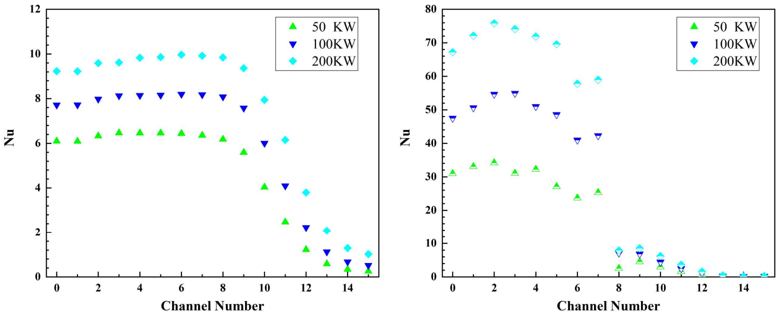

(a) **(b)**

Figure 9. *Nu* in each channel under different proton beam power. **(a)** parallel channel configuration; **(b)** serial channel configuration.

Figure 10 illustrates the velocity of the cooling water(a) and the Reynolds number(b) within the channel, corresponding to a cooling water flow rate of 2.5kg/s.

$$Re = \frac{\rho v l}{\mu} \tag{2}$$

where ρ is the density of water within the channel, v is the average velocity of water in the channel, l is the characteristic length, which corresponds to the width of the flow channel, μ is the dynamic viscosity, and the characteristic temperature is defined as the average temperature of the cooling water in the channel. As illustrated in **Figure 10**, the flow velocity and Reynolds number (Re) of the cooling water in the serially arranged channels 0–7 are significantly greater than those recorded in the parallel configuration. This observation suggests a more intense forced convective heat transfer process occurring within the initial 8 flow channels, which is further corroborated by the data presented in **Figure 9**.

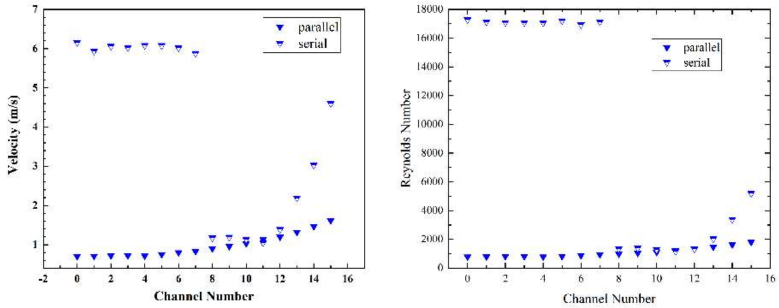

(a) (b)

Figure 10. Comparison of Velocity. **(a)** and Reynolds number; **(b)** between two configurations with a cooling water flow rate of 2.5 kg/s.

Figure 11 presents a comparative analysis of the Nusselt number (*Nu*) in both parallel model and serial configurations under varying proton beam power with a cooling water flow rate of 2.5 kg/s. It is evident that the *Nu* values for channels 0–7 in the serial model are significantly greater than those observed in the parallel model, suggesting that the serial model exhibits superior heat transfer efficiency. Conversely, in channels 8–15, the parallel model demonstrates enhanced heat transfer efficiency. Given that the majority of the heating power is concentrated in the target plates located at the front end of the vessel, the distribution of *Nu* in the serial model is more effective in mitigating the maximum temperature of the target. This implies that the surface temperature of the target can be maintained within a safe range with a reduced volume of cooling water when utilizing the serial cooling channel configuration.

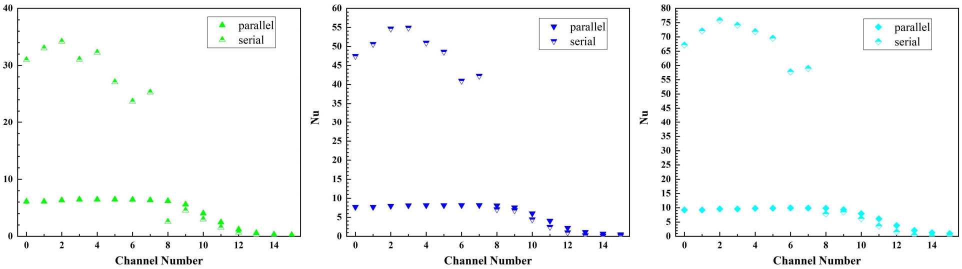

(a) (b) (c)

Figure 11. Comparison of *Nu* between two configurations with a cooling water flow rate of 2.5 kg/s. **(a)** 50KW; **(b)** 100KW; **(c)** 200KW.

In the serial model, the inlet of each channel is connected to the outlet of the preceding channel, resulting in an increase in water temperature as it progresses through each channel. This phenomenon may exacerbate the heat dissipation capabilities of the preceding channel. **Figure 12** illustrates a comparison of the average temperatures of the cooling water across various channels under differing proton beam power levels. In the parallel model, channels 0–7 exhibit similar average temperatures, with channels 3–6 displaying slightly elevated temperatures compared to the others. Conversely, the average temperatures in channels 8–15 are significantly lower. This discrepancy can be attributed to the independent flow characteristics of each channel in the parallel model, where the flow rates are relatively uniform (as shown in **Figure 10**). Therefore, the average temperature within each channel is influenced primarily by the internal heat sources of the target plates, leading to a temperature evolution that mirrors that of the target plates. In contrast, the average temperatures of channels 0–7 in the serial model demonstrate a linear increase. This trend arises from the direct connection between the inlet of each channel and the outlet of the preceding channel, resulting in a rise in the cooling water temperature as it flows through. Channels 8–15, being part of the parallel configuration, also exhibit temperature variations that correlate with the internal heat source power of the target plates. Given that the inlets of channels 8–15 effectively function as the outlets of channel 7, the minimum average temperature in these channels is inherently higher than that of channel 7. Obviously, the parallel flow configuration distributes the cooling capacity of the water by adjusting the flow to each channel, while the serial flow concentrates the cooling capacity at the front of the target. Since the heating power of the target is predominantly concentrated in the front target plates, this characteristic of the serial configuration is particularly advantageous for reducing the temperature of the target at the front of the vessel.

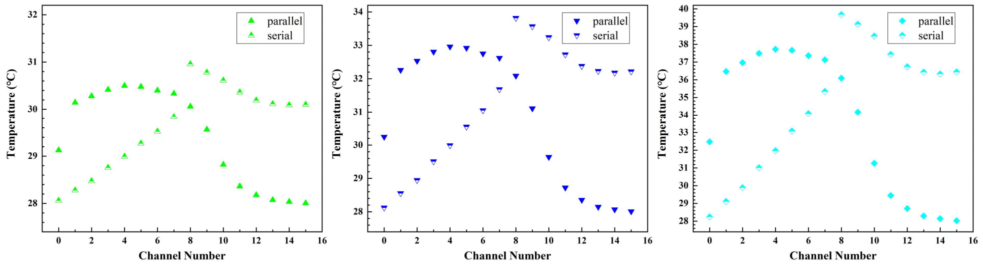

(a) (b) (c)

Figure 12. Comparison of the temperature measurements across each channel between two distinct configurations with a cooling water flow rate of 2.5 kg/s. **(a)** 50KW; **(b)** 100KW; **(c)** 200KW.

5. Effect of channel on pressure loss

The pressure loss within the channel and the power required by the pump serve as critical indicators of channel design. **Figure 13** illustrates the impact of cooling water flow rate on pressure loss (a) and pump power (b) across various models, specifically under conditions where the proton beam power is set at 100 KW. It is evident that, for a given cooling water flow rate, the pressure loss in a serial channel consistently exceeds a parallel channel. This phenomenon can be attributed to the parallel configuration, which distributes the cooling water flow across multiple channels, resulting in a larger cross-sectional area for the cooling water pathway. Consequently, the increase in pressure loss necessitates a significant rise in pump power.

$$P_{Pump} = \Delta PQ \tag{3}$$

where ΔP is the pressure loss within the target vessel, and Q is the flow rate of the cooling water. The relationship established by the formula indicates that pump power is directly proportional to pressure loss, a correlation that is substantiated by the data presented in **Figure 13(b)**. Furthermore, it is evident that in the serial configuration, both pressure loss and pump power exhibit a more pronounced increase with rising cooling water flow rates compared to the parallel configuration. **Figure 14** illustrates the effect of cooling water flow rate on the maximum temperature of the target across different configurations, specifically under conditions where the proton beam power is set as 100 KW. Consistent with the trends observed in pressure loss, the maximum temperature of the target in the serial model decreases more significantly with an equivalent increase in cooling water flow rate. Therefore, it can be concluded that the serial channel is more advantageous for heat dissipation; however, it also incurs greater pressure loss and pump power requirements. At low proton beam power levels, the cooling capacity of the parallel channel configuration is sufficient. Conversely, as the proton beam power increases, the serial design becomes more effective in enhancing heat dissipation, albeit at the expense of increased pump power.

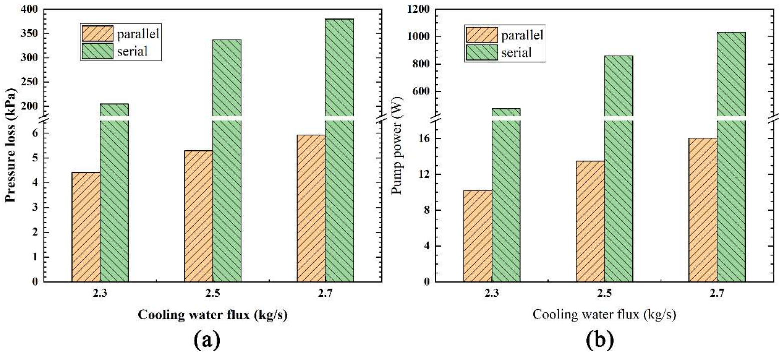

Figure 13. Influence of the cooling water flow rate on the pressure loss. **(a)** and the pump power; **(b)** in different configurations with the proton beam power of 100KW.

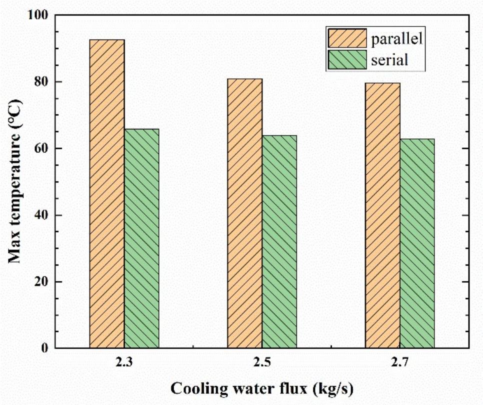

Figure 14. Influence of the cooling water flow rate on the maximum temperature of the target in different configurations with the proton beam power of 100KW.

6. Conclusion

This paper presents a numerical investigation of heat dissipation in a novel serial channel configuration within a solid fixed target, utilizing a combination of the Monte Carlo method and computational fluid dynamics (CFD). The implementation of a serial channel significantly enhances the cooling efficiency of the target, particularly under conditions where the flow of cooling water is constrained.

a) The flow rate of cooling water within the serial channel is elevated, resulting in increased Reynolds (Re) and Nusselt (Nu) numbers, which in turn enhances the heat transfer performance. Therefore, for a constant cooling water flow rate, the maximum temperature of the target equipped with the serial channel is reduced;

b) The serial design facilitates a decrease in the temperature of the cooling water as it traverses the initial target plates, thereby prioritizing the cooling of the high-power regions. This configuration results in the highest temperature point of the target being positioned further downstream, which is advantageous for managing the heat dissipation in structures characterized by uneven heat distribution, such as irradiated targets;

c) The introduction of a serial flow channel contributes to an increase in pressure within the target, necessitating greater pump power to circulate the coolant. This requirement imposes higher standards on the target container and the cooling water pipeline infrastructure.

Author contributions: Conceptualization, CJ and TJ; methodology, TJ; software, LY; validation, LY and WS; formal analysis, CJ; investigation, LY; resources, WS; data curation, LY; writing—original draft preparation, CJ; writing—review and editing, WJ; visualization, LY; supervision, LT; project administration, TJ; funding acquisition, TJ. All authors have read and agreed to the published version of the manuscript.

Funding: This research was funded by the Program for Guangdong Introducing Innovative and Entrepreneurial Teams. (Project number: 2017ZT07S225).

Conflict of interest: The authors declare no conflict of interest.

References

1. Wei J, Chen H, Chen Y, et al. China Spallation Neutron Source: Design, R&D, and outlook. Nuclear Instruments and Methods in Physics Research Section A: Accelerators, Spectrometers, Detectors and Associated Equipment. 2009; 600(1): 10-13. doi: 10.1016/j.nima.2008.11.017
2. Chen Y. China Spallation Neutron Source (CSNS). Bulletin of Chinese Academy of Sciences. 2011; 26(6): 726-728.
3. Wang F, Liang T, Yin W, et al. Conceptual design of target station and neutron scattering spectrometers for the Chinese spallation neutron source. Nuclear techniques. 2005; 8: 593-597. doi: 10.3321/j.issn:0253-3219.2005.08.006
4. Haines JR, McManamy TJ, Gabriel TA, et al. Spallation neutron source target station design, development, and commissioning. Nuclear Instruments and Methods in Physics Research Section A: Accelerators, Spectrometers, Detectors and Associated Equipment. 2014; 764: 94-115. doi: 10.1016/j.nima.2014.03.068
5. Ikeda Y. Scientific Reviews: 1-MW Pulse Sapllation Neutron Source (JSNS) of J-PARC. Neutron News. 2005; 16(1): 20-24. doi: 10.1080/10448630500454189
6. Bauer GS, Salvatores M, Heusener G. MEGAPIE, a 1 MW pilot experiment for a liquid metal spallation target. Journal of Nuclear Materials. 2001; 296(1): 17-33. doi: 10.1016/S0022-3115(01)00561-X
7. Aguilar A, Sordo F, Mora T, et al. Design specification for the European Spallation Source neutron generating target element. Nuclear Instruments and Methods in Physics Research Section A: Accelerators, Spectrometers, Detectors and Associated Equipment. 2017; 856: 99-108. doi: 10.1016/j.nima.2017.03.003
8. Burns GJ, Dey A, Findlay DJS, et al. Erosion of neutron-producing targets at ISIS spallation neutron source. Nuclear Instruments and Methods in Physics Research Section B: Beam Interactions with Materials and Atoms. 2022; 521: 7-16. doi: 10.1016/j.nimb.2022.04.004
9. Wei S, Zhang R, Shi Y, et al. Development of CSNS Target. Atomic Energy Science and Technology. 2019; 53(12): 2441-2446. doi: 10.7538/yzk.2018.youxian.0885
10. Futakawa M, Kogawa H, Hino R, et al. Erosion damage on solid boundaries in contact with liquid metals by impulsive pressure injection. International Journal of Impact Engineering. 2003; 28(2): 123-135. doi: 10.1016/S0734-743X(02)00054-4
11. Park JJ, Butt DP, Beard CA. Review of liquid metal corrosion issues for potential containment materials for liquid lead and lead-bismuth eutectic spallation targets as a neutron source. Nuclear Engineering and Design. 2000; 196(3): 315-325. doi: 10.1016/S0029-5493(99)00303-9
12. Hao J, Chen Q, Lu Y, et al. Thermal Design of a Spallation Neutron Source Target System. Journal of Engineering Thermophysics. 2013; 34: 1515-1518.
13. Hao J, Chen Q, Xu Y, et al. Flow field optimization and design for a Spallation Neutron Source target cooling system. Science China Technological Sciences. 2013; 56(6): 1370-1376. doi: 10.1007/s11431-013-5215-4
14. Lu Y, Tong J, Wang S, et al. The influence of proton beam offset on CSNS target heat transfer performance. In: Proceedings for the 14th National Conference on Reactor Thermalhydraulics; 23 September 2015; Beijing, China.
15. Takenaka N, Nio D, Kiyanagi Y, et al. Thermal hydraulic design and decay heat removal of a solid target for a spallation neutron source. Journal of Nuclear Materials. 2005; 343(1-3): 169-177. doi: 10.1016/j.jnucmat.2004.11.017
16. Bauer GS. Overview on spallation target design concepts and related materials issues. Journal of Nuclear Materials. 2010; 398(1-3): 19-27. doi: 10.1016/j.jnucmat.2009.10.005

17. Li Y, Roux S, Castelain C, et al. Tailoring the fluid flow distribution in a parallel mini-channel heat sink under multiple-peak heat flux. Thermal Science and Engineering Progress. 2022; 29: 101182. doi: 10.1016/j.tsep.2021.101182
18. Kumar S, Singh PK. A novel approach to manage temperature non-uniformity in minichannel heat sink by using intentional flow maldistribution. Applied Thermal Engineering. 2019; 163: 114403. doi: 10.1016/j.applthermaleng.2019.114403

Thermal Science and Engineering 2024, 7(3), 8297.
https://doi.org/10.24294/tse.v7i3.8297

Article

Study of different theories of thermoelasticity under the propagation of Rayleigh waves in thermoelastic medium

Manoj Kumar[1], Shruti Goel[1,*], Vandana Gupta[2], Puneet Bansal[3], Pawan Kumar[4]

[1] Baba Mastnath University, Haryana 124021, India
[2] Indira Gandhi National College, Haryana 136132, India
[3] University Institute of Engineering and Technology (UIET), Kurukshetra University, Haryana 136119, India
[4] State Institute of Engineering & Technology (SIET), Kurukshetra University, Haryana 136117, India
*** Corresponding author:** Shruti Goel, shruti1922goel@gmail.com

CITATION

Kumar M, Goel S, Gupta V, et al. Study of different theories of thermoelasticity under the propagation of Rayleigh waves in thermoelastic medium. Thermal Science and Engineering. 2024; 7(3): 8297. https://doi.org/10.24294/tse.v7i3.8297

ARTICLE INFO

Received: 21 July 2024
Accepted: 24 August 2024
Available online: 10 September 2024

COPYRIGHT

Copyright © 2024 by author(s). *Thermal Science and Engineering* is published by EnPress Publisher, LLC. This work is licensed under the Creative Commons Attribution (CC BY) license. https://creativecommons.org/licenses/by/4.0/

Abstract: The present research is on the propagation of Rayleigh waves in a homogenous thermoelastic solid half-space by considering the compact form of six different theories of thermoelasticity. The medium is subjected to an insulated boundary surface that is free from normal stress, tangential stress, and a temperature gradient normal to the surface. After developing a mathematical model, a dispersion equation is obtained with irrational terms. To apply the algebraic method, this equation must be converted into a rational polynomial equation. From this, only those roots are filtered out, which has satisfied both of the above equations for the propagation of waves decaying with depth. With the help of these roots, different characteristics are computed numerically, like phase velocity, attenuation coefficient, and path of particles. Various particular cases are compared graphically by using phase velocity and attenuation coefficient. The elliptic path of surface particles in Rayleigh wave propagation is also presented for the different theories using physical constants of copper material for different depths and thermal conductivity.

Keywords: coupled model; dual phase lag model; G-N model; three phase lag model; G-L model; L-S model; phase velocity; attenuation coefficient

1. Introduction

The reaction of both natural and artificial materials to wave propagation parameters, such as travel periods (or phase velocities) and wave polarization (particle oscillations), is used to assess the materials. Thermal conductivity, thermal expansion, and specific heat all have an impact on these quantifiable values. The theory of thermoelasticity examines how an elastic medium's temperature affects the way strain and stress are distributed, as well as how induced deformation affects the temperature distribution in the opposite direction.

Biot [1] developed the theory of thermoelasticity known as coupled theory with hyperbolic-parabolic field equations. Green and Lindsay [2] and Lord and Shulman [3] extended the coupled theory and named it generalized thermoelasticity. Green and Naghdi [4] developed a theory of thermoelasticity without energy dissipation. These theories [2–4] admit a finite speed of heat propagation, which creates the difference from coupled theory. Hetnarski and Ignaczak [5] and Ignaczak and Ostoja-Starzewski [6] have reviewed these representative theories of generalized thermoelasticity. Tzou [7] defined the two-stage lag model. Choudhuri [8] identified the initiative in the three-phase lag model. Problems of wave propagation in coupled or generalized thermoelasticity have been studied by various researchers [9–15].

Wave propagation phenomena have numerous applications in the fields of geophysical exploration, mineral and oil exploration, and seismology. Plane wave propagation in thermoelasticity has many applications in various engineering fields. The surface waves are very helpful for studying various aspects of an earthquake. Rayleigh [16] studied the surface waves that propagate along the free surface of an elastic solid medium. To observe the structural and mechanical properties of any material, these Rayleigh waves are used because waves can travel along the surface and penetrate to a depth of thick solid materials of one wave length and show very sensitive behavior to surface defects. The Rayleigh-type surface waves in thermoelasticity are considered to be used in different engineering fields and future technologies. Many applications of the Rayleigh wave in the theory of thermoelasticity have been reported to date. Some of them are as follows: Lockett [17] studied the effect of a change in Rayleigh wave velocity on a change in thermal conditions. Flavin [18] studied the effect of Rayleigh waves in three mutually perpendicular directions at a constant temperature. Chadwick and Windle [19] studied the effects of the propagation of Rayleigh waves along insulated and isothermal boundaries. Tomita and Shindo [20] examine the effect of magnetic fields on the propagation of Rayleigh waves in a perfectly conducting elastic half-space. Dawn and Chakraborty [21] considered the Rayleigh wave study in thermoelastic media with Green and Lindsay theory. Abd-Alla and Ahmed [22] investigated the influence of initial stress and gravity fields on the propagation of surface waves in an orthotropic thermoelastic medium. Ahmed [23] studied the effect of thermal stress on the propagation of Rayleigh waves in a granular medium. Sharma et al. [24] investigated the effect of Rayleigh surface waves in piezo thermoelastic half-space under the influence of rotation and thermal relaxation. Abouelregal [25] studied the Rayleigh waves in a thermoelastic solid half space using a dual-phase-lag model with surface boundary conditions. Mahmoud [26] investigated the effect of magnetic field, rotation, relaxation times, gravity field, and initial stress on Rayleigh wave velocity in the space of a granular medium. Chirita [27] studied the surface waves in an isotropic thermoelastic half-space. Bucur et al. [28] analyzed the damping effects of thermal fields on Rayleigh waves and plane harmonic waves in a linear thermoelastic material with voids. Passarella et al. [29] considered the G-N theory to study the effect of the propagation of Rayleigh waves in strongly elliptic thermoelastic materials with micro-temperatures.

Biswas et al. [30] considered a three-phase-lag model of thermoelasticity to study the propagation of Rayleigh surface waves in an orthotropic thermoelastic homogenous half-space. Singh and Verma [31] studied the propagation of the Rayleigh wave in thermoelastic solid half-space by considering different theories of thermoelasticity. Kumar and Sangeeta [32] studied the basic equation of thermoelasticity by considering L-S theory under the effects of initial stress, magnetic field, two temperatures, and diffusion. Kumar and Gupta [33] investigated Rayleigh waves in a generalized thermoelastic medium with mass diffusion. Sharma [34,35] studied the Rayleigh wave at the surface of a general anisotropic poroelastic medium: derivation of a real secular equation and Rayleigh waves at the boundary of an orthotropic elastic solid: influence of initial stress and gravity. Hague and Biswas [36] studied the wave propagation with the help of the Eigen value of an algebraic differential equation. Find phase velocity and attenuation coefficient and compare the graph for void and non-void space. Saeed et al. [37] discussed Rayleigh wave propagation in a semi-conductor thermoelastic medium having temperature-dependent properties.

The present paper is arranged as follows: First, we provide the necessary equations used in the paper and discuss the compact form of the heat conduction equation in Section 2. In Section 3, we formulate the problem in the form of a potential function. In Section 4, find the velocities of longitudinal and transversal waves with the help of potential functions. In Section 5, boundary conditions are applied to find the dispersion equation and its filtered roots. Which are utilized to discover different properties of the Rayleigh wave: the phase velocity, attenuation coefficient, and path of the particle. In Section 6, a comparison between six special cases is exhibited by presenting the phase velocity, attenuation coefficient, and path of the particle traced in motion graphically.

2. Basic equations

Following Kumar and Gupta [38], a compact form of the equations for thermoelasticity theories in the absence of external heat sources are:

The temperature-stress-strain relationship is:

$$\sigma_{ij} = 2\mu e_{ij} + \lambda e_{kk}\delta_{ij} - \delta_{ij}\beta\left(1 + \tau_1 \frac{\partial}{\partial t}\right)T \tag{1}$$

Relation between strain and displacement:

$$e_{ij} = \frac{1}{2}\left(u_{i,j} + u_{j,i}\right) \tag{2}$$

The equations of motion:

$$(\lambda + \mu)u_{k,ki} + \mu u_{i,kk} - \beta\left(1 + \tau_1 \frac{\partial}{\partial t}\right)T_{,i} = \rho \ddot{u}_i \tag{3}$$

Modified Fourier's law:

$$K'\left(n^* + t_1 \frac{\partial}{\partial t} + t_3 \frac{\partial^2}{\partial t^2}\right)T_{,i} = -q_i \tag{4}$$

Energy equation:

$$\rho T_0 \dot{S} = -q_{i,i} \tag{5}$$

Entropy-strain-temperature relation:

$$\begin{aligned}\rho C_E&\left(n_1 \frac{\partial}{\partial t} + \tau_0 \frac{\partial^2}{\partial t^2} + t_2 \frac{\partial^3}{\partial t^3} + t_4 \frac{\partial^4}{\partial t^4}\right)T \\ &+ T_0\beta\left(n_1 \frac{\partial}{\partial t} + n_0\tau_0 \frac{\partial^2}{\partial t^2} + t_2 \frac{\partial^3}{\partial t^3} + t_4 \frac{\partial^4}{\partial t^4}\right)e_{kk} = \rho T_0 \dot{S}\end{aligned} \tag{6}$$

The heat conduction equation:

$$\begin{aligned}K'\left(n^* + t_1 \frac{\partial}{\partial t} + t_3 \frac{\partial^2}{\partial t^2}\right)T_{,ii} &= \rho C_E\left(n_1 \frac{\partial}{\partial t} + \tau_0 \frac{\partial^2}{\partial t^2} + t_2 \frac{\partial^3}{\partial t^3} + t_4 \frac{\partial^4}{\partial t^4}\right)T + \\ &T_0\beta\left(n_1 \frac{\partial}{\partial t} + n_0\tau_0 \frac{\partial^2}{\partial t^2} + t_2 \frac{\partial^3}{\partial t^3} + t_4 \frac{\partial^4}{\partial t^4}\right)e_{kk},\end{aligned} \tag{7}$$

In the Equations (1)–(7) λ and μ are lame's constants, ρ is the density, C_E is the specific heat at the constant strain, q_i, u_i are heat flux and displacement components, and increase in temperature. σ_{ij} are stress tensor components, S is entropy per unit mass, K' is thermal conductivity, $T = \theta - T_0$ is small increment in temperature, where T_0 reference temperature and θ absolute temperature with condition satisfied as $|T/T_0| < 1$, e_{kk} is the dilatation, $\beta = (3\lambda + 2\mu)\alpha_t$, $\alpha_t$coefficient of thermal linear expansion, $\tau_0,\ \tau_1,\ \tau_T,\ \tau_q,\ \tau_v$ are thermal relaxation times with condition $\tau_1 \geq \tau_0 \geq 0$, phase lags of temperature gradient, heat flux and thermal displacement gradient respectively, where $n^*,\ n_0,\ n_1, t_1, t_3,\ t_2,\ t_4,\ \tau_0,\ \tau_1$, are parameters.

Rayleigh wave propagation in a thermoelastic medium. The different theories are studied by using the values of parameters in Equations (3) and (7) as follows:

1) Coupled theory (C-T) condition of thermoelasticity is obtained when.

$$n^* = \mathrm{n}_1 = 1,\ n_0 = t_1 = t_2 = t_3 = t_4 = \tau_0 = \tau_1 = 0 \tag{8}$$

2) The Lord-Shulman (L-S) theory of thermoelasticity is obtained when.

$$n^* = n_0 = n_1 = 1, t_1 = t_2 = t_3 = t_4 = \tau_1 = 0 \tag{9}$$

3) The Green- Lindsay (G-L) theory of thermoelasticity is obtained when.

$$n^* = n_1 = 1,\ n_0 = t_1 = t_2 = t_3 = t_4 = 0 \tag{10}$$

4) The Green-Nagdhi (Type-III) (G-N) theory of thermoelasticity is obtained when.

$$n^* > 0, \mathrm{n}_0 = \tau_0 = t_1 = 1, \mathrm{n}_1 = t_2 = t_3 = t_4 = \tau_1 = 0 \tag{11}$$

Put in Equation (7) results into equation:

$$K'\left(n^* + \frac{\partial}{\partial t}\right)T_{,ii} = \rho C_E \ddot{T} + \beta T_0 \ddot{e}_{kk} \tag{12}$$

Here n^* = constant having a dimension $\frac{1}{sec}$, $\dot{T} = \vartheta$ and $n^* K' = K'^*$ is a constant characteristic of the theory. Equation (12) become.

$$K'^* T_{,ii} + K' \vartheta_{,ii} = \rho C_E \ddot{T} + \beta T_0 \ddot{e}_{kk} \tag{13}$$

Subcase: When $K' = 0$ in Equation (13) Green-Nagdhi (Type-II) theory is obtained.

5) The two-phase-lag theory of thermoelasticity is obtained when.

$$n^* = 1, n_0 = \mathrm{n}_1 = 1, \tau_1 = t_3 = t_4 = 0, t_1 = \tau_T,\ t_2 = \frac{\tau_q^2}{2}, \tau_0 = \tau_q \tag{14}$$

6) The three-phase-lag theory of thermoelasticity is obtained when.

$$n_0 = \tau_0 = 1, n_1 = \tau_1 = 0, t_2 = \tau_q, t_1 = 1 + n^* \tau_v, t_3 = \tau_T, t_4 = \frac{\tau_q^2}{2} \tag{15}$$

3. Formulation of problem

To solve the problem related to two-dimensional space, consider the displacement vector $u = (u_1, 0, u_3)$ in medium. We define the following dimensionless quantities:

$$T' = \frac{\beta T}{\rho c_1^2},\ \{x_i', u_i'\} = \left\{\frac{\omega_1^* x_i}{c_1}, \frac{\omega_1^* u_i}{c_1}\right\}\ i = 1, 3,\ \nabla^2 = \frac{\partial^2}{\partial x_1^2} + \frac{\partial^2}{\partial x_3^2},$$

$$t' = \omega_1^* t, \{\tau_0', \tau_1', \tau_q', \tau_v', \tau_T'\} = \{\tau_0, \tau_1, \tau_q, \tau_v, \tau_T\}\omega_1^*, \tag{16}$$

$$\sigma_{ij}' = \frac{\sigma_{ij}}{\beta T_0}, \omega_1^* = \frac{\rho C_E C_1^2}{K'},\ \ C_1^2 = \frac{\lambda + 2\mu}{\rho},\ \ C_2^2 = \frac{\mu}{\rho},\ \delta^2 = \frac{C_2^2}{C_1^2},$$

The displacement components in form of potential function $\phi_1,\ \phi_2,\ \phi_3$can be written as:

$$u_1 = \frac{\partial \phi_1}{\partial x_1} + \frac{\partial \phi_2}{\partial x_1} + \frac{\partial \phi_3}{\partial x_3},\ u_3 = \frac{\partial \phi_1}{\partial x_3} + \frac{\partial \phi_2}{\partial x_3} - \frac{\partial \phi_3}{\partial x_1} \tag{17}$$

In Equations (3) and (7) with the help of (16), after suppressing the primes, apply the Equation (17) we obtain:

$$\left(\nabla^2 - \frac{\partial^2}{\partial t^2}\right)\varphi - \left(1 + \tau_1 \frac{\partial}{\partial t}\right)T = 0 \tag{18}$$

$$\nabla^2 \varphi_3 - \frac{1}{\delta^2}\frac{\partial^2 \varphi_3}{\partial t^2} = 0 \tag{19}$$

$$\begin{aligned}\left(m^* + t_1 \frac{\partial}{\partial t} + t_3 \frac{\partial^2}{\partial t^2}\right)\nabla^2 T \\ = \left(m_1 \frac{\partial}{\partial t} + \tau_0 \frac{\partial^2}{\partial t^2} + t_2 \frac{\partial^3}{\partial t^3} + t_4 \frac{\partial^4}{\partial t^4}\right)T \\ + \frac{\beta^2 T_0}{\rho^2 C_E c_1^2}\left(n_1 \frac{\partial}{\partial t} + n_0 \tau_0 c \frac{\partial^2}{\partial t^2} + t_2 c^2 \frac{\partial^3}{\partial t^3} + t_4 c^3 \frac{\partial^4}{\partial t^4}\right)\nabla^2 \varphi\end{aligned} \tag{20}$$

4. Solution of problem

We assume, for propagation of harmonic wave in consider plane as:

$$\{\phi, \phi_3, T\}(x_1, x_3, t) = \{\bar{\phi}, \bar{\phi}_3, \bar{T}\}e^{-i\omega t} \tag{21}$$

Substitute the Equation (21) in Equations (18) and (20) and then simplified, we get:

$$(Z_1 \nabla^4 + Z_2 \nabla^2 + Z_3)\bar{\varphi} = 0 \tag{22}$$

where:

$$Z_1 = S_2,\ Z_2 = S_2\omega^2 - S_3 - S_1 S_4,\ Z_3 = -\omega^2 S_3\ S_1 = 1 - i\omega\tau_1,\ S_2 \\ = (n^* - it_1\omega - t_3\omega^2)$$

$$S_3 = (-in_1\omega - \tau_0\omega^2 + it_2\omega^3 + t_4\omega^4),$$

$$S_4 = (\beta^2 T_0 / \rho^2 C_E C_1^2)(-in_1\omega - \tau_0 n_0 \omega^2 + it_2\omega^3 + t_4\omega^4),$$

General solution $\bar{\phi}$ can be written as:

$$\bar{\phi} = \bar{\phi}_1 + \bar{\phi}_2 \tag{23}$$

The potential $\bar{\phi}_1,\ \bar{\phi}_2$ are solutions of equation given by:

$$\left[\nabla^2 + \frac{\omega^2}{V_i^2}\right]\bar{\varphi}_i = 0, \quad i = 1,\ \ 2 \tag{24}$$

V_1, V_2, are the velocities of longitudinal waves ($P$and SVwave), roots of equation:

$$Z_3 V^4 - Z_2 \omega^2 V^2 + Z_1 \omega^4 = 0 \tag{25}$$

By using the Equation (21) in Equation (19) we get velocity of transverse wave $V_3 = \delta$ given by:

$$\left[\nabla^2 + \frac{\omega^2}{V_3^2}\right]\bar{\varphi}_3 = 0, \tag{26}$$

By using the Equations (7), (21), (23) and (24) we obtain:

$$\{\varphi, T\} = \sum_{i=1}^{2} \{1, m_i\}\varphi_i, \tag{27}$$

where:

$$m_i = \frac{S_1 S_4 \omega^2}{S_1 S_2 \omega^2 - S_3 {V_i}^2}, \quad i = 1,\ 2$$

The displacement potential ϕ_i for the propagation of harmonic wave with exponential decay in a plane is given as:

$$\varphi_i = A_i e^{i\omega\left(\frac{x_1+q_i x_3}{c}-t\right)}, \quad i = 1,\ 2,\ 3 \tag{28}$$

where: *c* is the apparent phase velocity and $q_i = \sqrt{\frac{c^2}{{V_i}^2}-1}, \quad i = 1,\ 2, \quad q_3 = \sqrt{\frac{c^2}{\delta^2}-1}.$

5. Boundary conditions

For the surface which is free from stress and insulated in nature.

Vanish normal and tangential stress component.

$$\sigma_{33} = 0 \tag{29}$$

$$\sigma_{31} = 0 \tag{30}$$

Vanish of temperature gradient normal to insulated surface.

$$\frac{\partial T}{\partial x_3} = 0 \tag{31}$$

By using the Equation (28) in Equations (29)–(31) with the help of Equations (1), (2), (17) and (27) we get system of three homogenous equations as:

$$\sum_{k=1}^{3} c_{ik} A_k = 0 \tag{32}$$

where:

$$c_{11} = -\omega^2\Pi_1 + 2\frac{\omega^2}{h} - \beta\frac{m_1}{\rho},\quad c_{12} = -\omega^2\Pi_2 + 2\frac{\omega^2}{h} - \beta\frac{m_2}{\rho},\quad c_{13} = 2\frac{\omega^2 q_3}{h}, c_{21} = 2q_1,\quad c_{22} = 2q_2,\quad c_{23} = q_3^2 - 1,\quad c_{31} = m_1 q_1,\quad c_{32} = m_2 q_2,\quad c_{33} = 0$$

A non-trivial solution of a homogeneous system of equations is obtained when the determinant of coefficients of Equation (32) vanishes. We get:

$$(2-h)[(2-\Pi_1 h) - \eta(2-\Pi_2 h)(q_1/q_2)] = -4(1-\eta)q_1 q_3 \tag{33}$$

where:

$$h = \frac{c^2}{\delta^2},\quad \eta = \frac{m_1}{m_2},\quad \Pi_i = \frac{\lambda+2\mu}{\rho V_i^2} + \frac{m_i\alpha_t(1-i\omega\tau_1)}{\omega^2}\quad , i = 1,\ 2$$

In Equation (32) some terms are irrational due to this; it is not possible to solve it by using the algebraic method. To solve this equation, remove radicals by three squaring and manipulation, which reduce the given equation to an algebraic equation of degree 9, written as follows:

$$\sum_{k=0}^{9} c_k h^k = 0 \tag{34}$$

where:

$$c_0 = 2a_0a_1 - 4(2b_0b_1 - \varepsilon_s b_0^2)p;$$

$$c_1 = a_1^2 + 2a_0a_2 - 4\left(b_1^2 + 2b_0b_2 + \varepsilon_p b_0^2 - 2\varepsilon_s b_0 b_1\right),$$

$$c_2 = 2(a_0a_3 + a_2a_1) - 4\left(2b_0b_3 + 2b_1b_2 + 2\varepsilon_p b_0b_1 - \varepsilon_s(b_1^2 + 2b_0b_2)\right),$$

$$c_3 = a_2^2 + 2a_1a_3 + 2a_0a_4 - 4\left[b_2^2 + 2b_1b_3 + 2b_0b_4 + \varepsilon_p(b_1^2 + 2b_0b_2) - 2\varepsilon_s(b_1b_2 + b_0b_3)\right],$$

$$c_4 = 2(a_0a_5 + a_1a_4 + a_2a_3) - 4\big[2b_1b_4 + 2b_2b_3 + 2\varepsilon_p b_0b_3 + 2\varepsilon_p b_1b_2 - \\ \varepsilon_s(b_2^2 + 2b_1b_3 + 2b_0b_4)\big],$$

$$c_5 = a_3^2 + 2a_1a_5 + 2a_2a_4 - 4\big[b_3^2 + 2b_2b_4 + \varepsilon_p(b_2^2 + 2b_1b_3 + 2b_0b_4) - \\ 2\varepsilon_s(b_2b_3 + b_1b_4)\big],$$

$$c_6 = 2(a_3a_4 + a_2a_5) - 4\big[2b_3b_4 + 2\varepsilon_p(b_2b_3 + b_1b_4) - \varepsilon_s(2b_2b_4 + b_3^2)\big],$$

$$c_7 = a_4^2 + 2a_3a_5 - 4\big[b_4^2 + \varepsilon_p(2b_2b_4 + b_3^2) - 2\varepsilon_s b_4b_3\big],$$

$$c_8 = 2a_4a_5 - 4\big(2\varepsilon_p b_4b_3 - \varepsilon_s b_4^2\big),\ c_9 = a_5^2 - 4\varepsilon_p b_4^2,$$

$$a_0 = 32\eta,\ a_1 = 16[g_1 + \eta g_2 - \varepsilon_2 - \eta^2\varepsilon_1 + (1-\eta)^2(1+\varepsilon_s)],$$

$$a_2 = 4(g_1^2 + g_2^2) + 8(\Pi_1 + n^2\Pi_2) - 16\big[g_1\varepsilon_2 + ng_2\varepsilon_1 + (1-n)^2\big(\varepsilon_p + \varepsilon_s\big)\big],$$

$$a_3 = 4(\Pi_1g_1 + \Pi_2g_2n - g_1^2\varepsilon_2 - g_2^2\varepsilon_1) - 8(\Pi_1\varepsilon_2 + n\Pi_2\varepsilon_1) + 16(1-n)^2\varepsilon_p,$$

$$a_4 = \Pi_1^2 + n\Pi_2^2 - 4(\varepsilon_2g_1\Pi_1 + n\varepsilon_1g_2\Pi_2), a_5 = -(\Pi_1^2\varepsilon_2 + n^2\Pi_2^2\varepsilon_1)$$

$$b_0 = 16\eta,\ b_1 = 8(g_2 + \eta g_1),\ \ b_2 = 4\eta(\Pi_1 + \Pi_2) + 4g_1g_2,$$

$$b_3 = 2(\Pi_1g_2 + \eta\Pi_2g_1),\ \ b_4 = \eta\Pi_1\Pi_2,\ g_1 = -(1+\Pi_1),\ \ g_2 = -\eta(1+\Pi_2),$$

$$\varepsilon_s = \varepsilon_1 + \varepsilon_2,\ \varepsilon_p = \varepsilon_1\varepsilon_2,\ \ \varepsilon_i = \left(\frac{\delta}{V_i}\right)^2,\ i = 1,\ 2.$$

An algebraic Equation (34) gives seven complex roots, of which some are added during the removal of radicals. These roots are identified and separated by not satisfying the original dispersion Equation (33). The remaining roots that satisfied Equation (33) are considered for decay of the wave field with an increase of x_3 in the medium. These roots are satisfied, and both the Equations (33) and (34) represent the propagation and existence of Rayleigh waves in an insulated plane boundary of a thermoelastic medium. The coefficient c_i depends upon ω therefore, the phase velocity V calculated from a root of Equation (32) is also a function of ω. This implies the dispersive behavior of the Rayleigh wave on an insulated surface in a thermoelastic medium.

By following Sharma [39], the phase velocity and attenuation coefficient can be calculated as:

Phase Velocity:

$$V = \frac{|c^2|}{Re(c)} = \frac{\delta|h|}{Re\big(\sqrt{h}\big)} \tag{35}$$

Attenuation Coefficient:

$$Q^{-1} = \frac{Im(1/c^2)}{Re(1/c^2)} = -\frac{Im(h)}{Re(h)} \tag{36}$$

Path of surface Particles:

$$\varphi_i = A_1\gamma_i e^{i(kx_1-\omega t)+ikx_3q_i}, i = 1,2,3 \tag{37}$$

where: $\gamma_i = A_i/A_1,\quad i = 1,2,3$ are solution of Equation (30) and $k = \omega/c$ is the complex number.

where: $\gamma_1 = 1,\ \gamma_2 = -\eta q_1/q_2,\ \ \gamma_3 = 2q_1\left(\frac{\eta-1}{q_3^2-1}\right),$

By using Equation (37) in Equations (17) and (23), we get:

$$(u_1, u_3) = \big(|U_0|e^{i\,arg\,U_0}, |W_0|e^{i\,arg\,W_0}\big)e^{i(kx_1-\omega t)} \tag{38}$$

$$\begin{pmatrix} U_0 \\ W_0 \end{pmatrix} = \begin{pmatrix} i\big[\gamma_1 e^{ik_Rx_3\delta_1} + \gamma_2 e^{ik_Rx_3\delta_2} + \gamma_3 q_3 e^{ik_Rx_3\delta_3}\big] \\ \big[\gamma_1 q_1 e^{ik_Rx_3\delta_1} + \gamma_2 q_2 e^{ik_Rx_3\delta_2} - \gamma_3 e^{ik_Rx_3\delta_3}\big] \end{pmatrix} kA_1 e^{i(kx_1-\omega t)} \tag{39}$$

where: $\delta_i = \left(1 - i\frac{c_I}{c_R}\right) q_i,\ i = 1,\ 2,\ 3.$

R is used for real part and I is used for imaginary part of complex quantity, K is wave number.

By using Equations (37) and (27), we get:

$$T = |T_0| e^{i\, arg\, T_0} e^{i(kx_1 - \omega t)} \tag{40}$$

$$T_0 = A_1\left(m_1\gamma_1 e^{ik_R x_3 \delta_1} + m_2\gamma_2 e^{ik_R x_3 \delta_2}\right) \tag{41}$$

On the boundary surface $x_3 = 0$ the Equation (38) by considering real part we get:

$$U = |U_0| e^{-k_I x_1} cos(arg\, U_0 + \Phi),\quad W = |W_0| e^{-k_I x_1} \sin(arg\, W_0 + \Phi) \tag{42}$$

$\Phi = K_R x - \omega t$ parameter varies in $(0, 2\pi)$ to show the path traced. By using Equations (28) in parametric form traces elliptical path.

Special cases

Case 1: To obtain the secular equation for Coupled theory of thermoelasticity. Put $n^* = \mathrm{n}_1 = 1,\ n_0 = t_1 = t_2 = t_3 = t_4 = \tau_0 = \tau_1 = 0$, in Equation (25).

For $\Pi_1 = 0,\ \eta = 0$ Equation (33) reduces to equation $(2 - h)^2 = -4q_1q_3$ which represents Rayleigh wave propagation in elastic medium. Similar to Ewing et al. [40].

Case 2: When the condition $n^* = n_0 = n_1 = 1, t_1 = t_2 = t_3 = t_4 = \tau_1 = 0$, with one relaxation of time, applied in Equation (25), yields the secular equation for L-S theory of thermoelasticity.

Case 3: When the condition $n^* = n_1 = 1,\ n_0 = t_1 = t_2 = t_3 = t_4 = 0$, with two relaxations of times, applied in Equation (25), yields the secular equation for the G-L theory of thermoelasticity.

Case 4: When the condition $n^* > 0, \mathrm{n}_0 = \tau_0 = t_1 = 1, \mathrm{n}_1 = t_2 = t_3 = t_4 = \tau_1 = 0$, applied in Equation (25), we obtained G-N (Type-III) theory of thermoelasticity.

Case 5: To obtain secular equation for Two-phase lag theory of thermoelasticity apply $n^* = 1, n_0 = n_1 = 1, \tau_1 = t_3 = t_4 = 0, t_1 = \tau_T,\ t_2 = \frac{\tau_q^2}{2}, \tau_0 = \tau_q$, in Equation (25).

Case 6: To obtain secular equation for three-phase lag theory of thermoelasticity apply $n_0 = \tau_0 = 1, n_1 = \tau_1 = 0, t_2 = \tau_q, t_1 = 1 + n^*\tau_v, t_3 = \tau_T, t_4 = \frac{\tau_q^2}{2}$, in Equation (25).

6. Numerical results and discussion

6.1. Findings of phase velocity, attenuation coefficient

The software MATLAB is used to compare phase velocity and attenuation coefficient for the different theories of thermoelasticity by using frequencies in the range of 0.1 Hz to 59.1 Hz.

Now we find numerical results by using physical constants of copper material, followed by [39], which are given below:

$$\lambda = 77.6 \text{ GPa}, \quad T_0 = 318 \text{ K}, \alpha_t = 1.78 \times 10^{-5} \text{K}^{-1}, \quad \mu = 38.6 \text{ GPa}, \text{C}_\text{E} = 383 \text{ J Kg}^{-1}/\text{K}, \quad \rho = 8920 \text{ kg/m}^3, \quad K^{'} = 400 \text{Wm}^{-1}$$

The relaxation time is given below:

$$\tau_0 = 0.1 \text{ s}, \tau_1 = 0.2 \text{ s}, \tau_q = 0.6 \text{ s}, \ \tau_T = 0.4 \text{ s}, \ \tau_v = 0.5 \text{ s}, \ \ n^* = 0.38710 \ \text{sec}^{-1}.$$

The output of the program is shown in **Tables 1** and **2** for comparing different theories of thermoelasticity with frequency.

Table 1. Value of phase velocity (*V*) w.r.t frequency ω in context of different theories of thermoelasticity.

Frequency ω	**C-T (*V*)**	**L-S (*V*)**	**G-L (*V*)**	**G-N (*V*)**	**DPL (*V*)**	**TPL (*V*)**
0.1	0.4923	0.492	0.4908	0.45	0.4917	0.45
1.1	0.437	0.4405	0.4495	0.4544	0.4511	0.4505
2.1	0.4526	0.4596	0.5079	0.4551	0.4985	0.5291
3.1	0.4662	0.4775	0.5152	0.3173	0.3939	0.3975
4.1	0.4765	0.4928	0.4863	0.2416	0.2883	0.3177
5.1	0.4843	0.4742	0.4305	0.1948	0.2211	0.2628
6.1	0.5676	0.4149	0.3712	0.1631	0.1761	0.2233
7.1	0.5267	0.3691	0.3217	0.1403	0.1444	0.1938
8.1	0.4935	0.3324	0.2825	0.1231	0.1212	0.1709
9.1	0.4658	0.3025	0.2514	0.1096	0.1036	0.1528
10.1	0.4423	0.2774	0.2262	0.0988	0.0899	0.1381
11.1	0.422	0.2561	0.2055	0.0899	0.0789	0.126
12.1	0.4043	0.2378	0.1882	0.0825	0.07	0.1158
13.1	0.3887	0.2219	0.1736	0.0762	0.0627	0.1071
14.1	0.3747	0.208	0.1611	0.0708	0.0566	0.0996
15.1	0.3621	0.1957	0.1502	0.0661	0.0514	0.0931
16.1	0.3507	0.1847	0.1407	0.062	0.0469	0.0874
17.1	0.3403	0.1749	0.1323	0.0584	0.0431	0.0823
18.1	0.3308	0.166	0.1249	0.0552	0.0398	0.0778
19.1	0.3221	0.158	0.1182	0.0523	0.0368	0.0738
20.1	0.314	0.1507	0.1123	0.0497	0.0343	0.0701
21.1	0.3065	0.144	0.1068	0.0474	0.032	0.0668
22.1	0.2995	0.1379	0.1019	0.0452	0.0299	0.0638
23.1	0.2929	0.1323	0.0975	0.0433	0.0281	0.0611
24.1	0.2868	0.1271	0.0933	0.0415	0.0264	0.0585
25.1	0.281	0.1223	0.0896	0.0398	0.0249	0.0562
26.1	0.2756	0.1178	0.0861	0.0383	0.0235	0.0541
27.1	0.2705	0.1137	0.0829	0.0369	0.0223	0.0521
28.1	0.2656	0.1098	0.0799	0.0356	0.0212	0.0502
29.1	0.261	0.1062	0.0771	0.0343	0.0201	0.0485
30.1	0.2567	0.1028	0.0745	0.0332	0.0192	0.0469
31.1	0.2525	0.0996	0.0721	0.0321	0.0183	0.0454
32.1	0.2485	0.0966	0.0698	0.0311	0.0174	0.044

Table 1. (*Continued*).

Frequency ω	**C-T (V)**	**L-S (V)**	**G-L (V)**	**G-N (V)**	**DPL (V)**	**TPL (V)**
33.1	0.2448	0.0938	0.0677	0.0302	0.0167	0.0427
34.1	0.2412	0.0911	0.0657	0.0293	0.016	0.0414
35.1	0.2377	0.0886	0.0638	0.0285	0.0153	0.0402
36.1	0.2344	0.0862	0.062	0.0277	0.0147	0.0391
37.1	0.2312	0.084	0.0603	0.0269	0.0141	0.0381
38.1	0.2282	0.0818	0.0587	0.0262	0.0136	0.0371
39.1	0.2252	0.0798	0.0572	0.0256	0.0131	0.0361
40.1	0.2224	0.0778	0.0557	0.0249	0.0126	0.0352
41.1	0.2197	0.076	0.0544	0.0243	0.0122	0.0344
42.1	0.2171	0.0742	0.0531	0.0237	0.0117	0.0336
43.1	0.2145	0.0725	0.0518	0.0232	0.0113	0.0328
44.1	0.2121	0.0709	0.0506	0.0227	0.011	0.032
45.1	0.2097	0.0694	0.0495	0.0222	0.0106	0.0313
46.1	0.2074	0.0679	0.0484	0.0217	0.0103	0.0307
47.1	0.2052	0.0665	0.0474	0.0212	0.01	0.03
48.1	0.2031	0.0651	0.0464	0.0208	0.0097	0.0294
49.1	0.201	0.0638	0.0454	0.0204	0.0094	0.0288
50.1	0.199	0.0626	0.0445	0.02	0.0091	0.0282
51.1	0.197	0.0614	0.0437	0.0196	0.0088	0.0277
52.1	0.1951	0.0602	0.0428	0.0192	0.0086	0.0271
53.1	0.1933	0.0591	0.042	0.0188	0.0084	0.0266
54.1	0.1915	0.058	0.0412	0.0185	0.0081	0.0261
55.1	0.1898	0.057	0.0405	0.0181	0.0079	0.0257
56.1	0.1881	0.056	0.0397	0.0178	0.0077	0.0252
57.1	0.1864	0.055	0.039	0.0175	0.0075	0.0248
58.1	0.1848	0.0541	0.0384	0.0172	0.0073	0.0243
59.1	0.1832	0.0532	0.0377	0.0169	0.0071	0.0239

Table 1 is used to present the findings graphically for comparison of different theories of thermoelasticity. **Figure 1** shows the variation of the phase velocity with respect to frequency for different theories of thermoelasticity. In **Figures 1** and **2**, the solid blue line, red dash line, green dash line with asterisk, red dash line with circle, dark green only asterisk, and sky blue with plus sign correspond respectively to the coupled theory (C-T), Lord-Shulman theory (L-S), Green-Lincoln theory (G-L), Green-Naghdi (Type-III) theory (G-N), two-phase lag theory (DPL), and three-phase lag theory (TPL) of thermoelasticity.

Figure 1 depicts that the phase velocities decrease in all theories smoothly and finally give constant values with an increase in frequency. $\omega = 0.1$ all theories give phase velocity near 0.49 except G-N and three-phase-lag theories, which have little less value in comparison to others. The maximum value of V is attained by coupled theory, and the minimum value is given by two-phase lag theory. Phase velocities given by different Theories follow a pattern: at every fixed value of frequency, descending values of phase velocity are obtained by theories in the following order: coupled theory, L-S theory, G-L theory, three-phase lag theory, G-N theory, and at the last, two-phase lag theory. In the case of coupled theory, phase velocity takes a curved shape in the range $5.1 \leq \omega \leq 8.1$. Two-phase-lag theory and G-N theory overlap each other in the range $3.1 \leq \omega \leq 6.1$as phase velocities are very close to each other.

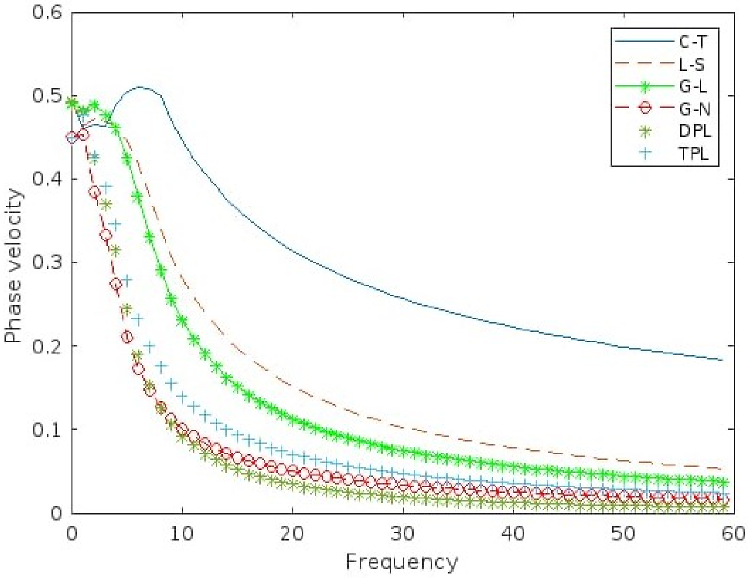

Figure 1. Variation of phase velocities V (m/s) with frequency ω (Hz) for different theories of thermoelasticity.

Table 2 is used to present the findings graphically for comparison of different theories of thermoelasticity. From **Figure 2**, it is depicted that in the case of coupled theory, the value of the attenuation coefficient jumped directly to 6.7789 from −0.1697 and was constant in the range $8.1 \leq \omega \leq 59.1$ up to one decimal place.

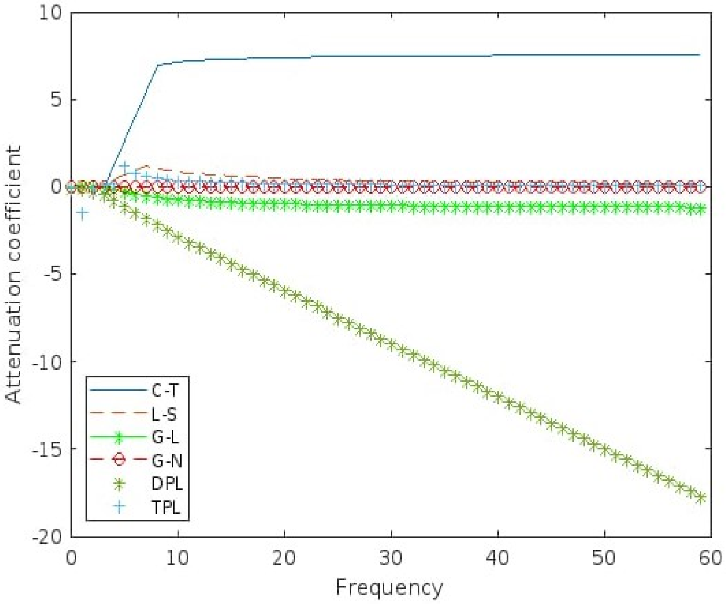

Figure 2. Variation of attenuation coefficient Q^{-1} with frequency ω (Hz) for theories.

Table 2. Value of Attenuation coefficient Q^{-1} w.r.t frequency ω in context of different theories of thermoelasticity.

Frequency ω	Q^{-1} **(C−T)**	Q^{-1} **(L−S)**	Q^{-1} **(G−L)**	Q^{-1} **(G−N)**	Q^{-1} **(DPL)**	Q^{-1} **(TPL)**
0.1	−0.1047	−0.1039	−0.1044	−0.0238	−0.103	0.45
1.1	−0.1101	−0.1071	0.1503	0.0204	−0.0643	0.4505
2.1	−0.1176	−0.1233	0.0975	−0.0719	−0.0053	0.5291
3.1	−0.1386	−0.1563	−0.0444	−0.0479	−0.3867	0.3975
4.1	−0.1562	−0.1916	−0.1856	−0.0379	−0.7994	0.3177
5.1	−0.1697	1.4524	−0.3295	−0.0318	−1.1739	0.2628
6.1	6.7789	1.271	−0.4536	−0.0275	−1.5272	0.2233
7.1	6.9052	1.1323	−0.551	−0.0243	−1.8671	0.1938
8.1	7.0003	1.0217	−0.6278	−0.0217	−2.1979	0.1709
9.1	7.0742	0.931	−0.6897	−0.0197	−2.5224	0.1528
10.1	7.1333	0.855	−0.7407	−0.018	−2.8423	0.1381
11.1	7.1815	0.7904	−0.7834	−0.0166	−3.1588	0.126
12.1	7.2215	0.7348	−0.8199	−0.0154	−3.4726	0.1158
13.1	7.2552	0.6864	−0.8513	−0.0143	−3.7844	0.1071
14.1	7.284	0.6439	−0.8787	−0.0134	−4.0946	0.0996
15.1	7.3087	0.6063	−0.9028	−0.0126	−4.4034	0.0931
16.1	7.3302	0.5728	−0.9241	−0.0119	−4.7112	0.0874
17.1	7.3491	0.5428	−0.9432	−0.0113	−5.018	0.0823
18.1	7.3657	0.5157	−0.9604	−0.0107	−5.3242	0.0778
19.1	7.3804	0.4911	−0.9758	−0.0102	−5.6297	0.0738
20.1	7.3935	0.4688	−0.9899	−0.0098	−5.9346	0.0701
21.1	7.4053	0.4484	−1.0027	−0.0094	−6.2391	0.0668
22.1	7.4159	0.4296	−1.0145	−0.009	−6.5432	0.0638
23.1	7.4255	0.4124	−1.0253	−0.0086	−6.8469	0.0611
24.1	7.4342	0.3965	−1.0352	−0.0083	−7.1503	0.0585
25.1	7.4422	0.3817	−1.0444	−0.008	−7.4535	0.0562
26.1	7.4494	0.368	−1.053	−0.0077	−7.7564	0.0541
27.1	7.4561	0.3552	−1.0609	−0.0074	−8.0591	0.0521
28.1	7.4622	0.3433	−1.0683	−0.0072	−8.3616	0.0502
29.1	7.4679	0.3321	−1.0753	−0.007	−8.664	0.0485
30.1	7.4731	0.3216	−1.0818	−0.0067	−8.9662	0.0469
31.1	7.478	0.3118	−1.0879	−0.0065	−9.2682	0.0454
32.1	7.4825	0.3026	−1.0936	−0.0064	−9.5701	0.044
33.1	7.4867	0.2938	−1.099	−0.0062	−9.8719	0.0427
34.1	7.4906	0.2856	−1.1041	−0.006	−10.1736	0.0414
35.1	7.4943	0.2778	−1.1089	−0.0058	−10.4752	0.0402
36.1	7.4977	0.2704	−1.1135	−0.0057	−10.7767	0.0391
37.1	7.5009	0.2634	−1.1178	−0.0056	−11.0782	0.0381
38.1	7.5039	0.2567	−1.122	−0.0054	−11.3795	0.0371
39.1	7.5068	0.2504	−1.1259	−0.0053	−11.6808	0.0361
40.1	7.5095	0.2444	−1.1296	−0.0052	−11.982	0.0352

Table 2. (*Continued*).

Frequency ω	Q^{-1} **(C–T)**	Q^{-1} **(L–S)**	Q^{-1} **(G–L)**	Q^{-1} **(G–N)**	Q^{-1} **(DPL)**	Q^{-1} **(TPL)**
41.1	7.512	0.2386	−1.1332	−0.005	−12.2832	0.0344
42.1	7.5144	0.2331	−1.1366	−0.0049	−12.5843	0.0336
43.1	7.5167	0.2279	−1.1398	−0.0048	−12.8854	0.0328
44.1	7.5188	0.2229	−1.1429	−0.0047	−13.1864	0.032
45.1	7.5208	0.2181	−1.1459	−0.0046	−13.4873	0.0313
46.1	7.5228	0.2135	−1.1487	−0.0045	−13.7883	0.0307
47.1	7.5246	0.209	−1.1514	−0.0044	−14.0892	0.03
48.1	7.5263	0.2048	−1.154	−0.0044	−14.39	0.0294
49.1	7.528	0.2007	−1.1566	−0.0043	−14.6908	0.0288
50.1	7.5296	0.1968	−1.159	−0.0042	−14.9916	0.0282
51.1	7.5311	0.1931	−1.1613	−0.0041	−15.2923	0.0277
52.1	7.5325	0.1895	−1.1635	−0.004	−15.5931	0.0271
53.1	7.5339	0.186	−1.1657	−0.004	−15.8938	0.0266
54.1	7.5352	0.1826	−1.1678	−0.0039	−16.1944	0.0261
55.1	7.5365	0.1794	−1.1698	−0.0038	−16.4951	0.0257
56.1	7.5377	0.1762	−1.1717	−0.0038	−16.7957	0.0252
57.1	7.5389	0.1732	−1.1736	−0.0037	−17.0963	0.0248
58.1	7.54	0.1703	−1.1754	−0.0036	−17.3969	0.0243
59.1	7.541	0.1674	−1.1771	−0.0036	−17.6974	0.0239

In the case of two-phase lag theory, a straight line is obtained with a decreasing slope as the value of the attenuation coefficient decreases smoothly with an increase in frequency along the negative axis. For the G-L theory, negative values of the attenuation coefficient were obtained with small differences in values and the same for up to one decimal place for increased frequency due to this straight line appearing. The values obtained by L-S and three-phase-lag theories are positive and near to zero within the range of frequency. In the case of the G-N theory, the negative value of the attenuation coefficient obtained very close to zero for increasing values of frequency. Due to the above L-S, G-N, and three-phase-lag theories, they overlap each other.

6.2. Findings of path of particle

All the special cases discussed in the form of different theories of thermoelasticity are presented graphically by using the output of MATLAB software in **Figures 3–8**. The polarization of particle motion in two-dimensional space is represented by (U, W).

Physical data of copper material used with frequency $\omega = 2\pi$ and parameter Φ varies in $(0,2\pi)$. Different depths vary as follows: $K_R x_3 = 0,\ 15,\ 45$. The coefficient of thermal linear expansion varies as follows: $\alpha_t = (1.78 \times e^{-2},\ 1.78 \times e^{-3},\ 1.78 \times e^{-4})\ \mathrm{K}^{-1}$. For one fixed value of depth, we present three figures for three different Coefficient of thermal linear expansion in such a way 9 figures obtained for three different depths in each of **Figures 3–8**. Computed for coupled theory, L-S theory, G-L theory, G-N theory, two-phase-lag model, and three-phase-lag model of thermoelasticity.

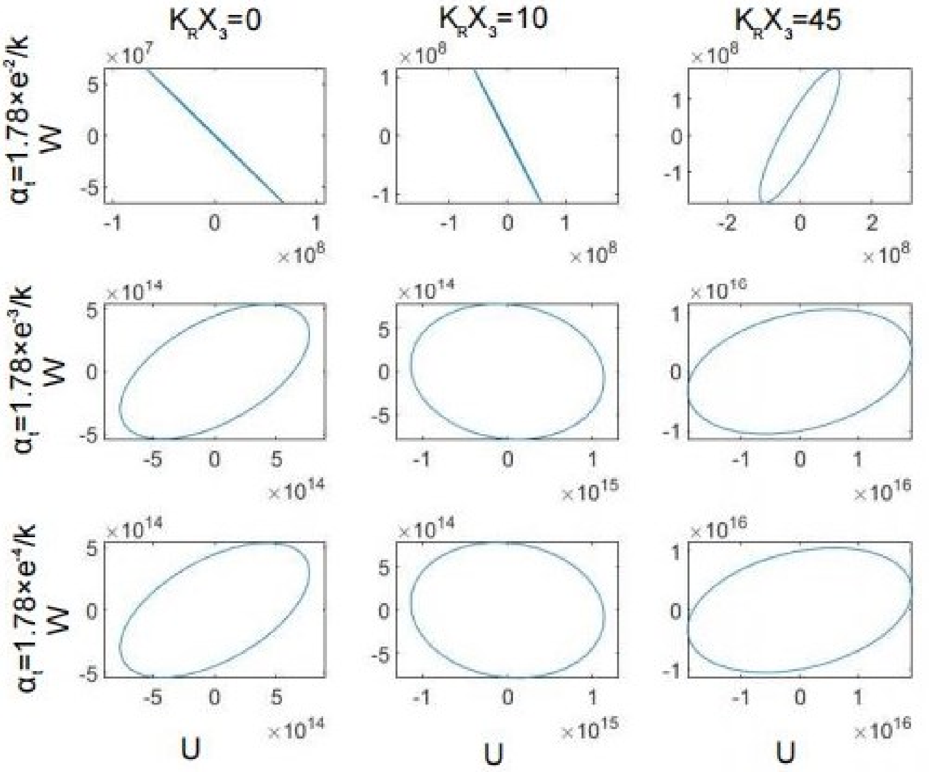

Figure 3. Variation of particle motion (U, W) with depth $K_R x_3 = 0,15,45$ for Couple theory of thermoelasticity and for L-S theory of thermoelasticity respectively.

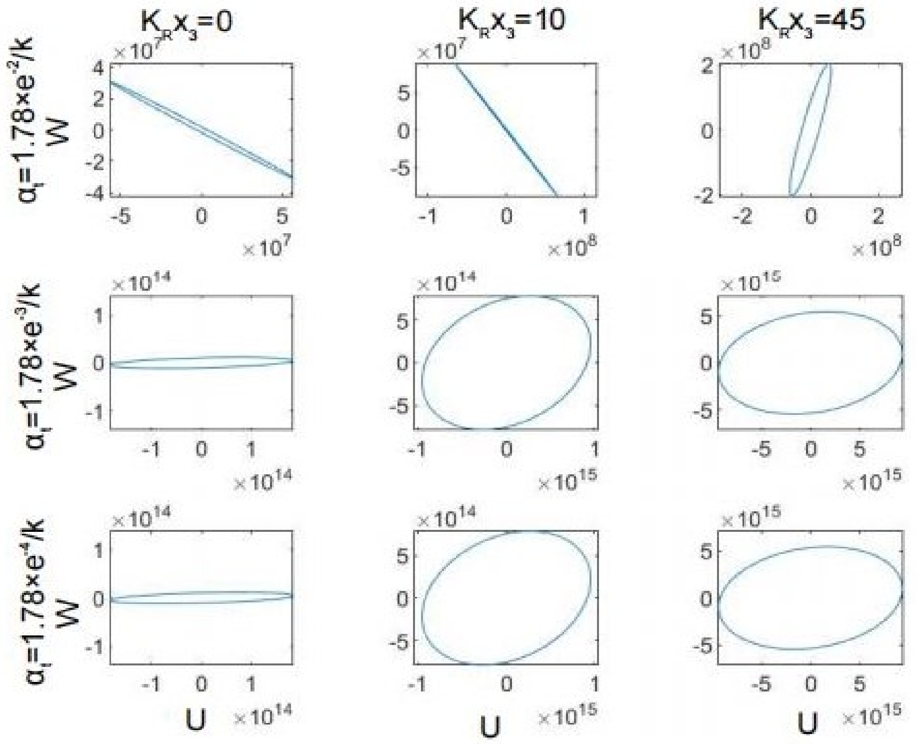

Figure 4. Variation of particle motion (U, W) with depth $K_R x_3 = 0,15,45$ for Couple theory of thermoelasticity and for L-S theory of thermoelasticity respectively.

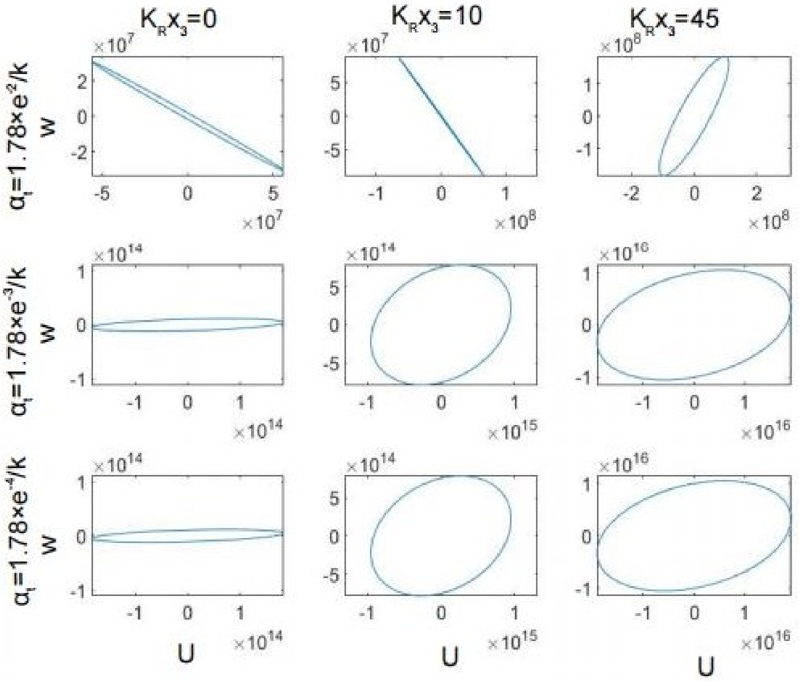

Figure 5. Variation of particle motion (U, W) with depth $K_R x_3 = 0,15,45$ for G-L theory of thermoelasticity and for G-N theory of thermoelasticity.

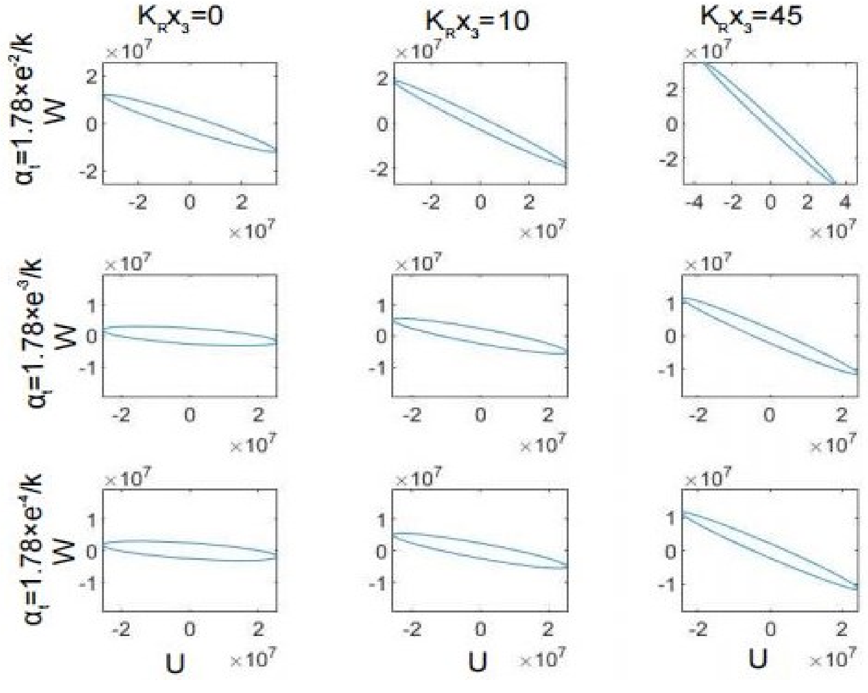

Figure 6. Variation of particle motion (U, W) with depth $K_R x_3 = 0,15,45$ for G-L theory of thermoelasticity and for G-N theory of thermoelasticity.

The effects of α_t on tilted particle motion at different depths are illustrated in **Figures 3–8**. It is noted that in the coupled, G-L, and two-phase-lag theories, the amplitude of the Rayleigh wave increases with an increase in values of α_t. The G-N theory shows a constant, and the remaining theories show a decrease in amplitude with an increase in thermal conductivity.

The elliptic path does not change with changes in depth or theories of thermoelasticity. In the case of G-N theory, the amplitude of the Rayleigh wave increases with an increase in the value of depth. The difference in plots of columns is observed as the motion of particle polarization and amplitude are very sensitive to any change in thermal conductivity. Fluctuations are observed in amplitude with depth, as is observed in other theories. Maximum tilt in the case of three-phase-lag theory increases with an increase in depth.

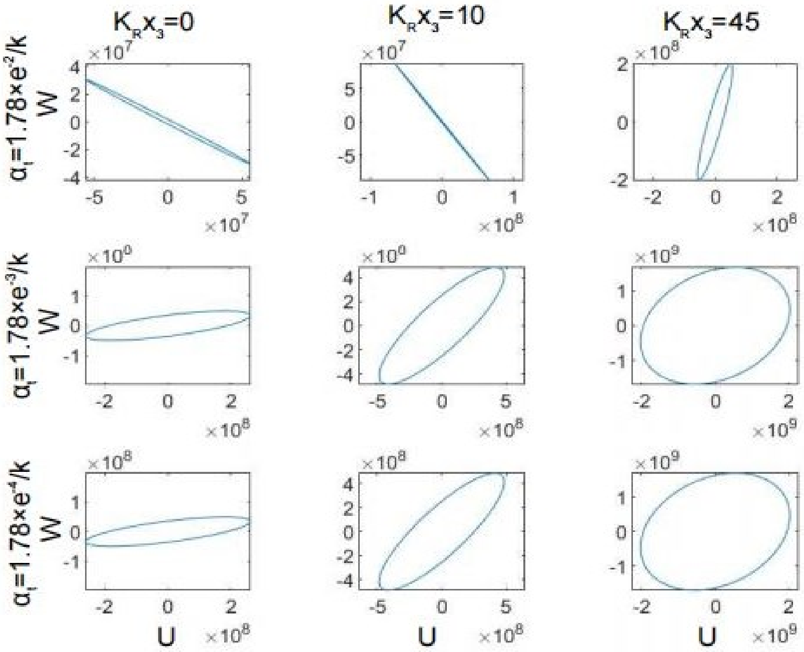

Figure 7. Variation of particle motion (U, W) with depth $K_R x_3 = 0,\ 15,\ 45$ for two phase lag and for three phase lag theory of thermoelasticity.

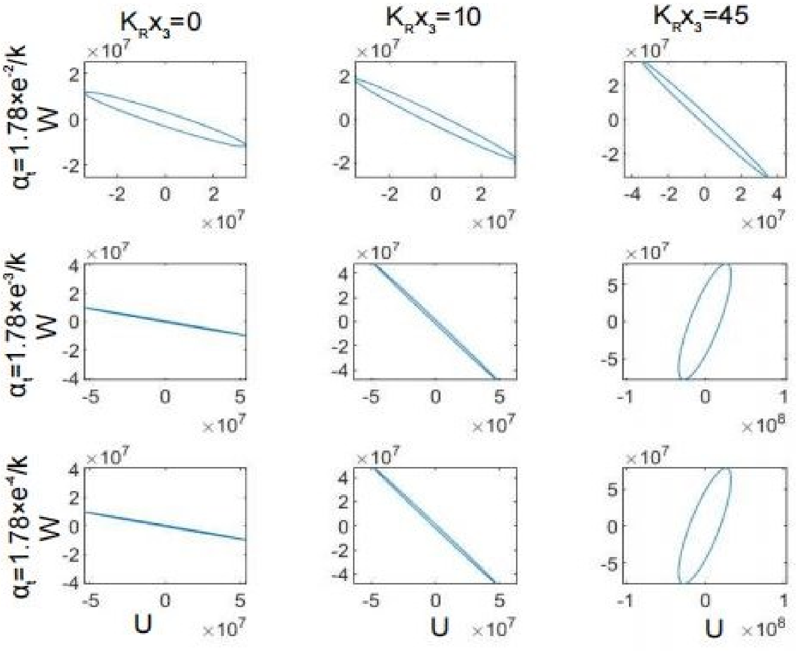

Figure 8. Variation of particle motion (U, W) with depth $K_R x_3 = 0{,}15{,}45$ for two phase lag and for three phase lag theory of thermoelasticity.

7. Conclusion

In this manuscript, the compact form of the heat conduction equation is used to study the coupled L-S, G-L, G-N, two-phase-lag, and three-phase-lag models of thermoelasticity in the propagation of the Rayleigh wave in an isotropic homogenous medium. For insulated surfaces, the dispersion equation is obtained with irrational terms. To obtain a polynomial equation, the dispersion equation is rationalized. Roots are filters that satisfy both equations by checking their decay properties with depth. The comparison of different theories is significant for studying the characteristic properties of the Rayleigh wave.

The phase velocity, attenuation coefficient, and path of particle motion are calculated numerically and presented graphically to compare different theories of thermoelasticity.

The thermally insulated surface reduces the speed of the Ryleigh wave; on the other hand, millions of folds' increases may be noticed in cases of attenuation of the wave.

It is observed that the phase velocity attains its maximum value in the case of coupled theory and its minimum value in the case of two-phase-lag theory. All theories show a smooth, decreasing curve with increasing frequency.

For coupled theory, an instant increase and then constant values of the attenuation coefficient are observed, whereas in the case of two-phase-lag theory, a decreasing slope line is observed with increasing frequency. In the other four theories, values are very close to zero due to this overlapping.

The effect of different theories is significant for the particle motion of the Rayleigh wave and shows an elliptic path for different depths and the coefficient of thermal linear expansion. The Rayleigh wave is one of the surface waves, which is very helpful for studying various aspects of an earthquake.

Author contributions: Conceptualization, MK, VG and SG; methodology, MK, VG and SG ; software, SG, PK and PB; validation, MK, VG and SG; formal analysis, MK, VG, SG, PK and PB; investigation, MK, VG and SG; data curation, MK, VG and SG; writing—original draft preparation, SG; writing—review and editing, MK, VG and SG; supervision, MK and VG. All authors have read and agreed to the published version of the manuscript.

Conflict of interest: The authors declare no conflict of interest.

References

1. Biot MA. Thermoelasticity and Irreversible Thermodynamics. Journal of Applied Physics. 1956; 27(3): 240–253. doi: 10.1063/1.1722351
2. Green AE, Lindsay KA. Thermoelasticity. Journal of Elasticity. 1972; 2(1): 1–7. doi: 10.1007/bf00045689
3. Lord H, Shulman Y. A generalised dynamical theory of thermoelasticity. J. Mech. Phys. Solids. 1967; 15: 299–309. doi: 10.1016/0022-5096(67)90024-5
4. Green AE, Naghdi PM. Thermoelasticity without energy dissipation. Journal of Elasticity. 1993; 31(3): 189–208. doi: 10.1007/bf00044969
5. Richard B, Hetnarski, JI. Generalized Thermoelasticity. Journal of Thermal Stresses. 1999; 22(4–5): 451–476. doi: 10.1080/014957399280832

6. Ignaczak J and Ostoja-Starzewski M. Thermoelasticity with Finite Wave Speeds. Oxford University Press; 2009.
7. Tzou DY. A Unified Field Approach for Heat Conduction from Macro- to Micro-Scales. Journal of Heat Transfer. 1995; 117(1): 8–16. doi: 10.1115/1.2822329
8. Choudhuri SKR. On A Thermoelastic Three-Phase-Lag Model. Journal of Thermal Stresses. 2007; 30(3): 231–238. doi: 10.1080/01495730601130919
9. Deresiewicz H. Effect of boundaries on waves in a thermo-elastic solid: Reflection of plane waves from plane boundary. J. Mech. Phys. Solids. 1960; 8: 164–172. doi: 10.1016/0022-5096(60)90035-1
10. SInha AN, Sinha SB. Reflection of thermoelastic waves at a solid half-space with thermal relaxation. Journal of Physics of the Earth. 1974; 22(2): 237–244. doi: 10.4294/jpe1952.22.237
11. Sinha SB, Elsibai KA. Reflection of Thermoelastic Waves at A Solid Half-Space with Two Relaxation Times. Journal of Thermal Stresses. 1996; 19(8): 749–762. doi: 10.1080/01495739608946205
12. Sharma JN, Kumar V, Chand D. Reflection of generalized thermoelastic waves from the boundary of a half-space. Journal of Thermal Stresses. 2003; 26(10): 925–942. doi: 10.1080/01495730306342
13. Singh MC, Chakraborty N. Reflection of a plane magneto-thermoelastic wave at the boundary of a solid half-space in presence of initial stress. Applied Mathematical Modelling. 2015; 39(5–6): 1409–1421. doi: 10.1016/j.apm.2014.09.013
14. Wei W, Zheng R, Liu G, et al. Reflection and Refraction of P Wave at the Interface Between Thermoelastic and Porous Thermoelastic Medium. Transport in Porous Media. 2016; 113(1): 1–27. doi: 10.1007/s11242-016-0659-1
15. Li Y, Li L, Wei P, et al. Reflection and refraction of thermoelastic waves at an interface of two couple-stress solids based on Lord-Shulman thermoelastic theory. Applied Mathematical Modelling. 2018; 55: 536–550. doi: 10.1016/j.apm.2017.10.040
16. Rayleigh L. On Waves Propagated along the Plane Surface of an Elastic Solid. Proceedings of the London Mathematical Society. 1885; 17(1): 4–11. doi: 10.1112/plms/s1-17.1.4
17. Lockett FJ. Effect of the thermal properties of a solid on the velocity of Rayleigh waves. J. Mech. Phys. Solids. 1958; 7: 71–75. doi: 10.1016/0022-5096(58)90040-1
18. Flavin JN. Thermo-elastic Rayleigh waves in a prestressed medium. Mathematical Proceedings of the Cambridge Philosophical Society. 1962; 58(3): 532–538. doi: 10.1017/s0305004100036811
19. Chadwick P, Windle DW. Propagation of Rayleigh waves along isothermal and insulated boundaries. Royal Society of London Series A Mathematical and Physical Sciences. 1964; 280(1380): 47–71. doi: 10.1098/rspa.1964.0130
20. Tomita S, Shindo Y. Rayleigh waves in magneto-thermoelastic solids with thermal relaxation. Int. J. Eng. Sci. 1979; 17: 227–232. doi: 10.1016/0020-7225(79)90067-3
21. Dawn NC, Chakraborty SK. On Rayleigh wave in Green-Lindsay's model of generalized thermoelastic media. Ind. J. Pure Appl. Math. 1988; 20: 273–286.
22. Abd-Alla AM, Ahmed SM. Rayleigh waves in an orthotropic thermoelastic medium under gravity field and initial stress. Earth, Moon, and Planets. 1996; 75(3): 185–197. doi: 10.1007/bf02592996
23. Ahmed SM. Rayleigh waves in a thermoelastic granular medium under initial stress. International Journal of Mathematics and Mathematical Sciences. 2000; 23(9): 627–637. doi: 10.1155/s0161171200002155
24. Sharma JN, Walia V, K Gupta S. Effect of rotation and thermal relaxation on Rayleigh waves in piezothermoelastic half space. International Journal of Mechanical Sciences. 2008; 50(3): 433–444. doi: 10.1016/j.ijmecsci.2007.10.001
25. Abouelregal AE. Rayleigh waves in a thermoelastic solid half space using dual-phase-lag model. International Journal of Engineering Science. 2011; 49(8): 781–791. doi: 10.1016/j.ijengsci.2011.03.007
26. Mahmoud SR. Influence of rotation and generalized magneto-thermoelastic on Rayleigh waves in a granular medium under effect of initial stress and gravity field. Meccanica. 2012; 47(7): 1561–1579. doi: 10.1007/s11012-011-9535-9
27. Chiriţă S. On the Rayleigh surface waves on an anisotropic homogeneous thermoelastic half space. Acta Mechanica. 2012; 224(3): 657–674. doi: 10.1007/s00707-012-0776-z
28. Bucur AV, Passarella F, Tibullo V. Rayleigh surface waves in the theory of thermoelastic materials with voids. Meccanica. 2013; 49(9): 2069–2078. doi: 10.1007/s11012-013-9850-4
29. Passarella F, Tibullo V, Viccione G. Rayleigh waves in isotropic strongly elliptic thermoelastic materials with microtemperatures. Meccanica. 2016; 52(13): 3033–3041. doi: 10.1007/s11012-016-0591-z
30. Biswas S, Mukhopadhyay B, Shaw S. Rayleigh surface wave propagation in orthotropic thermoelastic solids under three-phase-lag model. Journal of Thermal Stresses. 2017; 40(4): 403–419. doi: 10.1080/01495739.2017.1283971

31. Singh B, Verma S. On Propagation of Rayleigh Type Surface Wave in Five Different Theories of Thermoelasticity. International Journal of Applied Mechanics and Engineering. 2019; 24(3): 661–673. doi: 10.2478/ijame-2019-0041
32. Kumar A, Sangeeta SH. Rayleigh Wave Propagation with The Effect of Initial Stress, Magnetic Field and Two Temperature in The Dual Phase Lag Thermoelasticity. Advances in Mathematics: Scientific Journal. 2020; 9(9): 7535–7545. doi: 10.37418/amsj.9.9.100
33. Kumar R, Gupta V. Rayleigh waves in generalized thermoelastic medium with mass diffusion. Canadian Journal of Physics. 2015; 93(10): 1039–1049. doi: 10.1139/cjp-2014-0681
34. Sharma MD. Rayleigh wave at the surface of a general anisotropic poroelastic medium: derivation of real secular equation. Proceedings of the Royal Society A: Mathematical, Physical and Engineering Sciences. 2018; 474(2211): 20170589. doi: 10.1098/rspa.2017.0589
35. Sharma MD. Propagation of Rayleigh waves at the boundary of an orthotropic elastic solid: Influence of initial stress and gravity. Journal of Vibration and Control. 2020; 26(21–22): 2070–2080. doi: 10.1177/1077546320912069
36. Haque I, Biswas S. Rayleigh waves in nonlocal porous thermoelastic layer with Green-Lindsay model. Steel and Composite Structures. 2024; 50(2): 123-133.
37. Saeed T, Ali Khan M, Alzahrani ARR, et al. Rayleigh wave through half space semiconductor solid with temperature dependent properties. Physica Scripta. 2024; 99(2): 025208. doi: 10.1088/1402-4896/ad17fe
38. Kumar R, Gupta V. Uniqueness, reciprocity theorems and plane wave propagation in different theories of thermoelasticity. International Journal of Applied Mechanics and Engineering. 2013; 18(4): 1067–1086. doi: 10.2478/ijame-2013-0067
39. Sharma MD. Propagation and attenuation of Rayleigh waves in generalized thermoelastic media. Journal of Seismology. 2013; 18(1): 61–79. doi: 10.1007/s10950-013-9401-4
40. Ewing WM, Jardetzky WS, Press F, et al. Elastic Waves in Layered Media. Physics Today. 1957; 10(12): 27–28. doi: 10.1063/1.3060203

Thermal Science and Engineering 2024, 7(3), 8671.
https://doi.org/10.24294/tse.v7i3.8671

Article

Relating alkali release from a wood pellet with combustion progress: A modified random pore model supportive study

Rudolf P. W. J. Struis[1,2,*], Marco Wellinger[1,3], Christian Ludwig[1,2]

[1] PSI Center for Energy and Environmental Sciences, LEP CPM, Paul Scherrer Institute (PSI), 5232 Villigen PSI, Switzerland
[2] School of Architecture, Civil and Environmental Engineering, ENAC IIE GR-LUD Station 2, École Polytechnique Fédérale de Lausanne (EPFL), 1015 Lausanne, Switzerland
[3] Institute of Chemistry and Biological Chemistry, Coffee Excellence Center, Zurich University of Applied Sciences (ZHAW), 8820 Wädenswil, Switzerland
*** Corresponding author:** Rudolf P. W. J. Struis, rudolf.struis@psi.ch, rudolfstruis@ursulaburgherr.ch

CITATION

Struis RPWJ, Wellinger M, Ludwig C. Relating alkali release from a wood pellet with combustion progress: A modified random pore model supportive study. Thermal Science and Engineering. 2024; 7(3): 8671. https://doi.org/10.24294/tse.v7i3.8671

ARTICLE INFO

Received: 10 July 2024
Accepted: 16 August 2024
Available online: 23 August 2024

COPYRIGHT

Copyright © 2024 by author(s). *Thermal Science and Engineering* is published by EnPress Publisher, LLC. This work is licensed under the Creative Commons Attribution (CC BY) license. https://creativecommons.org/licenses/by/4.0/

Abstract: This paper concerns a miniature gasifier fed with a constant ambient-pressure flow of air to study the pyrolysis and subsequent combustion stage of a single wood pellet at T = 800 °C. The alkali release and the concentration of simple gases were recorded simultaneously using an improved alkali surface ionisation detector and a mass spectrometer in time steps of 1 s and 1.2 s, respectively. It showed alkali release during both stages. During combustion, the MS data showed almost complete oxidation of the charred pellet to CO_2. The derived alkali release, "O_2 consumed", and "CO_2 produced" conversion rates all indicated very similar temporal growth and coalescence features with respect to the varying char pore surface area underlying the original random pore model of Bhatia and Perlmutter. But, also large, rapid signal accelerations near the end and marked peak-tails with O_2 and CO_2 after that, but not with the alkali release data. The latter features appear indicative of alkali–deprived char attributable to the preceding pyrolysis with flowing air. Except for the peak-tails, all other features were reproduced well with the modified model equations of Struis et al. and the parameter values resembled closely those reported for fir charcoal gasified with CO_2 at T = 800 °C.

Keywords: wood pellet; pyrolysis; combustion; alkalis; surface ionisation detector; random pore model; alkali deprivation

1. Introduction

When using natural or waste wood in thermo-chemical conversion processes, a number of heteroatoms (e.g., sulfur, chlorine, mainly potassium, with or without metal contaminants) may hinder the processes, as well as, pose a threat to equipment and/or the environment. Due to the often strongly heterogeneous composition of the feedstocks and high dynamics of thermo-chemical reactions, the elemental concentrations in process gases show a high temporal variability. In order to accurately characterize such changes, efficient and representative sampling methods and analytical instruments with a high sensitivity and time resolution are necessary. To this purpose, a miniature thermo-chemical reactor (MTR) had been developed and constructed at PSI to study the pyrolysis and subsequent combustion of single commercial-sized wood pellets under a constant flow of ambient-pressure air at T = 800 °C. During the run, the amount of alkalis released with the reactor gas was monitored using an improved alkali surface ionisation detector (SID II) in time steps of about 1 s, and the evolution of simple gases by mass-to-charge ratios recorded with a MS every 1.2 s. After several numerically executed steps and conversions (see further on), the resulting alkali release, "O_2 consumed" and "CO_2 produced" rate course data with the combustion-specific stage were each compared in view of the modified random pore model of Struis et al. [1] and with the weight loss data of wood char from a pre-pyrolysed fir lath piece recorded during gasification with CO_2 at T = 800 °C in a TGA [1–3].

Thermo-chemical conversion processes with woody feedstock

During thermal conversion of woody feedstock, four stages can occur consecutively as a function of time with increasing temperature [4,5]:

(1) Heating and drying (up to T = 200 °C). (2) Pyrolysis (starting from T = 200 °C) by thermal decomposition of biomass macromolecules in the absence of an oxidant. (3) Gasifcation (starting from T = 400 °C) by partial oxidation by an understochiometric amount of oxidant. Or, (4) Combustion (starting here from T = 800 °C) by exhaustive oxidation with at least a stoichiometric amount of oxidant. Clearly, also overlap between stages (2–4) does occur. The four stages are depicted in **Figure 1**, including simple volatile components evolving from drying, pyrolysis, gasification, or combustion, towards the formation of wood ash at the end. The figure also shows another fresh wood pellet before combustion in air (λ = air-to-fuel ratio), after drying, after pyrolysis in N_2, and the wood ash at the end.

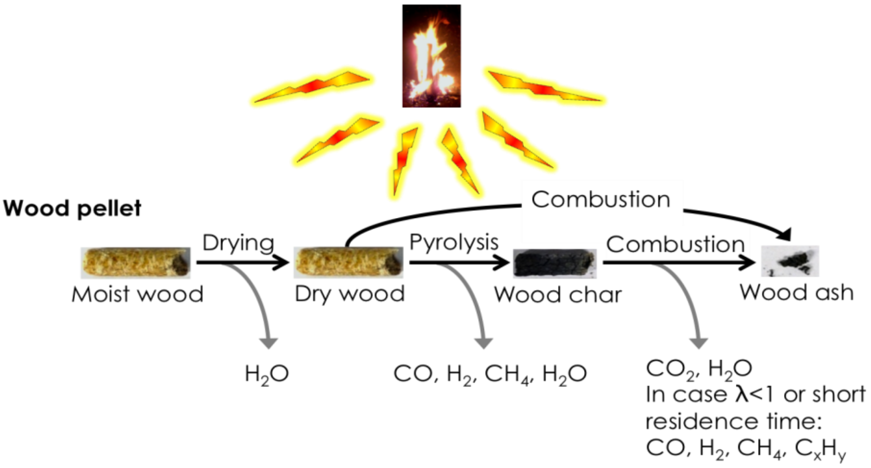

Figure 1. Stages of thermo-chemical conversion of a wood pellet.

2. Materials and methods

2.1. Chemical physical characteristics of the wood pellets

The wood pellets were bought from Buerli Trocknungsanlage (drying plant), Alberswil, Switzerland [6]. The pellets have a density of 1.2 kg/dm^3, a diameter of 6 mm, a length of around 2 cm, and water content below 10% by weight. A pellet weighing 0.70 ± 0.01 g was selected for the miniature gasifier run and with more pellets in other runs using a bubbling fluidized bed gasifier. The chemical composition of the wood pellet batch in question with respect to C, H, O, N, S, Cl, K, and Na is shown in **Table 1**. The pellet composition agrees well with that of most temperate-climate woods. It also shows that potassium is the predominant alkali element.

Table 1. Chemical composition of the wood pellets used in this work (C, H, O, N, S from Wellinger et al. [7], together with own results for K and Na with wood pellet ash.

Element concentration of the wood pellets	
C [Wt.-%]	47.31
H [Wt.-%]	6.23
O [Wt.-%]	44.44
N [Wt.-%]	0.18
S [Wt.-%]	0.01
Cl [Wt.-%]	< 0.02
K [µg/g]	551
Na [µg/g]	28

2.2. Overview of the experimental, sampling and measuring setup

The miniature thermo-chemical reactor (MTR, or simply "miniature gasifier"), alkali ionisation detector (SID II), continuous gas washer, and MS were setup according to the flow sheet shown in **Figure 2**. The gasification run was performed with a 750 ml_N/min flow of air under atmospheric pressure at room temperature. The air was supplied by an in-house filtering and compressor unit fed with ambient air. The air flow was led to the heated MTR. After stabilisation of gas flow and gasification temperature (T = 800 °C) with the MTR, one wood pellet was injected into the reactor through a vertical drop. Because a short length of sampling line is crucial when conducting direct gas measurements, the SID II was placed within 0.5 m distance from the gas outlet of the reactor. The remaining part of the reactor gas was directed to the continuous gas washer, operated at low temperature (T = −10 °C) and elevated pressure (P < 5 bar), to separate particulate and condensable matter. The non-volatile ("permanent") gases remaining after washing were then transported through sampling lines to the SID II and the MS, and they did neither affect the alkali nor the non-volatile gas transport efficiency.

2.3. Miniature thermo-chemical reactor

The design, construction, and experiments with a novel single pellet gasifier were the scope of the PhD thesis of Johannes and Judex at PSI [8]. The reactor was made from Inconel® to withstand the high temperatures during the run. The reaction chamber has a diameter of 16 mm and a height of 100 mm. The MTR is positioned inside a cylindrical furnace that can be heated electrically to the desired temperature to maximally T = 970 °C. The gasification agent (here ambient air) enters from the bottom through a distributor that at the same time serves as grate for the pellet. The reactor is placed in a vertical cylindrical cavity of a ceramic oven (Micromeritics, 48 V, 350 W). Reactor gas outlet and thermocouple inlet are positioned above the ceramic oven. The reactor temperature is measured by a thermocouple (Type K) with its tip positioned about 2 cm above the fuel grate within the reactor cavity. The wood pellet is given into a lock hopper above the reactor. When the temperature and all sensors are stable, the pellet is released through a ball valve and reaches the reactor grid in less than 30 s to avoid heating the pellet prematurely.

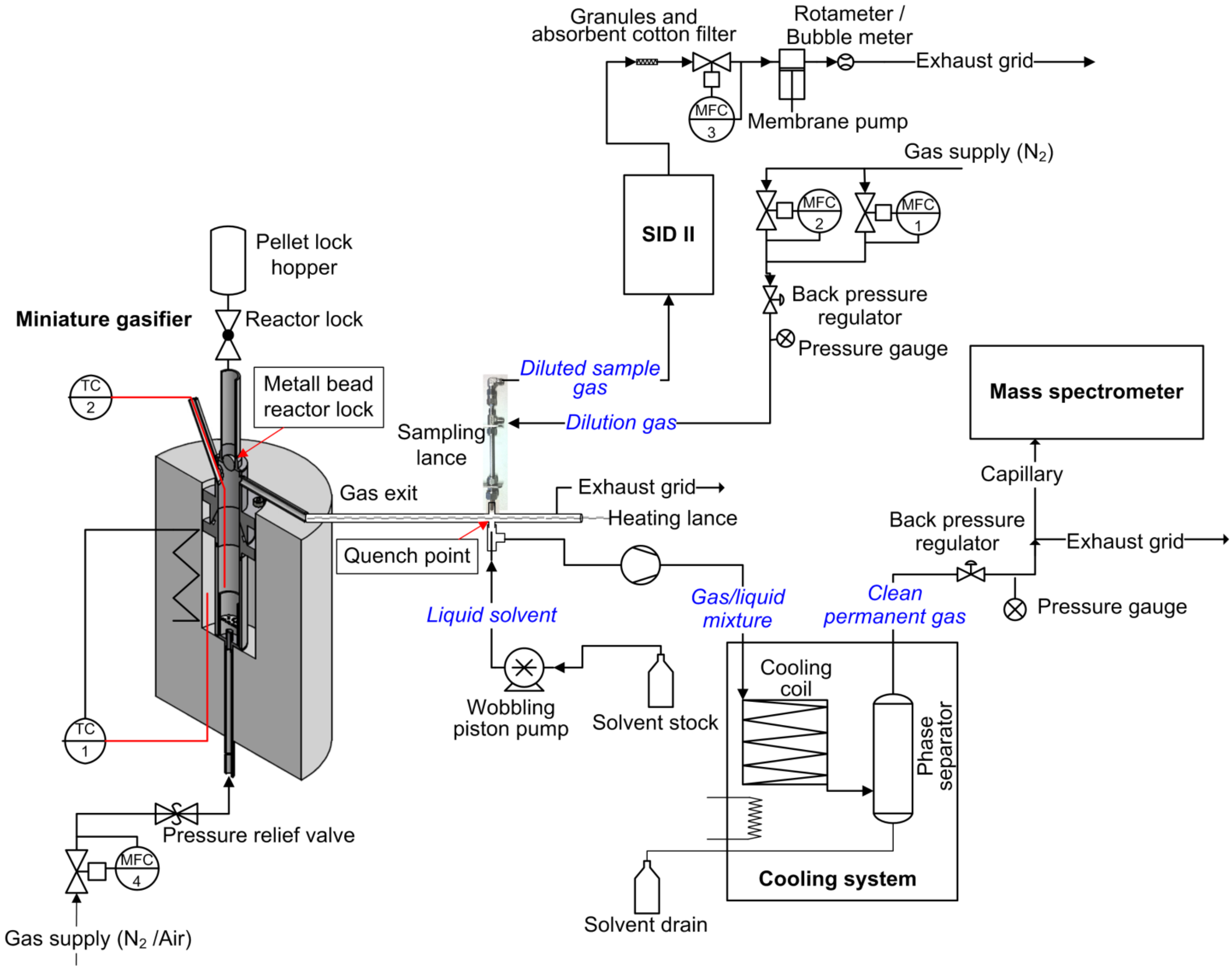

Figure 2. Flow sheet of the miniature gasifier including the sampling and measurement setup.

After that, a ferromagnetic ball is released to reduce any additional dead volume for the outgoing reactor gases. Lastly, the ball valve is closed again to provide additional sealing along with the cover nut. The pellet thus experiences similar conditions as if it had entered a large gasifier. The product gas leaves the reactor at the top through a sampling line heated to approximately T = 300 °C to prevent the condensation of tars. After each experiment, the grate was removed, the ash recovered, and the reactor cleaned. More details can be found in the literature [8,9].

2.4. Improved surface ionization detection (SID II)

The SID II is a newly developed alkali detector based on the principle of surface ionisation occurring by their impingement on a hot platinum filament, followed by acceleration of the ions by the voltage difference between filament and collector, and the detection of the ion current at the collector grating. Further details can be found in Judex [8] and Wellinger's works [9]. The detector signals are typically in the order of nano-amperes (nA). The alkali detector had demonstrated high sensitivity over 4 orders of magnitude [8,9]. The signal value depends on the effective volume flow carrying the alkalis and somewhat also on the bulk gas composition. Power law correlations were established to represent the measured signals accurately. Two correlations applicable for sodium and potassium nitrates nebulised at concentrations of 0.7, 7, and 70 $\mu g/m_N^3$ in air and in nitrogen, respectively, had already been published [9]. In order to exploit the alkali concentration validity range of the power law correlations, the gas from the reactor was diluted with a constant volume flow of N_2 prior to entering the SID II. The sample gas dilution setup and the sampling lance developed for SID II have been described elsewhere [7,9].

The principle of the sensor is based on the high probability of some alkali metals getting ionised during the desorption process from the ionising filament [10]. The sensor is especially sensitive to potassium (K), sodium (Na), and caesium (Cs) [11]. With our wood pellet, the concentration of K surmounts that of Na by a factor of 20 (**Table 1**), and the amount of Cs is normally negligibly small (<1 ppm [12]).

2.5. Continuous gas washer

After the SID II, a continuous gas washer (**Figure 2**) similar to the one described by Kowalski et al. [13] was used to separate water, soot, and tars from the permanent gases before being led to the MS. With the continuous gas washer, the raw gas was mixed thoroughly with water-containing organic solvent and transported to a two-phase separator unit operating at a below-zero temperature ($T = -10$ °C) under the pressure ($P < 5$ bar). The cleaned gas consists of "permanent" species that did not condensate out, and it led to the MS. In this study, 1-methoxy-2-propanol ($C_4H_{10}O_2$, CAS-Nr.107-98-2) was used as solvent, because of its much higher capability to solubilise tars in comparison to pure water. This is particularly important when analysing producer gas from pilot or industrial biomass gasifiers with high tar loads.

2.6. Mass spectrometer

The MS was a "Pfeiffer Thermostar" with a sample flow of approx. 1–2 ml_N/min depending on the pressure conditions at the capillary inlet. The built-in secondary electron multiplier was used as the detection system. For the present study, the mass signals for H_2^+($m/z = 2$), N_2^+ and CO^+($m/z = 28$), O_2^+($m/z = 32$), Ar^+($m/z = 40$), and CO_2^+($m/z = 44$) were selected to reconstruct the true reactor gas composition and amounts as a function of the experimental runtime. Under constant ambient pressure at the capillary inlet, the MS takes in a constant amount of sample gas from the reactor. When consumption or production occurs during the thermo-chemical conversion experiment, the gas flow alters. To convert the relative intensities measured by the MS into intensities that are proportional to the absolute flow from the reactor, argon ($m/z = 40$) in the air fed to the MTR with air was used as an internal, non-reactive, gaseous standard agent ("tracer") to compensate for total flow changes, as follows: The Ar signal intensity before the start of the experiment was used as a reference signal intensity. The recorded Ar signal intensity for each point in time was then divided by the reference signal intensity. This yielded ratio values ranging between 1.02 (ideally 1.00) before inserting the pellet into the reactor to 0.88 minimally during pyrolysis of the wood pellet. The Ar ratio values were then used to correct the other measured MS [m/z] intensities by dividing the MS-data by the Ar ratio data on a comparable runtime basis. As last step, the dilution-corrected MS data were converted into relative volume amounts (%V/V) after having experimentally established the proportionality ratio between simultaneously recorded MS (in arbitrary units) and pre-calibrated Varian micro-GC (%V) values with each gas species of interest during gasification runs with wood pellets with air in a bubbling fluidized bed reactor at T = 755 °C [9].

2.7. Modified Random Pore Model (MRPM)

Struis et al. [1] derived kinetic relations by modification of the original random pore model (RPM) of Bhatia and Perlmutter [14]. The original RPM addressed the conversion degree, X, the conversion-time behaviour, $X(t)$, and the conversion progress rate, dX/dt, of a solid-gas reaction with a carbonaceous porous solid in terms of the variation in the reaction surface area, S. The original model uses two parameters (A_0, ψ) to describe or reproduce the behaviour of a system that either shows one or no maximum in the derived conversion progress rate with runtime. A_o denotes the experimentally accessible reaction rate at start, and ψ comprises details regarding the pore system. The maximum in dX/dt (=S/S_0) with conversion degree is attributed to two opposing effects: pore growth increases the reaction surface area, and pore coalescence at intersections decreases the reaction surface area. In the work of Struis et al. [1, 2], and that of other workers [15,16], the conversion progress, X, is connected with the weight of the porous char sample, M, according to:

$$X(t) = (M_0 - M(t))/(M_0 - M_{ash}) \tag{1}$$

here, M_0 denotes the char weight at the start of the gasification, M_{ash} stands for the weight of the bottom ash after complete conversion, and $M(t)$ is the weight at a run time t. Accordingly, $X(t)$ is zero at start and attains unity at completion of the mass conversion. The conversion progress rate, dX/dt, can principally also be interrelated with other quantities associated with the char-gas reaction, such as the amount of oxidant gas consumed (here, O_2), the amount of product gas produced (here, mainly CO_2), and the release of biomass-native alkali from the sample (here, one wood pellet). Under kinetic control and ignoring the reaction on the exterior woody particle surface, the kinetic equations modified by Struis et al. [1] are defined by correlation time, τ', and conversion rate progress, X, as given in Equation (2) and Equation (3), respectively:

$$\tau' = A_0 t[1 + (Bt)^P] \tag{2}$$

$$X = 1 - e^{-\tau'\left(1+\frac{\psi\tau'}{4}\right)} \tag{3}$$

In Equation (2), τ' is a dimensionless run time, t the experimental run time, A_0 the experimentally accessible initial reaction rate, Ψ the pore system related structural constant, B a reciprocal time constant, and P a dimensionless power law constant. After differentiating Equation (3) with respect to time t, the resulting rate reads [1]:

$$\frac{\mathrm{d}X}{\mathrm{d}t} = \mathrm{A}_0(1 + (P + 1)(Bt)^P)(1 - X)\sqrt{1 - \psi \ln(1 - X)} \tag{4}$$

Noteworthy, the three modified equations converge to the original ones from Bhatia and Perlmutter when fixing $B = 0$.

2.8. Data treatment of selected MS gas data for model analysis

Figure 3 shows a compilation of the raw alkali signal from SID II in nano-Ampere, [nA], the temperature [°C] inside the reactor, and the MS signals for selected gases, as a function of the experimental runtime, with the single wood pellet at T = 800 °C. **Figure 3** shows H_2 (m/z = 2), O_2 (m/z = 32), CO and N_2 (both m/z = 28), and CO_2 (m/z = 44) in the MS machine units after having been corrected for gas dilution effects.

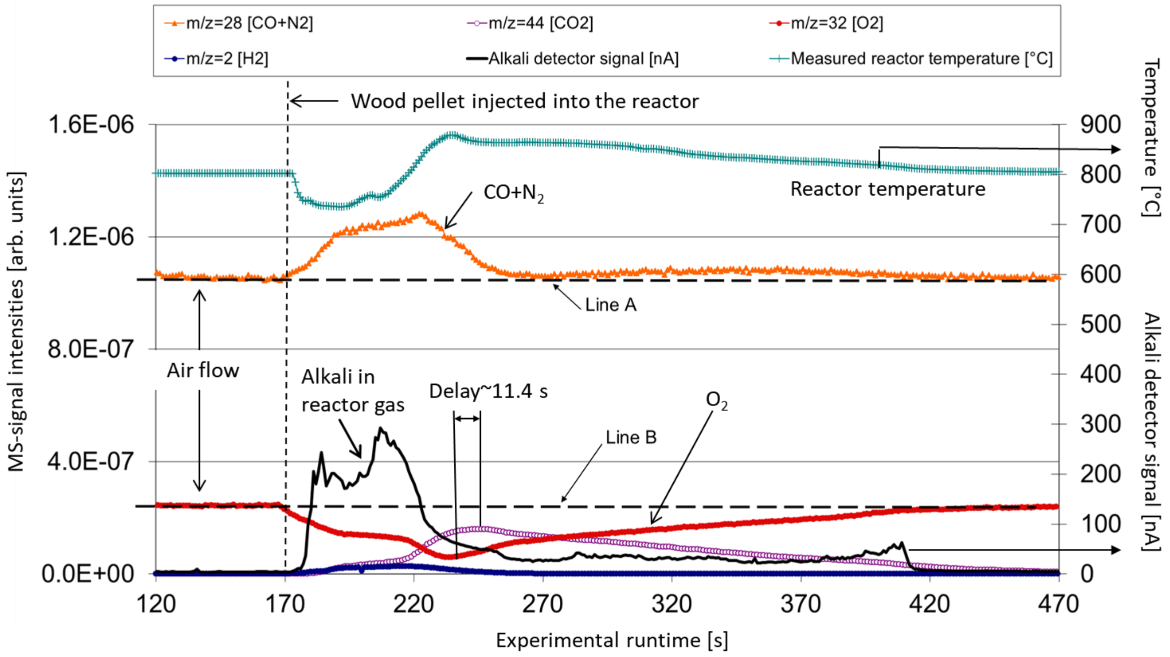

Figure 3. Raw data compilation of the amount of alkalis detected with the reactor gas, the reactor temperature, MS signals for m/z = 28 (CO + N_2), m/z = 32 (O_2), and other gases, recorded during the thermo-chemical conversion run of a single wood pellet at T = 800 °C in a constant flow of air.

After pellet injection, the CO_2 and O_2 courses with runtime progress in a complementary manner in that the O_2 signal passes through a minimum at $t \approx 233$ s, whereas CO_2 shows a maximum, but later at $t \approx 244$ s. The delay is likely caused by the moderate affinity of CO_2 with the liquid quench solvent (1-methoxy-2-propanol), as also noticed in other studies with the continuous gas washer [17,18]. The anomaly in runtime was not detected with the other gases. Hence, the "dwell time" of CO_2 was corrected by subtracting 10.5 s from the experimental runtimes.

The amounts of "CO produced" and "O_2 consumed" were obtained by subtracting the constant N_2 and O_2 levels pertaining to clean air for and after the experimental run (**Figure 2**) and then multiplying the resulting O_2 values with −1. The released alkali amounts and the amounts of "O_2 consumed", H_2, CO, CH_4, and "CO_2 produced" were each converted to calibrated units (Section 2.6). The values of "d*X* (O_2 consumed)/d*t*" and "d*X* (CO_2 produced)/d*t*" with the combustion stage were first averaged as follows: To suppress the impact from experimental noise with the calibrated MS data, two data blocks with one data point in between were used. Each data block comprised nine successive $\{t, X(t)\}$ data points. Instead of using two adjacent data points, block-averaged values were used to calculate dX/dt, and the result was allocated with the time value of the data point between the blocks. The procedure was repeated by moving the blocks plus intermediate data point one position forward in time, and so on, till reaching the end of the experimental data set in question.

Lastly, with gasification runs with more pellets in a fluidized bubble-bed gasifier under ideal gas solvent quench conditions, it was reported that the gas-phase "downstream/upstream" ratio with CO_2 could only be kept between 0.9–1, whereas those of H_2, CO, and CH_4 were much better (ratios~1) [17,18]. This was also evidenced in this study by comparing the calibrated "O_2 consumed" and "CO_2 produced" data where they reflected complete combustion, i.e., $C_{char} + O_2 \rightarrow CO_2$ and CO absent. Although the differences were small, the data overlay (not shown here) was not consistent enough ([O_2 consumed] ≠ [CO_2 produced]), but the differences diminished at higher runtimes. The anomaly was overcome by multiplying the "CO_2 consumed" values with 1.035.

2.9. Experimental point of reference with the MRPM analysis

The point of reference for comparing the temporal alkali and gas rate courses and model parameters obtained in this study were the model parameters for the mass loss conversion rate (Equation (1)) with pre-pyrolysed and grinded charcoal particles prepared from one fir lath (without bark). About 10 mg charcoal was gasified with CO_2 at T = 800 °C in a TGA. In contrast with the wood pellet, the fir charcoal was obtained in two consecutive stages: Pre-pyrolysis (2.5 h at T = 600 °C under Ar flow) and post-pyrolysis (20 min at T = 900 °C under He flow) [1,2]. Notwithstanding these, a comparison is fair in that the certified wood pellet batch comprises a high amount of heartwood among less sapwood, bark, branches or twigs. In the literature, the modified RPM equations were found applicable with several tree woods, chars, and charcoals. The reference sample is hereafter named "fir charcoal".

3. Results and discussion

3.1. Chemical and physical transients during the wood pellet gasification

For better visibility, the two apparent stages with the gasification run are shown separately in **Figure 4A**,**B**, respectively. It must also be mentioned that the alkali release is now shown in the calibrated unit of [mg/m_N^3], and "O_2 consumed", H_2, CH_4, CO_2, and "O_2 consumed" in the calibrated [%V/V] unit.

With the pyrolysis stage (**Figure 4A**), the tentatively drawn broken line with the temperature progresses rather smoothly with runtime. In chronological order, it depicts the arrival of the wood pellet in the reactor cavity by a fast temperature drop; the temperature passes through a minimum, and recovers again by the heat produced from the combustion of outflowing flammable gases and possibly also less combustion resistant wood pellet constituents. After that, the temperature even surpasses the pre-settled reactor temperature (T = 800 °C), passes through a maximum, and then converges slowly to a temperature of T ≈ 860 °C around runtime ~280 s. The tentative temperature course also emphasizes transient's features, such as water evaporation with the pellet (A), wood depolymerisation (D), and presumably also combustion of lignin (C) mobilized with the manufacturing of the wood pellets to "glue" the wood particles during the pelletization process together.

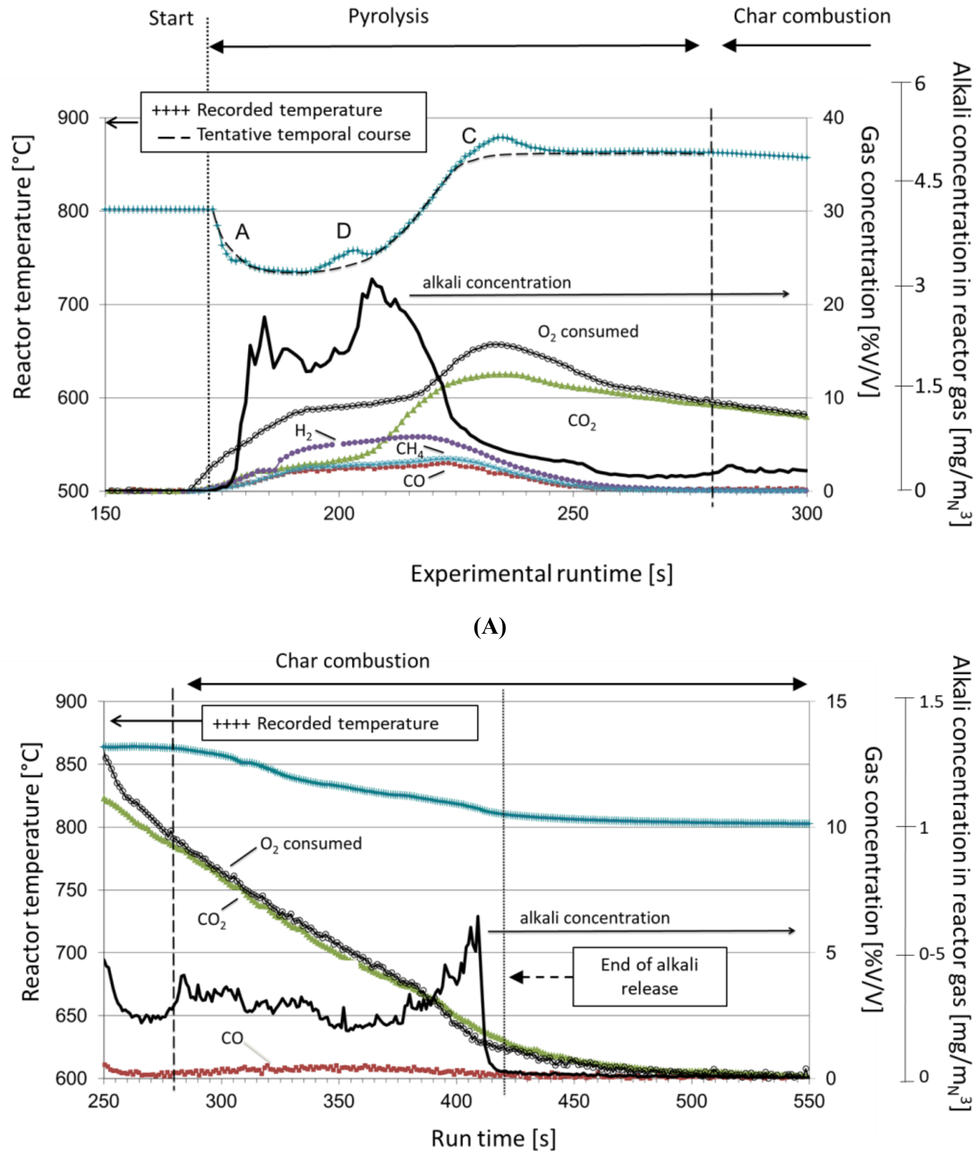

(A)

(B)

Figure 4. (A) Measured and tentative reactor temperature course as a function of the experimental run time. Also shown are the amount of alkalis detected in the reactor gas [mg/m_N^3], the amount of "O_2 consumed", and several other evolving gases (H_2, CO, CO_2, CH_4) in [%V/V]; **(B)** Continuation of the data shown with **Figure 4A** with extended, enlarged axis scales.

Particulates from sawmills and planning works [7]. The temperature stabilization around runtime ~280 s coincided with the absence of CO, H_2, and CH_4

with the reactor gas, whereas the signals of "CO_2 produced" and "O_2 consumed" continued.

In **Figure 4B**, the reactor temperature in the alleged sole char combustion stage converged gradually from T ≈ 860 °C (runtime ~280 s) to a stable temperature laying slightly above T = 800 °C for runtimes > 500 s. With [CO] much smaller than [CO_2, it reflects near complete combustion of the charred wood pellet with O_2.

Lastly, a large alkali release started jointly with the outflow of flammable gases from the wood pellet during the pyrolysis stage (**Figure 4A**). The alkali release continued during the combustion stage (**Figure 4B**), but in much smaller amounts. (Note that the alkali unit scale range with **Figure 4A** is 4 times larger than with **Figure 4B**).

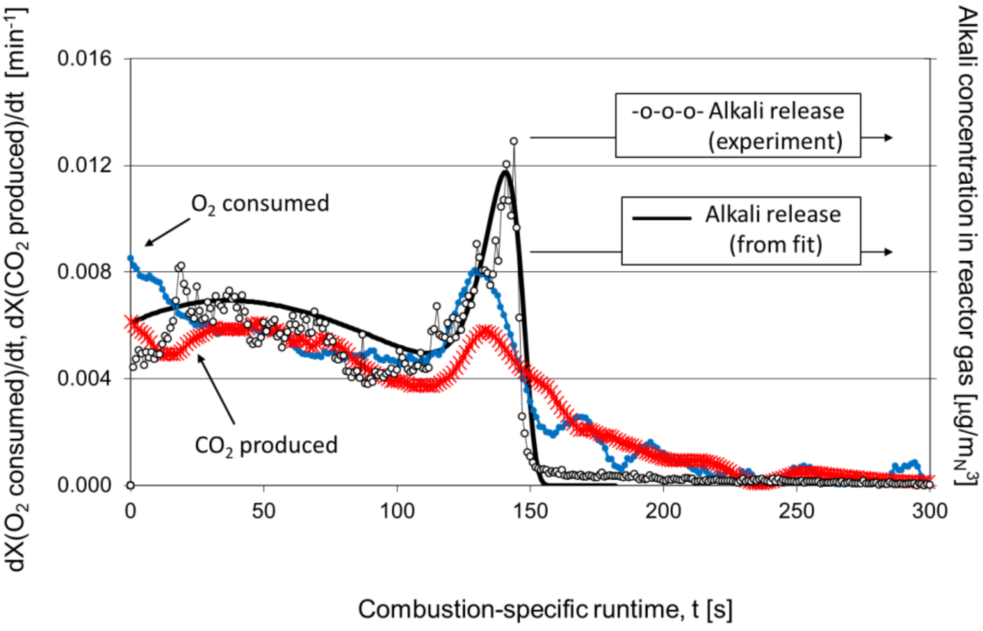

Figure 5. Overlay of measured (-o-) and fitted alkali release data (solid line using Equtions (2–4)) together with "O_2 consumption" and "CO_2 production" rates derived from MS data recorded simultaneously during the combustion stage of the wood pellet under a constant air flow at T = 800 °C.

3.2. Relating the alkali release to product gas reaction rates

Figure 5 shows the alkali concentration with the reactor gas, as a function of the combustion-specific runtime ($t_{combustion}$ = 0). The start time was chosen where, with **Figures 4A,B**, the O_2 and CO_2 concentrations predominated in the near absence of any other pyrolysis or combustion product gases. Here, the start of the pellet combustion stage was arbitrarily fixed at the experimental runtime = 280 s. Modelling the alkali release data, an additional parameter was added to multiply the integral right-hand side of Equation (4) to prevent compromising the original meaning of parameter A_0 as the reaction rate with the initial char(coal) pore surface area [1,14].

With **Figure 5**, the drawn solid black line shows the reproduced temporal course of the alkali release by the MRPM for the parameters shown in **Table 2**. With

Table 2, the unit for A_0 and B with the wood pellet is [s^{-1}], and with the fir charcoal [min^{-1}] because O_2 is more reactive than CO_2. The data reproduction quality with the alkali release data was satisfactory, except for the minute peak-tail at the end that lasted till about $t_{combustion}$ ~300 s.

Table 2. Model parameters derived for Equation (4) with the temporal alkali release of a charred wood pellet during combustion in flowing air at T = 800 °C, and from the weight loss of pre-pyrolysed fir charcoal during gasification with CO_2 at T = 800 °C [1]. Standard (1σ) errors were provided by the modelling software.

Sample	**Parameter's quantity**	**Numerical data multiplication factor**	A_0	ψ	B	P
Charred wood	Alkali release	44607	0.00609	4.5	0.00669	18.6
Pellet (this study)	(Single run)	± 378	±0.00017 [s^{-1}]	±0.4 [-]	± 0.00002 [s^{-1}]	±0.6 [-]
Fir charcoal [1]	Weight loss	Not applicable	0.0056	5.0	0.0051	14.4
	(18 experiments)		±0.0013 [min^{-1}]	±0.2 [-]	± 0.0003 [min^{-1}]	±1.6 [-]

Also shown with **Figure 5** are the "O_2 produced" and the "CO_2 consumed" dx/dt rate data (in their own calibrated units). The gas axis values were chosen such to achieve a high visually possible overlay (coverage) with the alkali release data. All three data sets revealed typically the same features (**Figure 5**), except for deviations with $t_{combustion}$ < 23 s attributable to overlap with the preceding pyrolysis domain, and by a very small peak-tailing signal remaining after the decline of the taller, but shorter-lived, alkali release peak. The peak-tail began after $t_{combustion}$ ~140 s and lasted for at least 100 s after that. Actually, similarly small signal-tais and time durations were also found with the raw MS data with the gases, except for CO and CO_2 in that they showed substantially larger tail amplitudes. Striking also is that both the CO and CO_2 d*X*/dt signal-tails appeared as soon as the accelerated alkali release had ceased at $t_{combustion}$ ~140 s (**Figure 5**).

The different peak-tail amplitudes with the alkali release and the CO and CO_2 conversion rates during the combustion stage may be understood by the difference in reactivity of the flowing gas during the pyrolysis treatment in this study (reactive O_2) and with fir charcoal (inert Ar and He). The fir lath was destined for construction purposes, so it essentially consists of heartwood. In contrast with oxygen, pyrolysis in flowing, non-reactive gas at sufficiently high temperatures mainly enables the outflow of decomposition gases from woody samples, but hardly any combustion. Therefore, the alkalis with the fir heartwood are hardly depleted with the charcoal, where this could very well be the case with the wood pellet pyrolysis under O_2. This would also explain the fact that the alkali release with the charred wood pellet seems to have run out prematurely (**Figure 5**), and, as a result, the large signal-tail-amplitude with O_2 and CO_2 started where the alkali release had stopped. Noteworthy, the almost doubling of the effective combustion duration with the pellet char here was reported found with the fir charcoal that had been deprived of its alkali by washing them out with HCl [1].

Author contributions: Conceptualization, MW and CL; methodology, MW; software (curve fitting), RPWJS; validation, RPWJS and MW; formal analysis, RPWJS and MW; investigation, RPWJS and MW; resources, CL; data curation, RPWJS and MW; writing—original draft preparation, MW; writing—review and editing, RPWJS, MW and CL; visualization, MW; supervision, CL; project administration, CL; funding acquisition, CL. All authors have read and agreed to the published version of the manuscript.

Acknowledgments: In the very early stages of this project, financial support was obtained from Swisselectric research (Project TREPGAS) and the Swiss Federal Office of Energy (Project 102093). The authors also thank Johannes W. Judex for instructions regarding the miniature thermo-chemical reactor (MTR) and assisting the quantification of the MS data for main reactor gas components by simultaneous use of a calibrated micro-GC and a MS during bubbling fluidised bed test rig experiments with wood pellets. We are also grateful to Serge Biollaz (PSI) and his research group for valuable discussions and providing equipment, such as the continuous gas washer unit, and more.

Conflict of interest: The authors declare no conflict of interest.

Abbreviations

MS	Mass spectrometer
MTR	Miniature thermochemical reactor (“Miniature gasifyer”)
RPM	Random pore model
MRPM	Modified random pore model by Struis et al. [1]
SID II	Improved surface ionisation detector developed at PSI
TGA	Thermogravimetric analyser

Notation

A_0	Experimental initial reaction rate defined in Equation (2), min^{-1}
B	Modified model parameter introduced in Equation (2), min^{-1}
M_{ash}	Mass of ash, g
$M(t)$	Char coal mass at gasification time t, g
P	Power law constant with Equation (2), dimensionless
S	Active surface area per unit volume, m^2/m^3
t	Experimental run time, min
T	Temperature, °C
X	Conversion progress degree or burn-off, dimensionless

Greek letters

τ'	Correlation time defined with Equation (2), dimensionless
Ψ	Pore system parameter defined with Equation (3), dimensionless

Subscript

0	Initial, at start of the pellet gasification run

References

1. Struis RPWJ, von Scala C, Stucki S, Prins R. Gasification reactivity of char coal with CO_2. Part I: Conversion and structural phenomena. Chemical Engineering Science. 2002; 57(17): 3581-3592. doi: 10.1016/S0009-2509(02)00254-3
2. Struis RPWJ, von Scala C, Stucki S, Prins R. Gasification reactivity of char coal with CO_2. Part II: Metal catalysis as a function of conversion. Chemical Engineering Science. 2002; 57(17): 3593-3602. doi: 10.1016/S0009-2509(02)00255-5
3. Struis RPWJ, von Scala C, Stucki S, Prins R. In: Bridgwater AV (editor). Progress in Thermochemical Biomass Conversion. Blackwell Science Ltd.; 2001. Volume 1, pp. 73-91.
4. Higman C, van der Burgt M. Gasification Processes. Gasification. Published online 2008: 91-191. doi: 10.1016/b978-0-7506-8528-3.00005-5
5. Kaltschmitt M, Thrän D, Smith KR. Renewable Energy from Biomass. Encyclopedia of Physical Science and Technology. Published online 2003: 203-228. doi: 10.1016/b0-12-227410-5/00059-4
6. Ecological product from native forests—Pellet production. Available online: http://www.buerli-pellets.ch/herstellung (accessed on 20 August 2024).
7. Wellinger M. Development and Application of Devices for Online Trace Element Analysis of Thermal Process Gases from Woody Feedstocks [PhD thesis]. École polytechnique fédérale de Lausanne EPFL; 2012.
8. Judex, Johannes W. Grass for power generation: extending the fuel flexibility for IGCC power plants. Published online 2010. doi: 10.3929/ETHZ-A-006032252
9. Wellinger M, Biollaz S, Wochele J, et al. Sampling and Online Analysis of Alkalis in Thermal Process Gases with a Novel Surface Ionization Detector. Energy & Fuels. 2011; 25(9): 4163-4171. doi: 10.1021/ef200811q
10. Jäglid U, Olsson JG, Pettersson JBC. Detection of sodium and potassium salt particles using surface ionization at atmospheric pressure. Journal of Aerosol Science. 1996; 27(6): 967977. doi: 10.1016/0021-8502(96)00025-0
11. Svane M, Hagström M, Davidsson KO, et al. Cesium as a Tracer for Alkali Processes in a Circulating Fluidized Bed Reactor. Energy & Fuels. 2006; 20(3): 979-985. doi: 10.1021/ef050273l
12. Thy P, Lesher CE, Jenkins BM, et al. Trace Metal Mobilization During Combustion of Biomass Fuels. UC Berkeley; 2007.
13. Kowalski T, Judex J, Schildhauer TJ, et al. Transmission of Alkali Aerosols through Sampling Systems. Chemical Engineering & Technology. 2010; 34(1): 42-48. doi: 10.1002/ceat.201000366
14. Bhatia SK, Perlmutter DD. A random pore model for fluid-solid reactions: I. Isothermal, kinetic control. AIChE Journal. 1980; 26(3): 379-386. doi: 10.1002/aic.690260308
15. Figueiredo JL, Moulijn JA. Carbon and Coal Gasification. Springer Netherlands; 1986. doi: 10.1007/978-94-009-4382-7
16. van Heek KH, Mühlen HJ. Fundamental Issues in Control of Carbon Gasification Reactivity. In: Lahaye L, Ehrburger P (editors). Fundamental Issues in Control of Carbon Gasification Reactivity. Kluwer Academic Publishers; 1991. pp. 1-34.
17. Kaufman Rechulski MD, Schneebeli J, Geiger S, et al. Liquid-Quench Sampling System for the Analysis of Gas Streams from Biomass Gasification Processes. Part 1: Sampling Noncondensable Compounds. Energy & Fuels. 2012; 26(12): 7308-7315. doi: 10.1021/ef3008147
18. Kaufman Rechulski MD, Schneebeli J, Geiger S, et al. Liquid-Quench Sampling System for the Analysis of Gas Streams from Biomass Gasification Processes. Part 2: Sampling Condensable Compounds. Energy & Fuels. 2012; 26(10): 6358-6365. doi: 10.1021/ef300274p

EnPress Publisher, LLC

Add: 9650 Telstar Avenue, Unit A, Suite 121, El Monte, CA 91731, USA.
Email: contact@enpress-publisher.com
Web: https://systems.enpress-publisher.com

ISSN 2578-1782